FLUIDS IN NANOSCOPIC SPACE REVEALED BY NUCLEAR MAGNETIC RESONANCE (NMR)

Yan Song

A dissertation submitted to the faculty of the University of North Carolina at Chapel Hill in partial fulfillment of the requirements for the degree of Doctor of Philosophy in the Department of Applied Physical Sciences.

Chapel Hill
2019

Approved by:
Yue Wu
Alfred Kleinhammes
Sean Washburn
Theo Dingemans
Luchang Qin

ABSTRACT

Yan Song: Fluids in Nanoscopic Space Revealed by Nuclear Magnetic Resonance (NMR)
(Under the direction of Yue Wu)

The behavior of fluids in nanoscopic space is of enormous importance in various fields from biology to geophysics. At such length scales, fluids have a high surface-to-volume ratio and are subject to geometrical restrictions, leading to new phenomena that are not observed at bigger length scales. Fundamental understanding of the new sciences requires detailed characterizations of the structure, dynamics, and phase diagrams of confined fluids. Nuclear magnetic resonance (NMR) has been proven to be a versatile tool for this purpose. In this dissertation, NMR methods are developed for the study of the fluids in nanoscopic spaces.

A combined methodology of NMR-detected isotherm and NMR imaging capability are implemented to study microscopic processes of water sorption on activated carbons. The NMR imaging capability with sub-nanometer scale spatial resolution is based on the natural field gradient inside the pore space of conjugated systems owing to the diamagnetic response of ring currents. Specifically, two distinct growth mechanisms are identified: gradual growth of water clusters and cooperative growth by pore-bridging. While the desorption process is predominantly associated with a single water cluster shrinking in size. The relationship between the macroscopic sorption isotherm and microscopic molecular configurations is elucidated as well.

In situ NMR methods are then developed to study water effects on chemical warfare agent simulants (CWAS) capture in MOFs. Firstly, the CWAS adsorption capacity in MOFs is

decreased by the presence of water. More importantly, we find that the preadsorbed water significantly decelerates the transport of CWAS, which could be a rate-limiting step in decontamination applications.

Additionally, I investigate aqueous alcohols within hydrophobic nanopores using NMR. The self-assembly of water and alcohol into stable structures at hydrophobic interfaces is directly observed. This demixing phenomenon remains remarkably stable from -60 to 90 ℃ and its driving mechanisms are discussed. Moreover, microscopic segregation substantially influences macroscopic properties.

Last but not least, an NMR-based isotherm technique is developed for quantifying hydrophilic and hydrophobic characteristics of reservoir rocks. Water isotherms of the pristine rocks provide information on two important rock properties: wettability and pore size distribution. Overall, the NMR approach offers unique insights into the molecular mechanisms of nanoconfined fluids.

For my wife Yanmo and son Zile. Thank you for all your support on the way.

ACKNOWLEDGEMENTS

First and foremost, I would like to express my sincere gratitude to my advisor Professor Yue Wu for the endless support, motivation, and inspiration. He has been supportive since the days I began working on nuclear magnetic resonance which is quite difficult for a rookie. Under his supervision, I learned how to define a research problem, find a solution to it, and present your findings. Besides research, he is also a great friend, likes sharing interesting stories with us, chatting, and watching basketball games. It has been a privilege and a great journey to work with such a brilliant scientist and group leader.

I would also like to thank Professor Alfred Kleinhammes for being an incredible mentor and teacher, and for always being willing to discuss ideas or help with experiments, forever in good humor. I am also hugely appreciative to Dr. Horst Kessemeier, especially for sharing his research experience and life stories with me. I will remember those times when I show him how to do copy and paste in the Word, insert an image inline in an Email, and increase speaker volume on his computer.

Besides my advisor, I would like to express my deepest appreciation to my committee: Prof. Sean Washburn, Prof. Theo Dingemans, Prof. Luchang Qin, and Prof. Jianping Lu, for their encouragement, insightful comments, and offering helpful advice on my dissertation.

I would like to express my special gratitude to our collaborator Dr. Hyung T Kwak and Dr. Jinhong Chen in Saudia Aramco, who provide me financial support grant and help me a lot

in the oil project. In addition, thank you to Professor Yao Yu, Xun Liu, and Liang Peng, who helped me a lot with NMR experiments in Wuhan. I also thank Antoinette Setari, Maggie Jensen, Julia Green, Brianna Torres, Dr. Amar Kumbhar, and other staffs in the Department of Physics and Department of Applied Physical Science, who have provided numerous supports through the years.

It has been a great time working with Wu group members over the last five years. To Zhixiang Luo, thanks for enlightening me the first glance of NMR. To Yunzhao Xing, thanks for discussing simulation and helping me with the magic angle spinning tests. To Yuan Chong, thanks for teaching me how to use the adsorption isotherm system and helping me a lot on paper writing. To An Yao, thanks for the day and nights we were working together on oil projects. To Patrick Doyle, thanks for your help with the experiments and your patience with us. To Enyi Chen and Weiming Yang, thanks for those happy hours in every Chinese restaurant in NC and for the happy trips to Houston, DC, and Atlanta. To Arjun Raghavan and Vikram Aikat, it was a great pleasure working with you guys. To Shiyu Liu, thanks for those hot-pot times and a nice trip to New York City. Special thanks go to Yanchun Ling, for driving me to the supermarket before I got my own car and for the happy lunch and coffee times together.

The days would have passed far more slowly without the support of my friends. I would like to thank Qishun Tang, Lei Yang, Weida Gong, Muyang Wang, Qian Dong, Xiao You, Yaoyu Chen, Gang Li, Weizi Li, and Zhaopeng Xing, for their support, feedback, and friendship. A big thank you to my wonderful teammates in the UNC Chinese Basketball Team, for the exciting games and happy training times.

Last, but certainly not the least, I would like to thank my family: my parents Jihong Sun and Guangti Song, for their endless support and encouragement. You are always there for me. I also want to thank my wife Yanmo Li. I know there are many difficult times when I am not at home. Thank you for your selfless dedication to our family. I believe our love will last eternally. Finally, I want to say sorry to my son Zile Song. Sorry for not staying with you and sorry for missing those happy times. When you are grown up and able to read, hopefully, one day you would open papa's thesis and find the following sentence: "*My son, I love you forever!*"

TABLE OF CONTENTS

LIST OF TABLES

LIST OF FIGURES

LIST OF ABBREVIATIONS

BET	Brunauer-Emmett-Teller
CNT	Carbon Nanotube
CWA	Chemical Warfare Agent
DFT	Density Functional Theory
EXSY	Exchange Spectroscopy
FID	Free Induction Decay
FWHM	Full Width at Half Maximum
MAS	Magic Angle Spinning
MD	Molecular Dynamics
MOF	Metal-Organic Frameworks
NICS	Nucleus-independent Chemical Shift
NMR	Nuclear Magnetic Resonance
PPM	Parts Per Million
PFG	Pulsed Field Gradient
SEM	Scanning Electron Microscopy

CHAPTER 1 INTRODUCTION

Fluids in nanoscopic space are ubiquitous in nature, from hydrocarbons contained in porous rock formations to water tucked away in tiny crevices inside soil and buildings, and also in the biological world, especially in living cells and tissues. The enormous importance of nanoscopic fluids in diverse areas such as catalysis, energy storage and conversion, medicine, and more, has attracted extensive research activities, aimed at the understanding and application of fluids confined within nanostructures with at least one characteristic dimension below 100 nm.(*1, 2*) At such length scales, the surface-fluid interactions and spatial restrictions impart unique structural, thermodynamic, and dynamic properties that are not seen in the bulk fluid. For instance, gases and liquids that are normally isotropic in bulk can become anisotropic inside a nanometer-sized container if the shape of the container is nonspherical; miscible mixtures such as aqueous alcohol solutions become immiscible in nanoscale confinement under ambient conditions.(*3, 4*) Therefore, knowledge of the behavior of fluids in restricted geometries, with length scale comparable to molecular diameter, presents the possibility of learning new science as well as advancing technological developments.

Despite its importance, it has been a perpetual challenge to get an accurate and comprehensive picture of the structure, dynamics, and interactions of fluids in nanoscopic space. The porous networks are complex structures, and often comprise heterogeneous pore geometry and a variety of defects, making the properties of confined fluids difficult to describe. To this end, computational modeling has greatly enhanced our understanding of the molecular-scale behavior of both liquids and solids (surfaces) within the nanometre-sized pores. Meanwhile, advanced

characterization techniques such as X-ray, Raman spectroscopy, as well as quasielastic neutron scattering (QENS), have been used to picture the microscopic world.(*5-8*) Nuclear magnetic resonance (NMR) spectroscopy is one such method that has remarkable strength in looking into the inside of nano-sized pores (Figure 1.1). The key insight responsible for the superior strength of NMR to the confining system is that the surfaces of porous spaces have a strong influence on the magnetic field experienced by the in-pore nuclei, as well as their relaxation and diffusion properties.(*9, 10*) As a result, NMR is capable to provide both structural and dynamic information of confined fluids with atomic resolution, thus revealing intermolecular interactions, conformational information, mechanisms of adsorption and desorption, and transport phenomena.

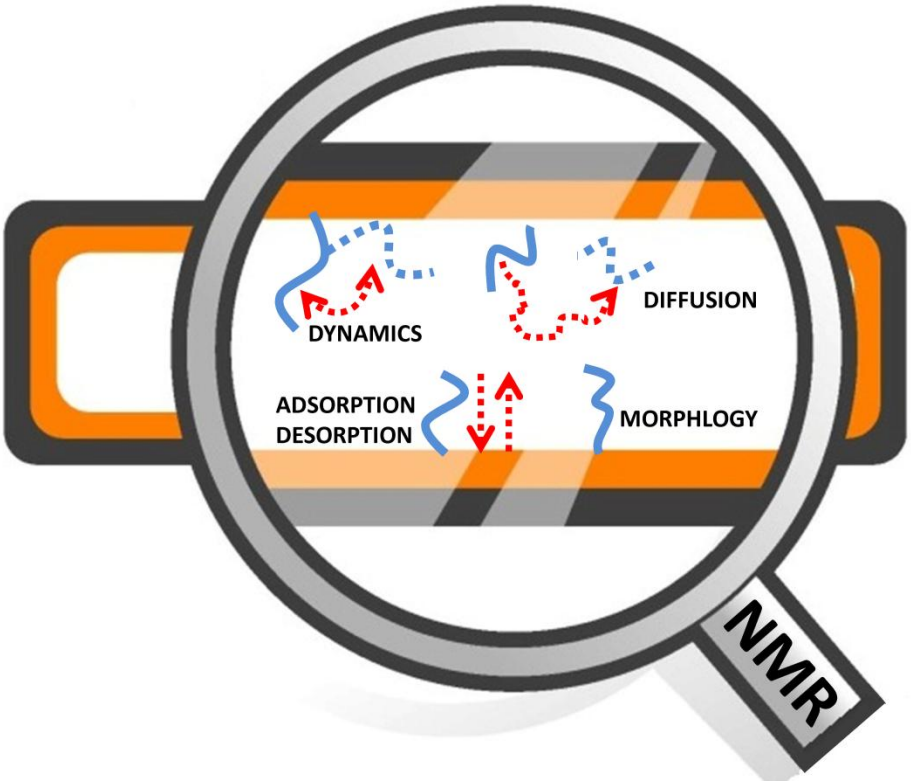

Figure 1.1 Schematic illustrating the main targets of NMR investigations in the field of nanoconfined fluids.

It is the topic of this dissertation to develop and apply the NMR as a complementary experimental tool to probe simultaneously the microscopic state, its evolution upon changing external parameters, and dynamics of fluids in nanoscopic spaces. The rest of the dissertation is organized as follows.

CHAPTER 2 presents what NMR can do in the field of confined fluids, and also reviews recent literature.

CHAPTER 3 introduces the essential concepts of NMR spectroscopy, NMR pulse sequences, and NMR imaging capability for a range of conjugated systems.

CHAPTER 4 presents the application of NMR spectroscopy to study nucleation and growth process of water adsorption in micropores of activated carbon.

CHAPTER 5 uses a combined NMR approach of NMR-detected isotherm and NMR imaging capability to explore adsorption-desorption hysteresis of water in hydrophobic nanopores.

CHAPTER 6 elucidates CWAs binding sites in MOFs and seeks to rationalize the effect of water on CWAs global uptake dynamics.

CHAPTER 7 investigates the phase separation of water and alcohols near a hydrophobic surface and discusses the corresponding driving mechanisms.

CHAPTER 8 develops an in situ NMR-based isotherm technique for quantifying the reservoir wettability.

CHAPTER 9 presents the main conclusions of this work and suggests new research directions.

CHAPTER 2 NMR INVESTIGATIONS OF FLUIDS IN NANOSCOPIC SPACE

Magnetic resonance originates from the Zeeman interaction between an external static magnetic field and nuclei that possess a nonzero spin quantum number, including ^{1}H, ^{13}C, ^{17}O, ^{19}F, *etc*. In addition, the nuclei interact with nearby electrons and atoms, resulting in subtle changes in the magnetic behavior of specific atomic nuclei. NMR spectroscopy manages to detect these local differences and takes advantage of them to elucidate the chemical structure, the interatomic distance, molecular dynamics, *etc*.(*11*) In general, the superior strength of NMR spectroscopy is manifested in four ways. First, NMR is intrinsically noninvasive and non-perturbative, allowing detailed study of materials in their pristine state without introducing any external disturbances, and in many cases, experiments may be performed in situ or in operando.(*12, 13*) For example, in situ NMR methodology has recently been developed to study structural changes that occur during the operation of a battery/supercapacitor.(*14*) Second, NMR is uniquely suited to study dynamic processes because of a broad time scale range, from rapid bond librations (picoseconds) to events that take seconds.(*15, 16*) For example, recent methodological advancements in NMR have extended our ability to characterize protein dynamics and promise to improve our understanding of protein dynamics and their relation to biological activity.(*17*) Third, NMR has imaging capability with sub-nanometer scale spatial resolution, and thus is able to provide atomic-level structural and conformational information for molecules ranging from small organic compounds to proteins.(*18*) Last but not least, NMR can selectively detect elements and can therefore simultaneously qualify and quantify the chemical

compositions. All these advantages are also applicable to the restricted regions and have made NMR a versatile tool for studying fluids in nanoscopic space.

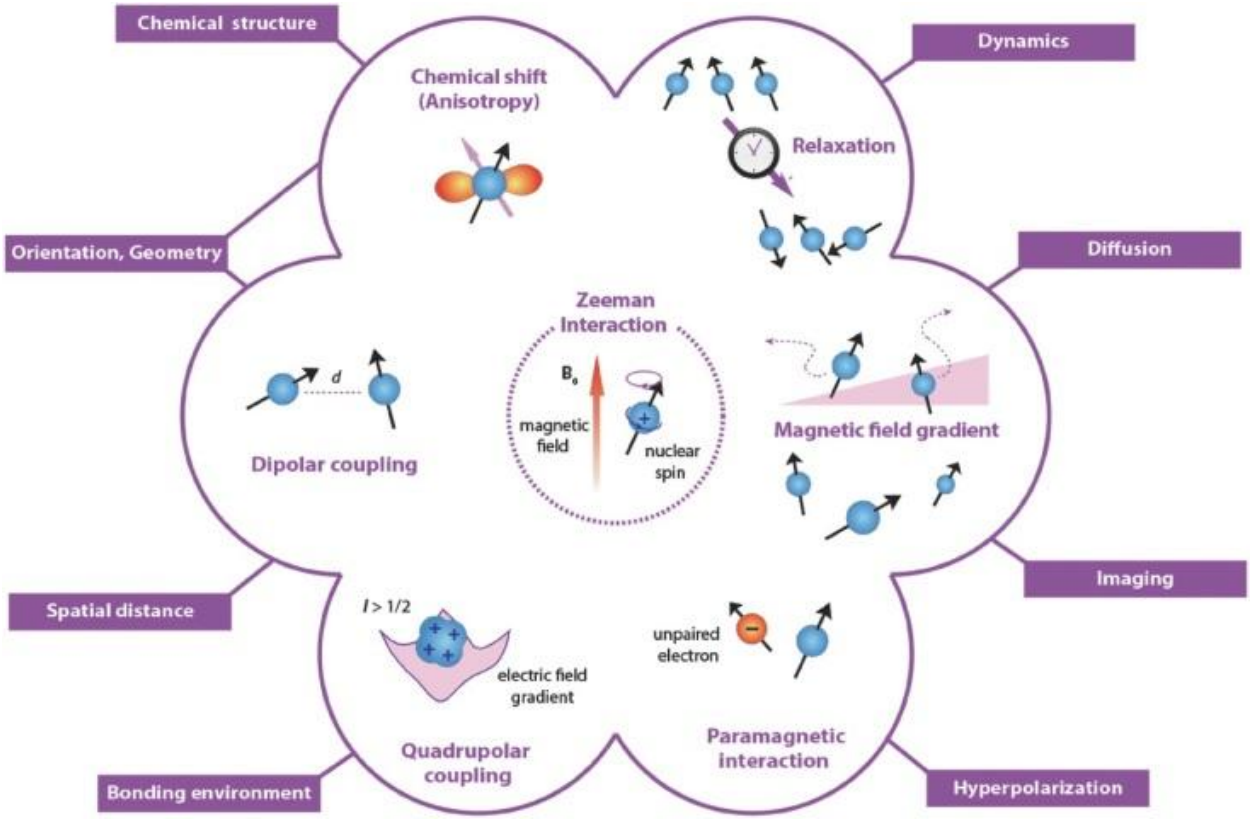

Figure 2.1 Illustrations of the physical phenomena in NMR and the underlying mechanisms for NMR characterization.(*11*)

Fluids in nanoscopic space are a broad area where chemistry, physics, and engineering intersect. In this chapter, we give an overview of NMR studies on nanoconfined fluids and highlight some recent advances in this field. In particular, in Section 2.1, we will discuss the applications of NMR to distinguish confined species from the bulk. Section 2.2 describes NMR exploration of molecular dynamics of fluids in porous materials. Section 2.3 introduces operando NMR spectroscopic analysis of reactions in restricted geometries. Section 2.4 and 2.5 discuss the applications of NMR to study host-guest interactions and to determine pore size distributions.

There are many more confined systems that are not included here but can still be studied by NMR, for example, fluids in biological related nanochannels and porous reservoir rocks.(*10, 19*)

2.1 Distinguishing In-Pore and Ex-Pore Fluids

One of the key capabilities of NMR spectroscopy for the study of nanoconfined fluids is the ability to distinguish species inside the nanopores (referred to as "in-pore") from those in larger voids and spaces outside of the nanopores (referred to as "ex-pore"). This capability is of crucial importance because it enables NMR to selectively and quantitatively study the properties of in-pore species.

2.1.1 Frequency-Based Signal Separation

The phenomenon of NMR itself is based on the occurrence of a precessional motion of nuclear spins in an external magnetic field. The Larmor frequency ω of the precession is given as the product of the magnetic field strength B and the gyromagnetic ratio γ of the nuclei under study. Due to the presence of pore surfaces, the in-pore nuclei may experience different B with the ex-pore nuclei, allowing frequency-based signal separation. A typical example is fluids within carbon nanopores. NMR studies of microporous carbon adsorbents found that resonances corresponding to in-pore species are shifted to lower frequency by several ppm as compared to the ex-pore free species. For example, Zhixiang Luo *et al.* studied $NaBF_4$ electrolyte in a microporous activated carbon with the average pore size of 0.9 nm from the wall surface to wall surface. Figure 2.2 plots the ^{19}F, ^{1}H, and ^{23}Na static NMR spectra of 30 µl 1 mol/kg $NaBF_4$ electrolyte in 20 mg activated carbon. All the ex-pore (free) electrolytes resonate at 0 ppm, while the in-pore (confined) electrolytes are at -7 ppm. Moreover, since the NMR signal is proportional to the number of spins, the numbers of ex-pore and in-pore ions can be quantified by the

corresponding nuclei peak intensities. The anomalous concentration difference between in-pore cations and anions indicated substantial electroneutrality breakdown in nanoconfined regions.

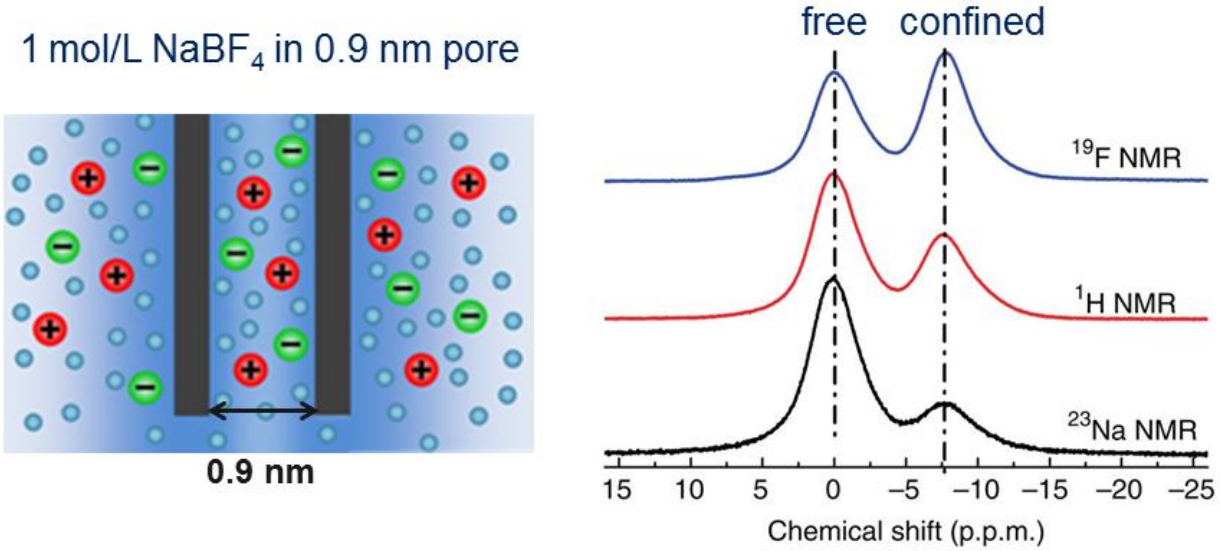

Figure 2.2 Left, a schematic model of electrolytes inside microporous activated carbon. Right, ^{19}F, ^{1}H, and ^{23}Na static NMR spectra of 30 µl 1 mol/kg $NaBF_4$ electrolyte in 20 mg activated carbon. The peak of ex-pore electrolytes is chosen as the reference (0 ppm).(*20*)

Similar observations have also been reported for species adsorbed within carbon nanotubes (CNTs).(*21*, *22*) For example, Xinhe Bao *et al.* studied ^{13}C-enriched methanol in multiwalled CNTs. Figure 2.3 shows the room-temperature ^{13}C MAS NMR spectra of the CNTs exposed to ^{13}C-enriched methanol at various vapor pressures. At 16 kPa (yellow curve), the ex-pore methanol peak is at 44 ppm, while the in-pore methanol is centered at 32 ppm. Based on the chemical shift difference, the amount of in-pore methanol can be quantified and the detailed adsorption mechanism of methanol on CNTs can be studied as well.

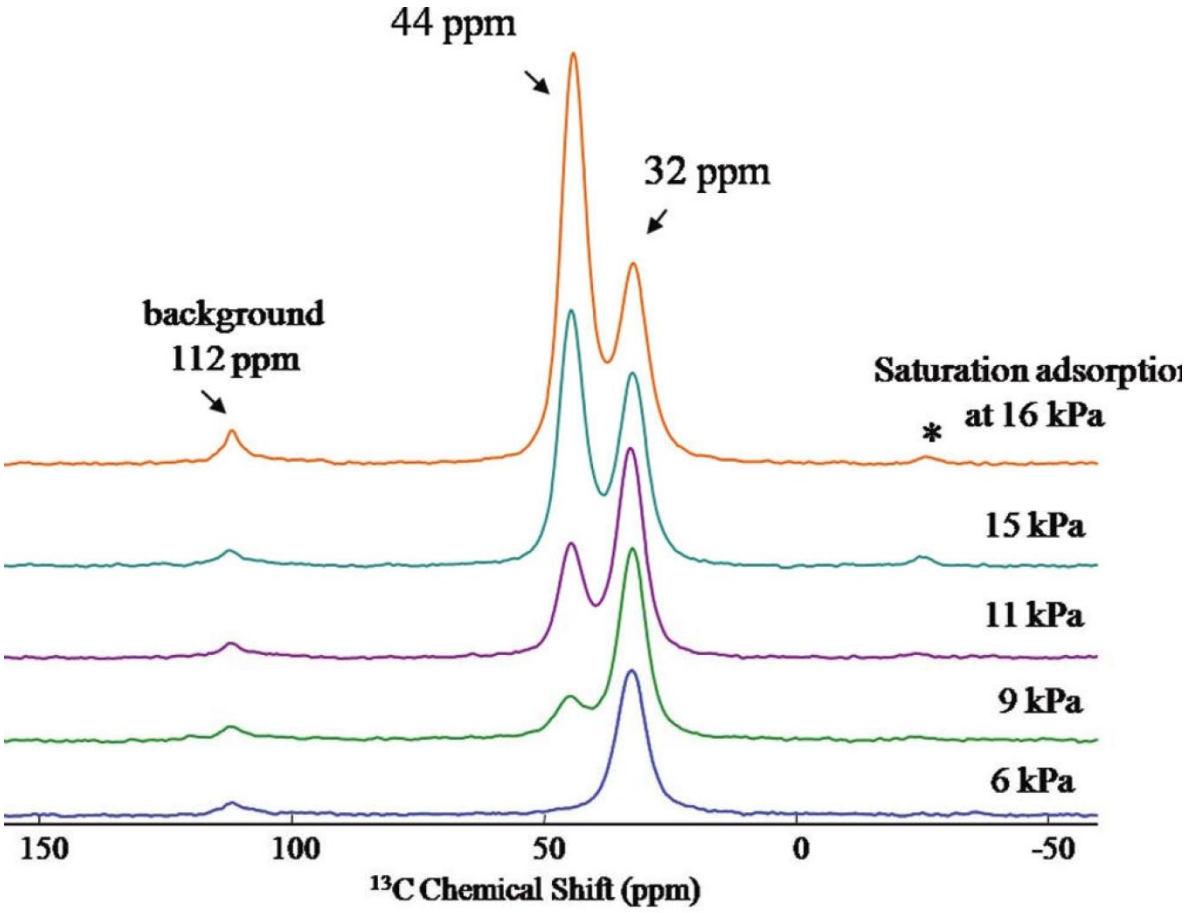

Figure 2.3 ^{13}C MAS NMR spectra of the methanol adsorbed in CNTs as a function of methanol vapor pressure at room temperature.(*21*)

2.1.2 Relaxation-Based Signal Separation

Besides the chemical shift difference, the in-pore and ex-pore fluids can also be identified by NMR through relaxation measurements. For example, Alfred Kleinhammes and coworkers applied NMR to study ethane in single-walled carbon nanotubes (SWNTs).(*23*) The spin-spin relaxation was measured with the Hahn echo pulse sequence 90°-τ-180°-τ-echo. Figure 2.4 shows the decay of ^{1}H Hahn-echo intensity as a function of the dephasing time 2τ for ethane at 0.093 MPa measured at 4.7 T. It clearly shows two components of exponential decays, T_{2a} = 0.125 ms and T_{2b} = 2.8 ms. The component with T_{2a} is assigned to in-pore ethane adsorbed inside SWNTs whereas the much longer T_{2b} corresponds to free ethane gas.

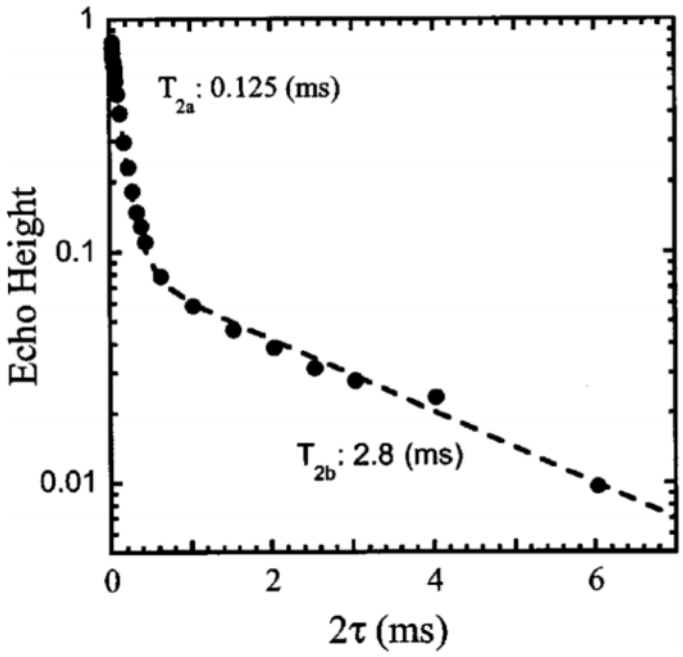

Figure 2.4 Decay of the 1H Hahn-echo intensity at room temperature as a function of dephasing time 2τ measured for ethane gas at 0.093 MPa in contact with cut SWNTs at 4.7 T. The dashed line is a fit using double exponential decays.(*23*)

2.2 Monitoring Microscopic Diffusion of Fluids under Confinement

Self-diffusion which characterizes the random translational motion of molecules under equilibrium conditions is a key parameter for determining the mass transport in porous materials. Among various experimental techniques for studying self-diffusion, pulsed field gradient (PFG) NMR is a well-established methodology used to measure directly the self-diffusion coefficient of adsorbed molecules in porous media. This method is based on the creation of an initial coherence of the nuclei and on following its loss in an applied magnetic field gradient due to displacements of the nuclei. This displacement is determined by the gradient pulse details and is typically on the order of micrometers to nanometers.

As such an example, Figure 2.5 shows the adsorption isotherm for cyclohexane in Vycor porous glass and the corresponding diffusivities measured at different points of the isotherm.(*24*)

A schematic illustration of the in situ PFG NMR system is illustrated in Figure 2.5a.(*25*) The measured adsorption amount and diffusivities are consistent with each other, both exhibiting a hysteretic behavior. The convergence of isotherm and diffusion allowed us to identify a two-stage mechanism of the transient uptake in the hysteresis region, which turns out to be generic for porous materials. (i) At low pressures, in general, the entire pore space is accessible for gas to diffuse into the pore structure, making the dynamics purely diffusive. (ii) As the pressure increases, liquid droplets appear at various places in the pore structure, forming bridges between the pore walls. The formation of these bridges blocks the pore network and reduces the diffusivities.

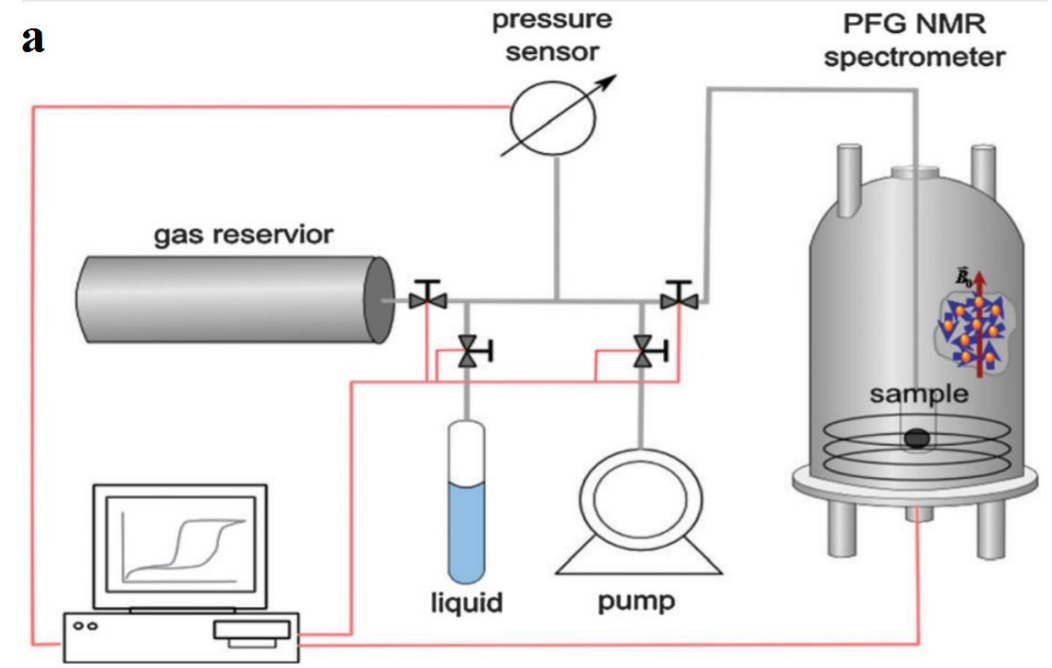
a
pressure sensor
PFG NMR spectrometer
gas reservior
sample
liquid
pump

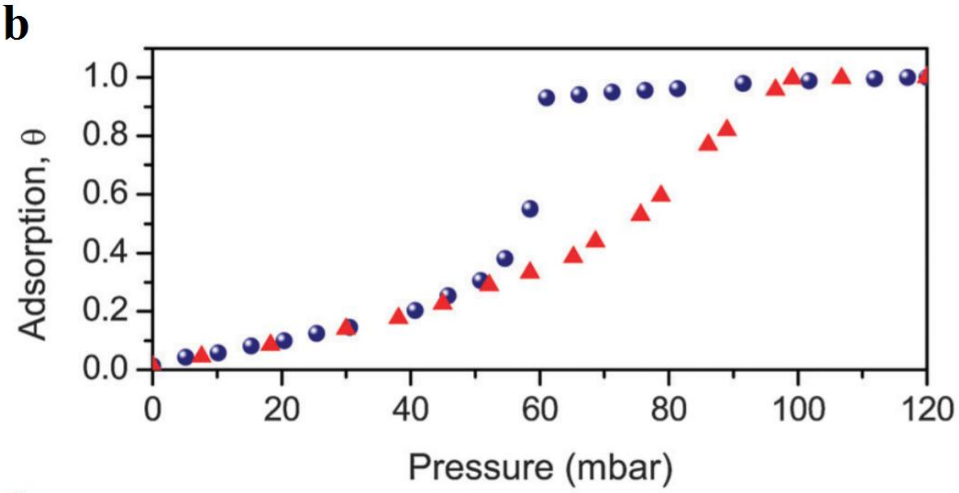
b
Adsorption, θ
1.0
0.8
0.6
0.4
0.2
0.0
0
20
40
60
80
100
120
Pressure (mbar)

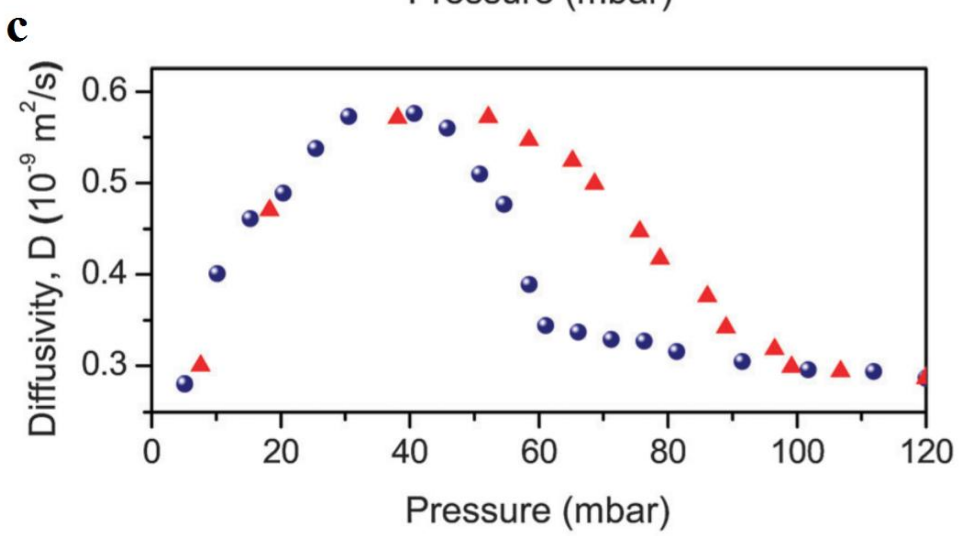
c
Diffusivity, D (10^-9 m^2/s)
0.6
0.5
0.4
0.3
0
20
40
60
80
100
120
Pressure (mbar)

Figure 2.5 (a) The schematic illustration of the in situ PFG NMR setup for simultaneously tracking the uptake amount and the diffusion characteristics of fluids in porous solids. (b, c) Normalized adsorption θ of cyclohexane in pores of Vycor porous glass (b) and the diffusivity (c) measured as a function of external vapor pressure on the adsorption (triangles) and the desorption (circles) branches of the isotherm at $T = 297$ K.(*25*)

Recently, in situ PFG NMR spectroscopy has been applied to measure the ionic diffusion in supercapacitors directly.(*26*) The ionic diffusion in the nanopores of electrodes is a decisive factor which determines the power performance of supercapacitors. As shown in Figure 2.6a, it is found that the nanoconfinement significantly decreases the self-diffusion coefficients $D_{\text{in-pore}}$ of in-pore ions (~10^{-11} to 10^{-12} m^2/s) by over two orders of magnitude compared with neat electrolyte (~10^{-9} m^2/s). Moreover, $D_{\text{in-pore}}$ in YP80F which has additional pore volume in the 1-3 nm range is ~4 to 5 times larger compared with YP50F. (See Figure 2.6b) These findings deepen our understanding of the interplay between the nanoporous structure of the electrode and ionic transport, and bring new opportunities for the design of enhanced supercapacitors.

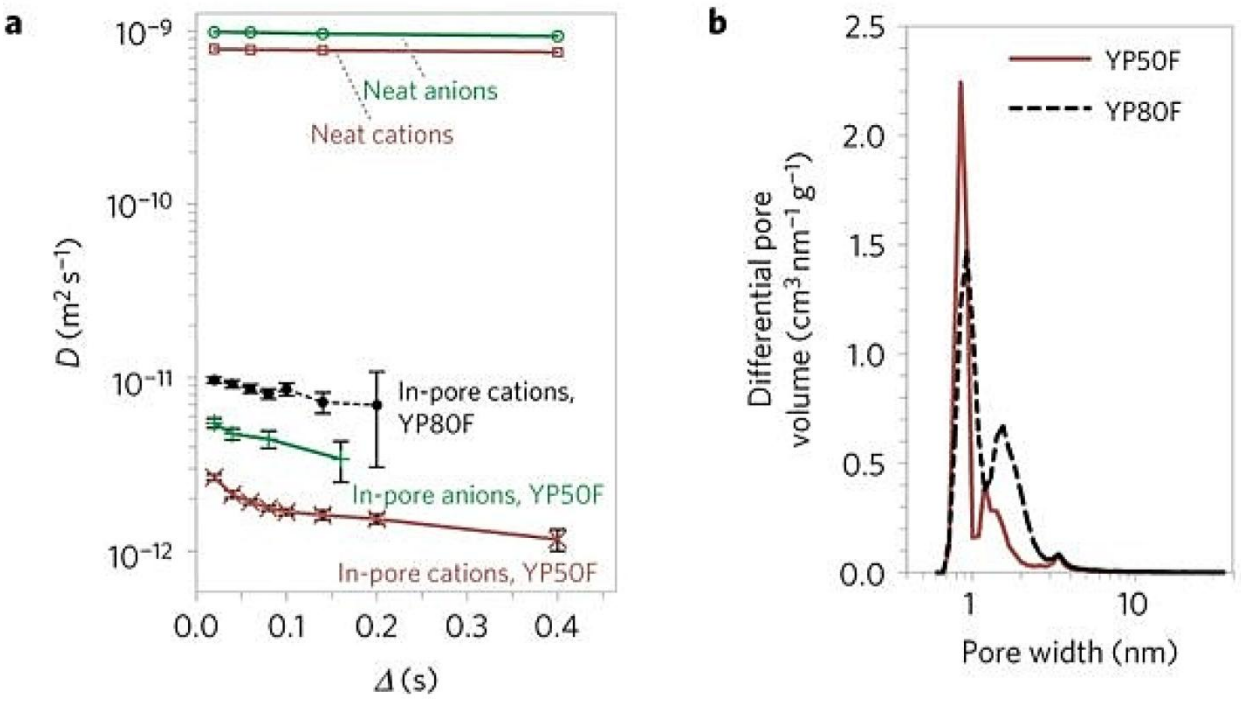

Figure 2.6 (a) Diffusion measurements for YP50F and YP80F supercapacitors, with 1.5 M PEt_4BF_4 in deuterated acetonitrile electrolyte. Measurements on neat electrolyte are also shown. (b) Pore size distributions of the two carbons YP50F and YP80F.(*26*)

2.3 In Situ Observing Chemical Reactions within the Nanospace

Reactions under confinement are the subject of continuing interest because the chemical nature of molecules and reactions within the nanospaces can be changed significantly due to the nanoconfinement effect and have various potential applications in optical and electrical devices, catalytic reactions, *etc*.(*27, 28*) Therefore, any noninvasive measurements that can probe the reaction in a confined space by in situ spectroscopy are of great significance. NMR is such a method which can elucidate the adsorbed reactants, intermediates and products inside nanopores and more importantly, can simultaneously provide the kinetic and dynamic information of the confined reactions.

For example, Shutao Xu *et al.* developed a new approach of in situ continuous-flow laser-hyperpolarized ^{129}Xe MAS NMR together with ^{13}C MAS NMR to study the adsorption and

reaction kinetics of methanol conversion in CHA zeolite with a cage dimension of 7.5 × 8.2 Å.(*29*) Figure 2.7a shows the in situ ^{129}Xe MAS NMR spectra recorded as a function of reaction time at 453 K. As increasing the reaction time, Xe in empty cage signal at 84 ppm decreases in intensity, while the signal at lower field splits into two peaks: Peak A at 92 ppm is from Xe co-adsorbed with methanol in CHA cages, while Peak B at 88 ppm is from Xe in the methanol reaction cage in which methanol molecules are converted to dimethoxyethane (DME) and water. (Equation 2.1) Moreover, the reaction kinetics can be directly obtained by plotting the concentration of $[\mathrm{Cage}]_{\mathrm{empty}}$ versus reaction time. (Figure 2.7b)

$$\mathrm{Methanol(g)} + [\mathrm{Cage}]_{\mathrm{empty}} \rightarrow \mathrm{DME\&H_2O@[cage]} \qquad (2.1)$$

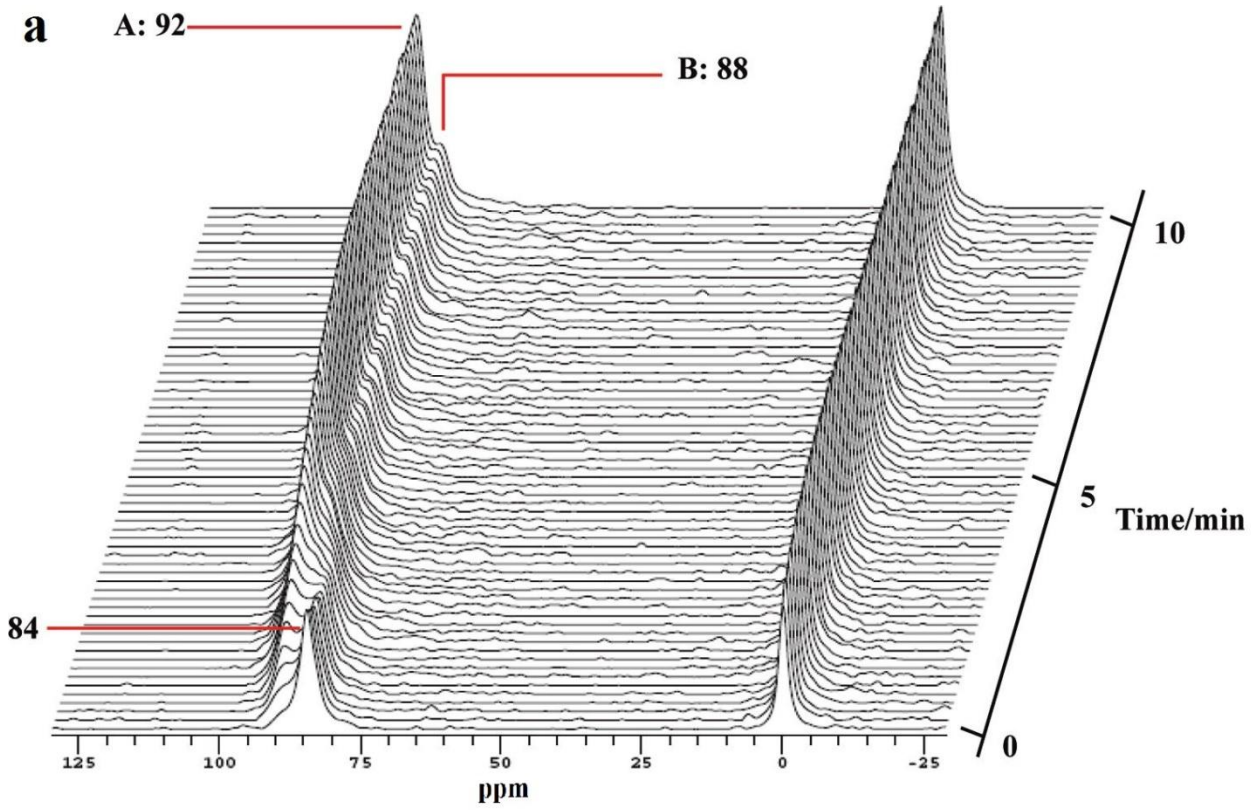
a
A: 92
B: 88
84
10
5
0
Time/min
125
100
75
50
25
0
-25
ppm

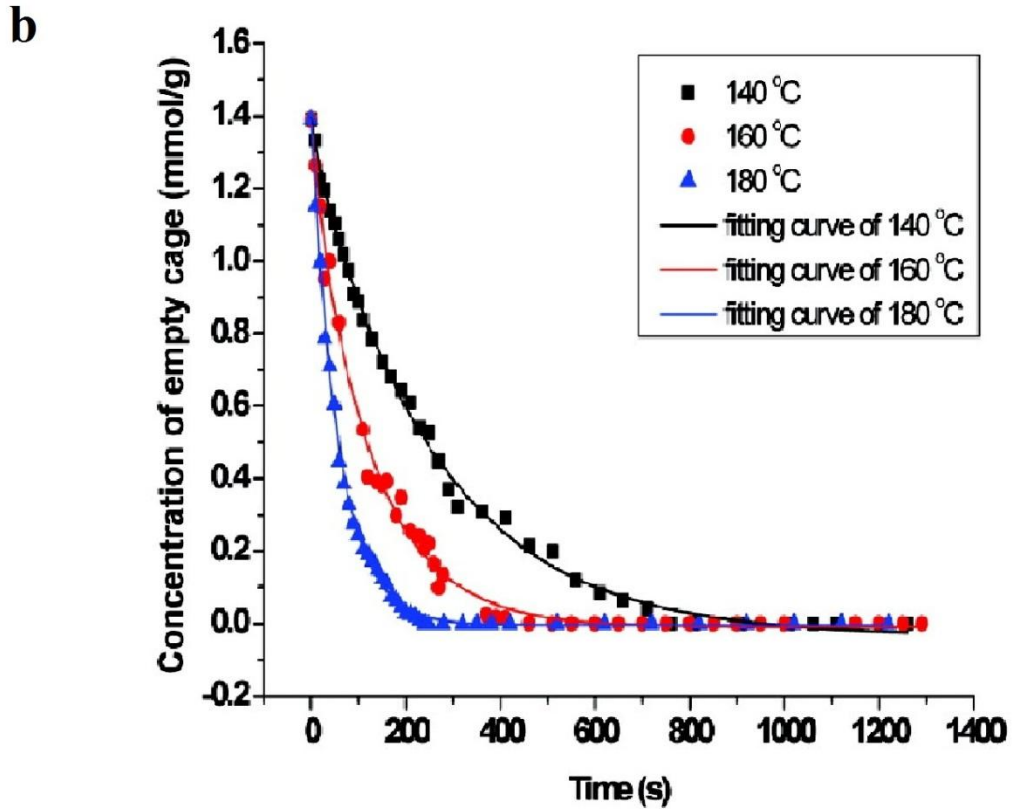
b
Concentration of empty cage (mmol/g)
1.6
1.4
1.2
1.0
0.8
0.6
0.4
0.2
0.0
-0.2
0
200
400
600
800
1000
1200
1400
Time (s)
140 °C
160 °C
180 °C
fitting curve of 140 °C
fitting curve of 160 °C
fitting curve of 180 °C

Figure 2.7 (a) In situ ^{129}Xe MAS NMR spectra recorded with a time resolution of 10 s per spectrum as a function of time during the reaction of methanol in CHA zeolite nanocages at 453 K. (b) Kinetic curves of methanol reaction in CHA zeolite nanocages at various temperatures.(*29*)

Chemical warfare agents (CWAs), *e.g.*, VX ([O-ethyl-S-(2-diisopropylethylamino)ethyl methylphosphonothioate]), are among the most toxic chemicals known to mankind. Recent global military events, such as the conflict and disarmament in Syria, have brought into focus the need to find effective strategies for the rapid decontamination of CWAs. Nanotubular titania (NTT) exhibits many desirable characteristics for the destruction of CWAs. Figure 2.8 shows the ^{31}P MAS NMR spectra obtained for VX added to NTT at the indicated times.(*30*) The appearance and growth of product EMPA peak (20.2 ppm) indicate the degradation of VX on NTT. Moreover, the VX peak (52.5 ppm) disappears after 4.9 h, indicating notably fast decontamination of VX. Further analysis on ^{31}P MAS NMR reveals that VX is adsorbed within the NTT tubules and/or its titania layers, perhaps providing optimum conditions for its hydrolysis by water sandwiched between the layers.

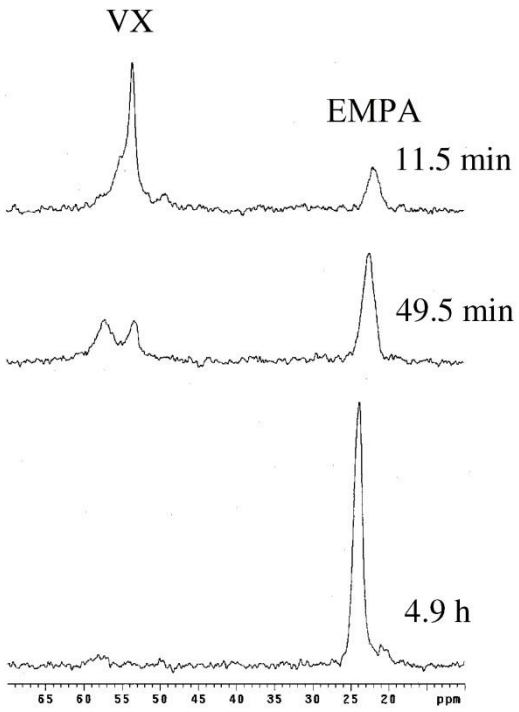

Figure 2.8 ^{31}P MAS NMR spectra obtained for VX added to nanotubular titania at the indicated times.(*30*)

2.4 Host-Guest Interactions in the Pores

The host-guest interactions between adsorbates and adsorbents play essential roles in many practical processes, including separation, catalysis, *etc*. The strength of the host-guest interactions could be further enhanced in restricted space due to the contribution from both pore walls. NMR can capture local environments through interpretation of NMR observables such as chemical shift and dipolar interactions, as well as motion-dependent parameters such as spin-spin relaxation time and spin-lattice relaxation. Those parameters are of great importance to provide information of the host-guest interactions in the pores.

MOFs as a new type of porous materials have been proved to be robust and effective for separation.(*31*) The separation mechanism is highly related to the host-guest interaction between MOFs and adsorbates. Recently, Shenhui Li *et al.* applied ^{13}C-^{27}Al double-resonance NMR to

probe the host-guest interaction between MIL-53 and styrene (St)/ethylbenzene(EB).(*32*) In particular, the host-guest interaction amplitude could be directly manifested from the relative dephasing ratios in the ^{13}C-^{27}Al rotational-echo saturation-pulse double-resonance (RESPDOR) experiment. Figure 2.9 shows the ^{13}C-^{27}Al S-RESPDOR NMR spectra of MIL-53 upon adsorption of St and EB. As shown in Figure 2.9a, the peaks at 137 and 130 ppm arising from the linker BDC, the peak at 125 ppm arising from the aromatic carbon of St show an obvious dipolar dephasing under ^{27}Al irradiation. In comparison, as shown in Figure 2.9b, none obvious dipolar dephasing is observed for all of the aromatic carbons as well as the ethyl group of EB. These results indicate that the host-guest interaction between St with MIL-53 is much stronger than that between EB with MIL-53, resulting in good separation performance.

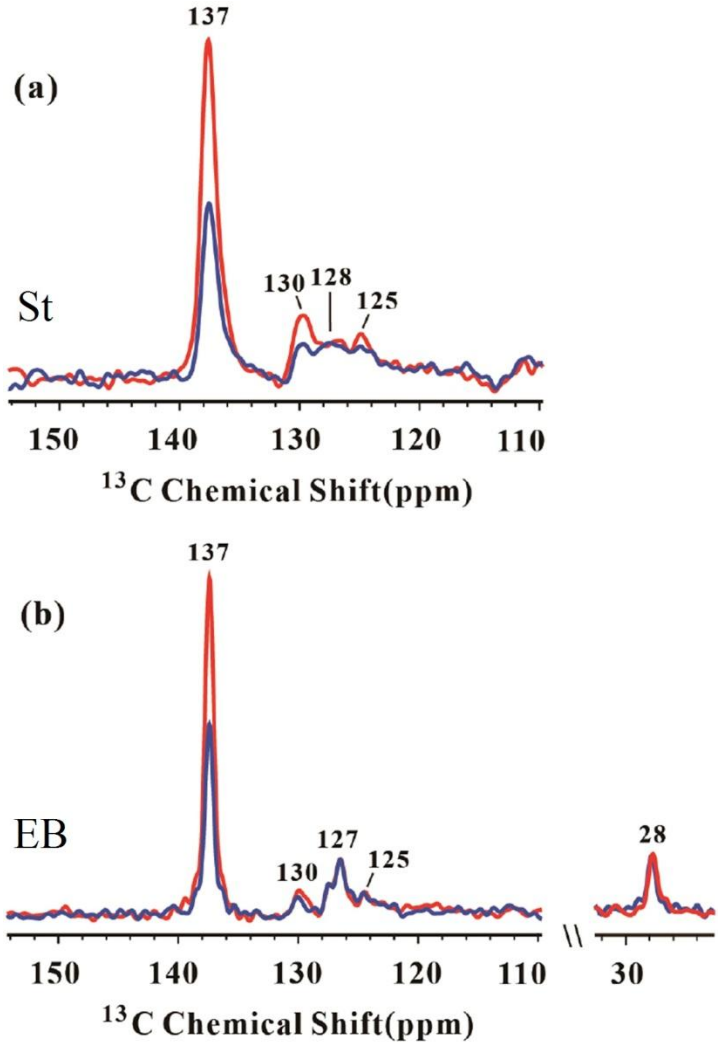

Figure 2.9 ^{13}C-^{27}Al S-RESPDOR NMR spectra of MIL-53 upon adsorption of (a) St and (b) EB. The blue and red lines represent the spectra of with and without ^{13}C-^{27}Al S-RESPDOR dipolar dephasing.(*32*)

2.5 Porosity Determination with NMR

Evaluating porosity, especially for micropores with pore size less than 2 nm, is a challenging and time-consuming task through adsorption measurement such as BET method. Several studies have demonstrated that NMR can potentially serve as a tool to analyze porosity. Those NMR-based porosity determination techniques take advantage of the unique properties of confined fluids and could greatly reduce the test time.

2.5.1 NMR Relaxometry of MOFs for Rapid Surface-Area Screening

In 2013, Chen *et al.* used ex situ NMR relaxometry for rapid estimation of the pore volume and surface area of an unknown MOF.(*33*) Figure 2.10a plots the profiles of T_2 relaxation times for Mg_2(dobdc) with different amounts of dimethyl sulfoxide (DMSO). DMSO is chosen as the probe solvent because of its common use in the synthesis of MOFs and its inert nature towards most compounds. The short T_2 is attributed to DMSO confined within the 1D channels of Mg_2(dobdc) (usually ~nm), while the intermediate and long T_2 are from DMSO in intergranular spaces (usually $\sim \mu m$). Since the signal area in the relaxation spectrum is proportional to the number of spins (i.e. solvent volume) of that relaxation population, a connection can be made between the pore volume and the relaxation behavior. Further studies of a variety of porous samples imbibed with DMSO or dimethylformamide (DMF) reveal a linear correlation between the NMR-predicated volume and the BET-determined area. These results demonstrate the potential for NMR relaxometry as a high-throughput technique for surface-area screening.

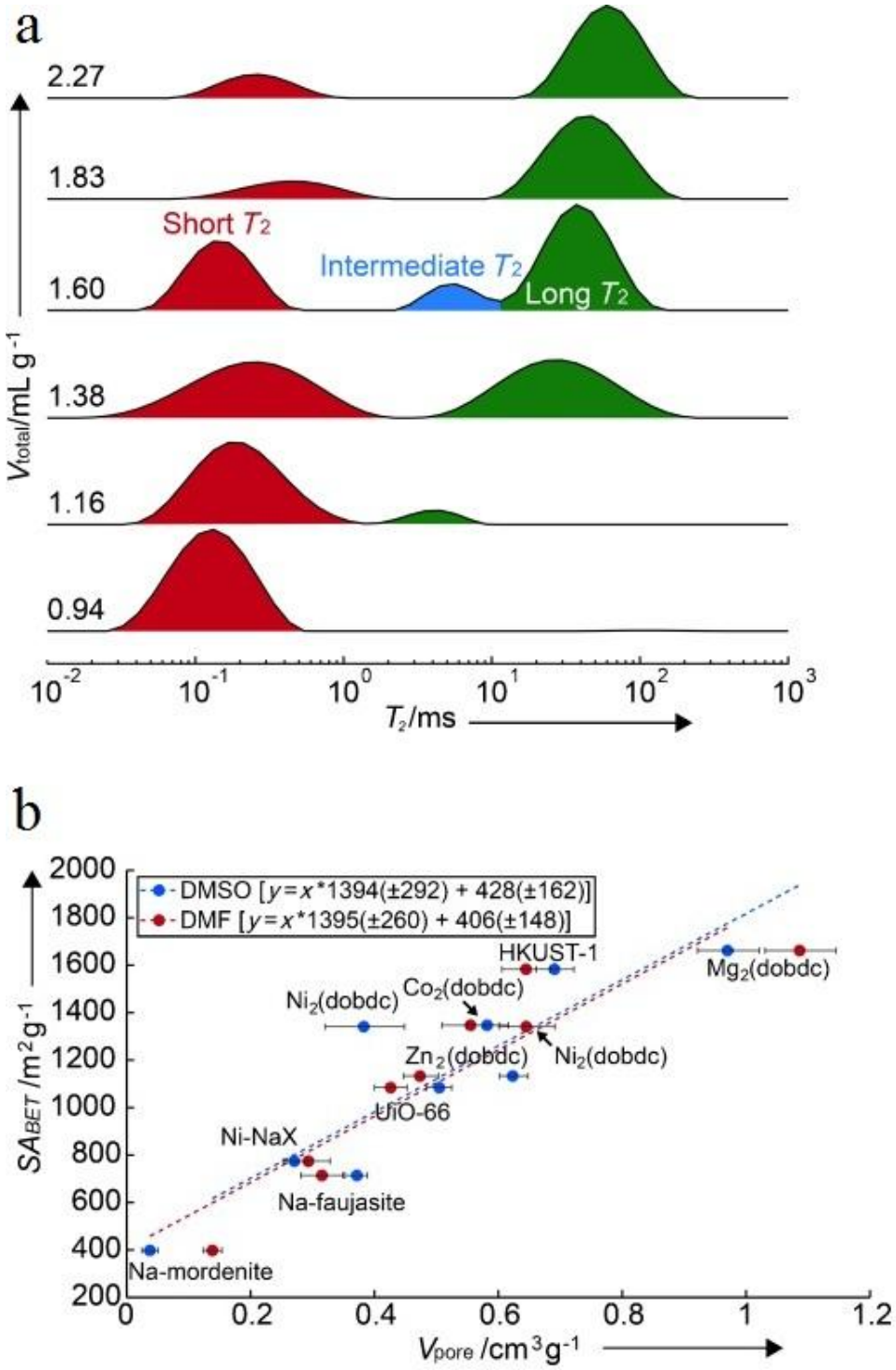

Figure 2.10 (a) Profiles of T_2 relaxation times for Mg_2(dobdc) with various amounts of DMSO added. Solvent content is normalized to the mass of the evacuated framework. (b) Correlation of BET surface area to the NMR-predicted pore volume using DMSO and DMF. Dashed lines indicate the fit for each solvent.(*33*)

2.5.2 NICS-based NMR Porometry Technique

Recently, Yunzhao Xing *et al.* developed a room temperature method to determine micropore size distribution of activated carbons based on ^{1}H NMR spectrum of adsorbed water under MAS, mostly suited for investigating pore structures of activated carbons smaller than 2 nm.(*34*) As discussed in Section 2.1, water confined within carbon nanopores experience a reduced magnetic field, and thus compared to the neat water, the chemicals shift of confined water is shifted to high-field by several ppm, which is called nucleus independent chemical shift (NICS). As shown in Figure 2.11a, DFT calculations demonstrate a straightforward relationship between the measurable NICS values with the micropore size, allowing for the determination of the micropore size distribution. Moreover, the pore volume can be calculated from the amount of in-pore water. Pore size distributions of a variety of activated carbon samples obtained from the NICS-based NMR porosimetry technique are shown in Figure 2.11b.

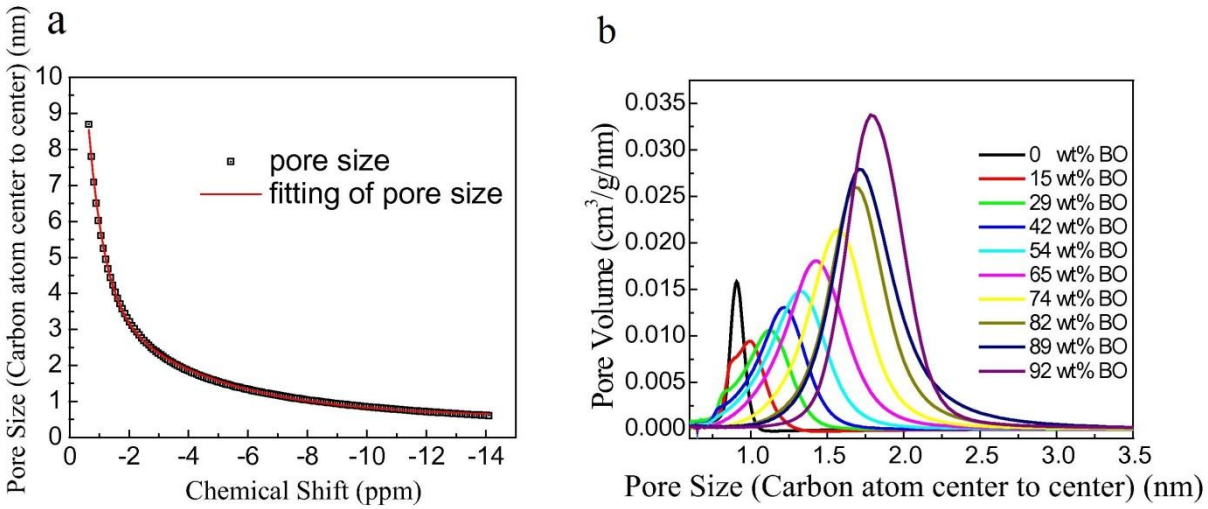

Figure 2.11 (a) Pore size as a function of averaged NICSs of confined water. (b) Pore size distributions of PEEK-derived activated carbon samples.

2.6 Aims of This Thesis

The main aim of this thesis is to develop and apply the NMR approach for studying the distinct physicochemical properties of fluids in the restricted space compared to the corresponding bulk systems. Specifically, the aims are to:

- Understand how the surface influences the NMR spectra of fluids within carbon nanopores.
- Investigate the structures of adsorbed water clusters inside carbon nanopores at different vapor pressures and related those to the water adsorption isotherm.
- Study the structural and dynamical differences between water clusters in the adsorption and desorption process and correlate it with the adsorption-desorption hysteresis of the isotherm.
- Carry out competitive adsorption of isopropanol and water on MOFs and quantify the relaxation dynamics associated with mass transport by direct measurement.
- Understand how the presence of interfaces affects hydrophobic phenomena, we also discuss the driving force for assembly in the vicinity of a hydrophobic surface.
- Develop the in situ NMR approach for the quantitative study of the reservoir rock wettability.

CHAPTER 3 NUCLEAR MAGNETIC RESONANCE SPECTROSCOPY

Nuclear Magnetic Resonance (NMR) spectroscopy is the main technique used in this thesis. This chapter starts with a short historical description of NMR. This is followed by a description of the NMR basics. The third part of this chapter gives an introduction of several important pulsed NMR techniques. Section 3.4 describes the ring current effect which is a fundamental concept to understand the NMR properties and aromaticity for conjugated systems, such as activated carbons.

3.1 A Brief History of NMR Technique Development

I begin with a historical introduction of the discovery and development of NMR. NMR was first accurately measured and described by Isidor Isaac Rabi as far back as 1938. Rabi, who received the Nobel Prize in Physics in 1944, successfully detected NMR absorption in a molecule beam. Working at Columbia University in the 1930s, Rabi and his team succeeded in detecting the resonance peaks for both Li and Cl as predicted, as shown in Figure 3.1.(*35*) Rabi named this phenomenon "nuclear magnetic resonance".(*36*) However, such studies were limited to nuclei in small molecules under very high vacuum. The first successful demonstrations of NMR in the ordinary matter were published in 1946. Two independent groups led by Felix Bloch at Stanford and Edward Mills Purcell at Harvard simultaneously demonstrated NMR for the first time on liquids (water) and solids (paraffin), respectively.(*37, 38*) The importance of their discovery was recognized by the joint award of the 1952 Nobel Prize in Physics to Bloch and Purcell.

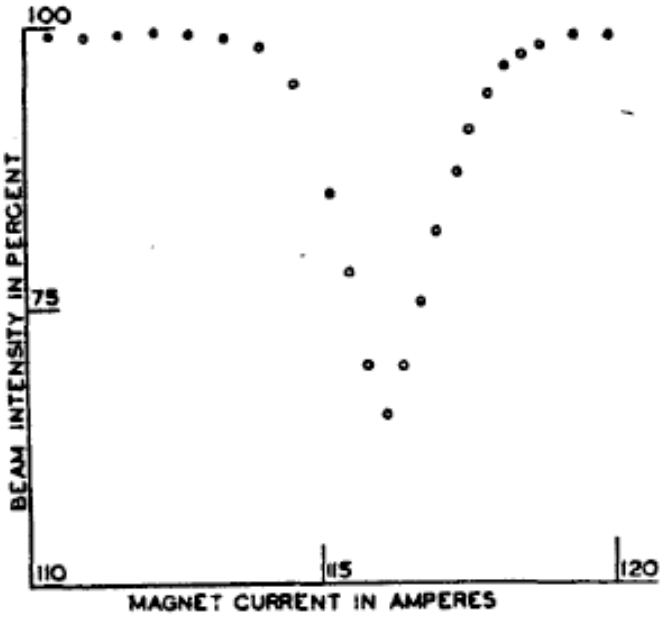

Figure 3.1 Resonance of LiCl from Isidor Rabi's 1938 paper.(*35*)

Since then, NMR spectroscopy has bloomed into a valuable analytical technique for the laboratory scientist, and magnetic resonance imaging (MRI) has become an indispensable medical diagnostics tool. Additionally, these developments have resulted in 4 Nobel prizes being awarded in the field of NMR.

1. Richard R. Ernst, Switzerland: Nobel Prize in Chemistry 1991, "*for his contributions to the development of the methodology of high resolution nuclear magnetic resonance (NMR) spectroscopy*".

2. Kurt Wüthrich, Switzerland: Nobel Prize in Chemistry 2002, "*for his development of nuclear magnetic resonance spectroscopy for determining the three-dimensional structure of biological macromolecules in solution*".

3. Paul C. Lauterbur, USA and Peter Mansfield, United Kingdom: Nobel Prize in Physiology or Medicine 2003, "*for their discoveries concerning magnetic resonance imaging*".

The history of NMR has been well summarized in some very readable reviews.(*39, 40*) In the following, the basics of NMR are described.

3.2 Basic Theory of NMR

3.2.1 Spin and Magnetic Properties

Matter is made of atoms. Atoms are made up of positively charged nuclei surrounded by a cloud of electrons. Each nucleus has an intrinsic physical property: spin, characterized by a nuclear spin quantum number, *I*. The magnetic moment that a nuclear spin with spin *I* possesses is:

$$\vec{\mu} = \gamma\hbar\vec{I} \tag{3.1}$$

γ is gyromagnetic ratio. The application of an external magnetic field $\vec{B}_0$, as it is in an NMR experiment, produces an interaction energy of the nucleus of the mount $-\vec{\mu}\cdot\vec{B}_0$. Therefore, the Hamiltonian for this system is:

$$\mathcal{H} = -\vec{\mu}\cdot\vec{B}_0 = -\gamma\hbar\vec{I}\cdot\vec{B}_0. \tag{3.2}$$

Thus, the allowed energies are:

$$E_m = -\gamma\hbar B_0 m.\ \ m = I, I-1, \ldots, -I+1, -I \tag{3.3}$$

For ^{1}H, and other nuclei with spin 1/2, there are two allowed energy states:

$$E_\alpha = -\tfrac{1}{2}\gamma\hbar B_0 \text{ and } E_\beta = \tfrac{1}{2}\gamma\hbar B_0, \tag{3.4}$$

with the α-spin state (m = 1/2) lower in energy than the β-spin state ($m = -1/2$) by $\gamma\hbar B_0$, as shown in Figure 3.2. In NMR spectroscopy, the transitions between these energy levels are observed as the Larmor frequency, ω_0, which is given by: $\omega_0 = \gamma B_0$.

For an ensemble of spin-1/2 nuclear spins, at thermal equilibrium, the ratio of populations follows a Boltzmann distribution:

$$\frac{N_\beta}{N_\alpha} = \frac{e^{-E_\beta/kT}}{e^{-E_\alpha/kT}} = e^{-\gamma\hbar B_0/kT}. \tag{3.5}$$

Thus the relative population difference is given by:

$$\frac{\Delta N}{N} = \frac{N_\alpha - N_\beta}{N_\alpha + N_\beta} \approx \frac{\gamma\hbar B_0}{2kT}. \tag{3.6}$$

Assuming protons in a 1 T field at T = 273 K, the relative population difference $\Delta N/N \approx 6 \times 10^{-7}$. In spite of its tiny magnitude, the spin population difference between the two states creates a macroscopic magnetization M, which is given by:

$$M = N\gamma\hbar \frac{\sum_{m=-1/2}^{1/2} m \exp(\gamma\hbar m B_0 / kT)}{\sum_{m=-1/2}^{1/2} \exp(\gamma\hbar m B_0 / kT)}. \tag{3.7}$$

In practice, $\gamma\hbar B_0/kT$ is a very small number. Therefore, the exponentials can be expanded as a power series, which is usually called *high-temperature approximation*:

$$M = \frac{N\gamma^2\hbar^2}{4kT} B_0 = \chi_0 B_0, \tag{3.8}$$

where χ_0 is the static nuclear susceptibility. This magnetization can be pictured as a vector-called the magnetization vector-pointing along the direction of the applied field $\vec{B}_0$, as shown in Figure 3.2. This is known as the vector model. This model has been around as long as NMR itself, and the language and ideas which flow from the model have become the language of NMR to a large extent. From now on we will only be concerned with what happens to this vector, and

in the subsequent section, we will use the vector model to describe how the most basic pulsed NMR experiment works.

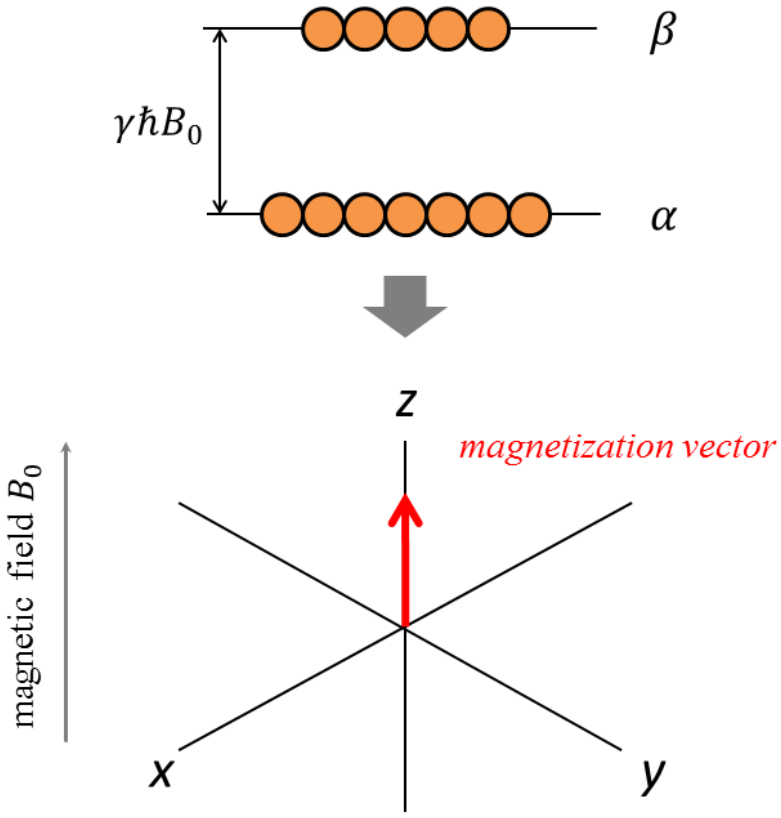

Figure 3.2 At equilibrium, the population difference creates a net magnetization along the magnetic field direction (the *z*-axis) which can be represented by a magnetization vector.

3.2.2 Relaxations

The bulk magnetization, which lies along the direction of the applied magnetic field, $\vec{B}_0$, can then be thought of precessing around $\vec{B}_0$ at the Larmor frequency. The time dependence of the magnetization $\vec{M}$ can be classically described by Bloch's equations:

$$\frac{dM_x(t)}{dt} = \gamma(\overrightarrow{M}(t) \times \vec{B}(t))_x - \frac{M_x(t)}{T_2}$$
$$\frac{dM_y(t)}{dt} = \gamma(\overrightarrow{M}(t) \times \vec{B}(t))_y - \frac{M_y(t)}{T_2} \quad , \tag{3.9}$$
$$\frac{dM_z(t)}{dt} = \gamma(\overrightarrow{M}(t) \times \vec{B}(t))_z - \frac{M_z(t) - M_0}{T_1}$$

where T_1 is the spin-lattice relaxation time, T_2 is the spin-spin relaxation time, and M_0 is the steady-state nuclear magnetization. Spin-lattice relaxation is concerned with the movement of spin populations back to their Boltzmann distribution values. Thus, spin-lattice relaxation is also known as longitudinal relaxation. Spin-spin relaxation is concerned with the decay of coherence; spin-spin relaxation is also known as transverse relaxation. One has to keep in mind that Bloch equations are macroscopic. These equations do not describe the motion of individual nuclear magnetic moments, which are governed and described by laws of quantum mechanics.

3.3 Pulse Sequences

Nowadays the majority of NMR experiments are done with radio frequency pulses. In the following, I describe the three most widely used pulse sequences: single pulse, spin echo, and inverse recovery.

3.3.1 Single Pulse Experiment

The longitudinal nuclear spin magnetization, described in Section 3.2.1, is almost undetectable. It is about four orders of magnitude less than the typical diamagnetism of the sample, associated with the electrons. Instead, NMR spectroscopy measures the magnetization perpendicular to the field, which is called transverse magnetization.(*41*)

First, we will deal with how to move the magnetic vector away from its equilibrium state. Rotation of the magnetization is achieved by the application of a radio frequency (RF) pulse,

which is an oscillating magnetic field with a frequency close or equal to the Larmor frequency of the nucleus under study. To describe the behavior of the nuclear spin magnetization, it is preferred to switch from the laboratory frame to the rotating frame where the *x*,*y*-plane rotates about the *z*-axis at the Larmor frequency. The axes of the rotating frame are labeled as *x´*, *y´*, and *z´*. As shown in Figure 3.3, the RF field generates a magnetic field $\vec{B}_1$ that is perpendicular to $\vec{B}_0$ in the rotating frame. Hence, according to Equation 3.10, in the rotating frame $\vec{M}_0$ will be flipped about $\vec{B}_0$ by a certain angle:

$$\theta(t) = t\omega_1 = t\gamma B_1, \tag{3.10}$$

which depends upon the duration of the RF pulse *t*. If the flip angle $\theta = 90°$, the longitudinal nuclear spin magnetization along the *z* axis is flipped to the *x*,*y*-plane, i.e. transverse magnetization. In the laboratory frame, the transverse magnetization precesses about the *z* axis. The precession frequency of the transverse magnetic moment is equal to the Larmor frequency of each individual spins. In NMR spectrometry, a receiver coil is placed in the *x*,*y*-plane to detect the induced current generated by the rotating transverse magnetization. This oscillating electric current induced by the precessing transverse magnetization is called the NMR signal or free-induction decay (FID), and Fourier transformation yields the NMR spectrum. (See Figure 3.4)

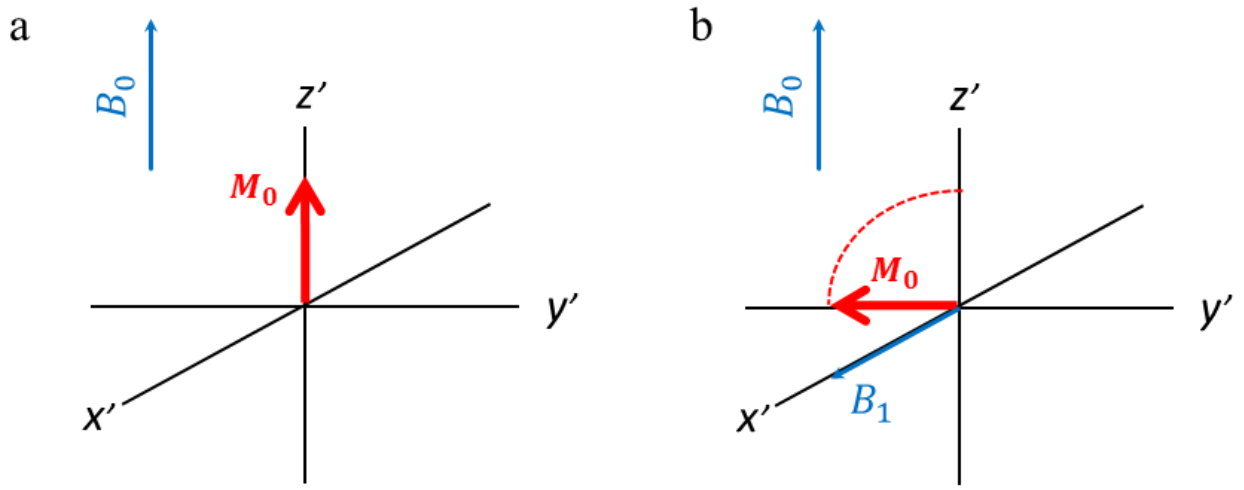

Figure 3.3 The vector model of NMR spectroscopy, viewed in the rotating frame. (a) equilibrium magnetization, (b) effect of a 90º pulse.

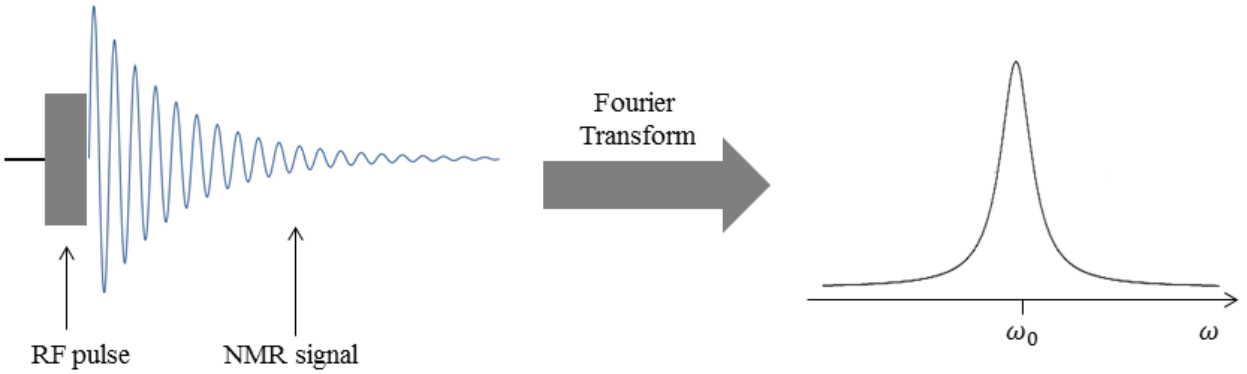

Figure 3.4 Illustration of a typical free induction decay (FID) signal. After the Fourier Transform, the spectrum in the frequency domain is obtained.

3.3.2 Spin Echo

Another commonly used pulse sequence is the spin-echo pulse sequence, which can be used to measure the spin-spin relaxation time T_2. The spin echo phenomenon was discovered by Erwin Hahn and can be counted among the most important developments in NMR history. The spin-echo pulse sequence consists of two RF pulses separated by a time interval τ. $2 * \tau$ is known

as the echo time. The 90°-τ-180°-τ-echo pulse sequence can be described in terms of the vector model, as shown in Figure 3.5.

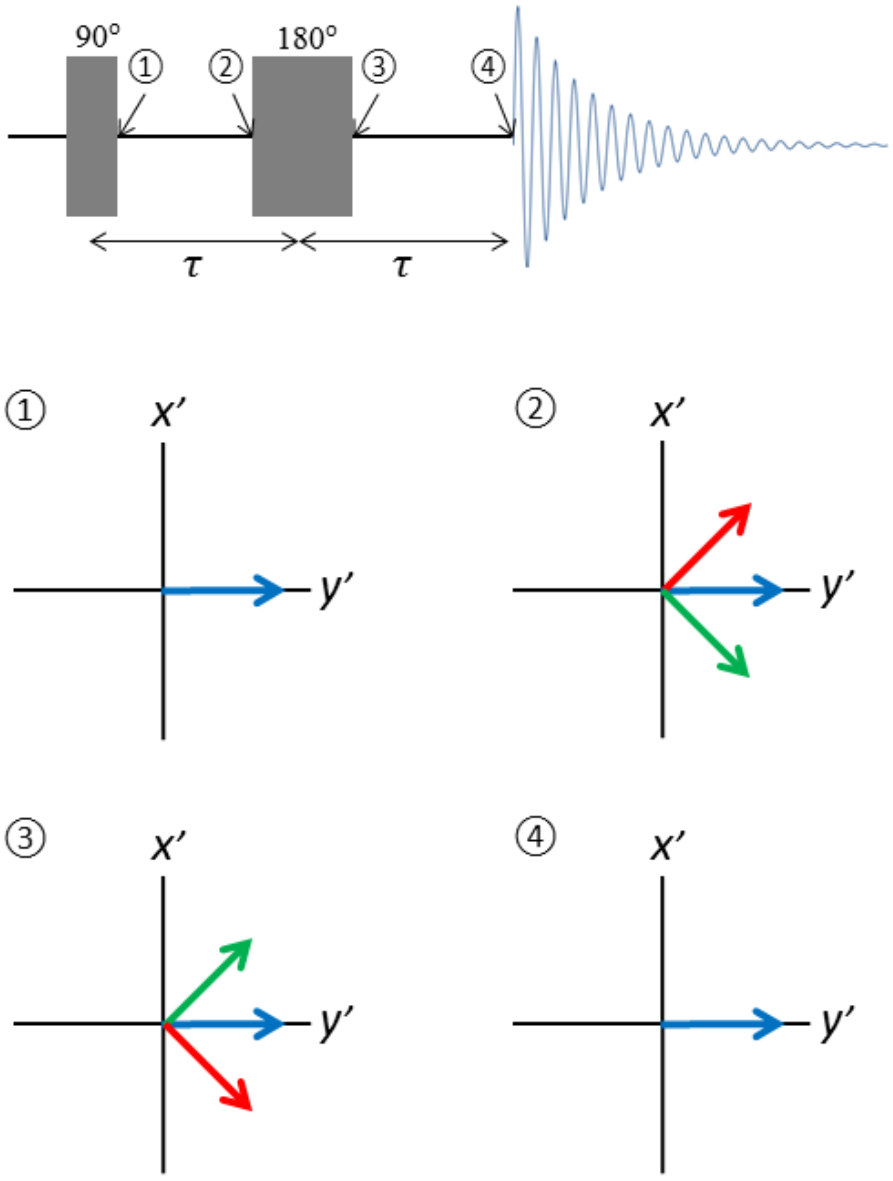

Figure 3.5 Pulse sequence and classical vector picture of spin echo experiment. Schematics show the change of magnetization vectors in the rotating frame for three sites with different offset frequencies at different time points of the pulse sequence.

The first pulse in the sequence is a 90° pulse and converts the initial longitudinal magnetization into transverse magnetization. During the first interval τ, the transverse

magnetization begins to dephase due to local magnetic field inhomogeneity: some spins may precess faster (green vector in Figure 3.5) relative to others (red vector in Figure 3.5) since the precession frequency of a particular spin is proportional to the strength of the magnetic field at the site. The dephasing leads to a loss in the total signal during the first τ interval. A 180° pulse is now applied and inverts the relative positions of the magnetization vectors belonging to strong and weak magnetic fields. After the pulse, the slower spins lead ahead of the main moment and the faster ones trail behind. With continued evolution, the faster precessing spins catch up with the slower spins. After the second τ interval, they all refocus simultaneously at the -*y*-axis, forming the echo. The T_2 relaxation time can be obtained by varying the time interval τ and fitting the echo intensity with the equation:

$$I(\tau) = I_0 \exp(-\frac{2\tau}{T_2}). \tag{3.11}$$

3.3.3 Inverse Recovery

The spin-lattice relaxation time T_1 can be measured by the inversion recovery experiment. In Figure 3.6, the inversion recovery pulse sequence consists of two RF pulses separated by an interval τ. First, a 180° pulse is applied. It inverts the net magnetization down to the -*z*-axis. Then an interval τ is left for the magnetization relaxes back towards the thermal equilibrium. Subsequently, a 90° pulse is applied which rotates the longitudinal magnetization into the *x*-*y* plane to record the size of the *z*-magnetization. Many experiments with different τ times are carried out, and the resulting signal, $I(\tau)$, is fitted to get T_1:

$$I(\tau) = I_0(1 - 2e^{-\frac{\tau}{T_1}}). \tag{3.12}$$

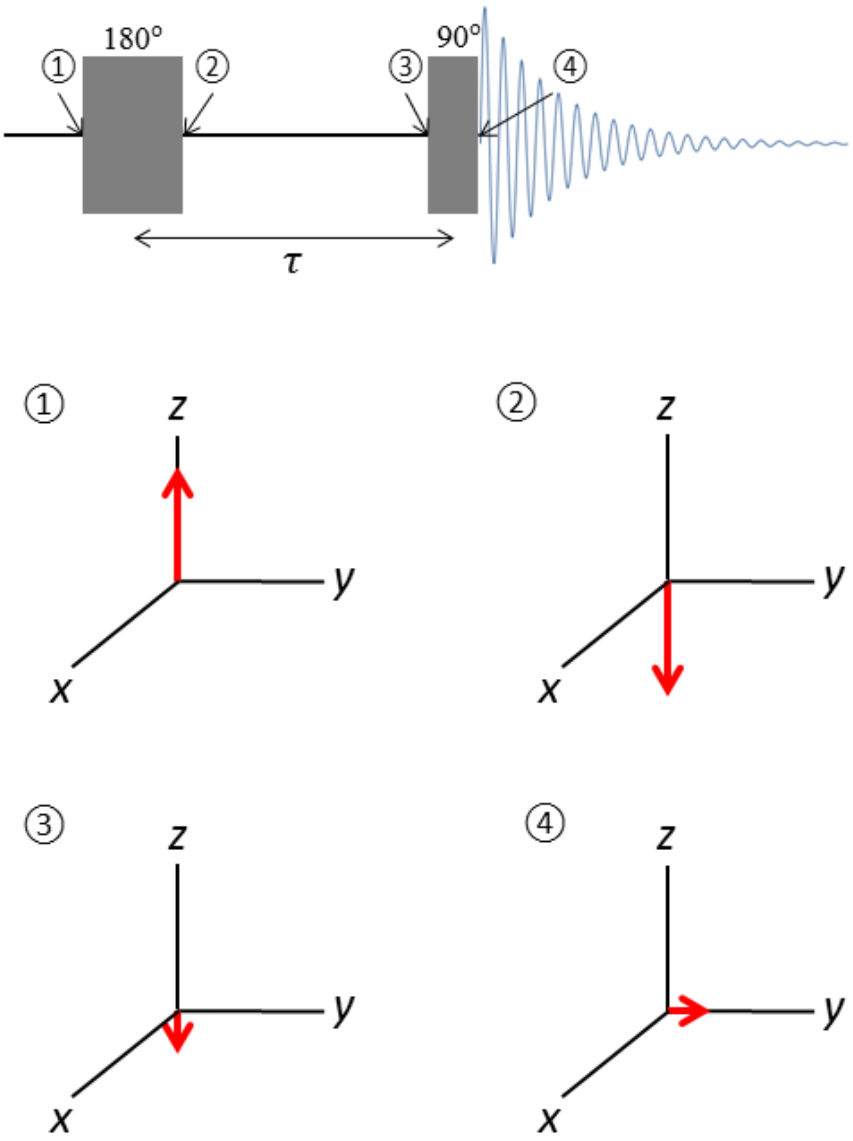

Figure 3.6 Pulse sequence and classical vector picture of the inverse recovery experiment. Schematics show the change of magnetization vectors in the laboratory frame at different time points of the pulse sequence.

3.4 Ring Current Effect

Since the primary objective of this thesis is to apply NMR to study confined fluids in conjugated systems, such as MOFs and activated carbon, it is important to consider what effect the delocalized electrons will give rise to the resonance frequency of the nanoconfined nuclear

spins. For example, activated carbon is known to be predominantly composed of carbon atoms that are arranged in 6-membered, hexagonal rings. Benzene is therefore chosen as a good model to exhibit the mechanism of ring current effect. As illustrated in Figure 3.7, when subjected to a magnetic field, benzene, consisting of cyclically delocalized electrons has a ring current and a resulting induced local magnetic field $\vec{B}_{\text{induced}}$. Even though such a ring-current is a quantum phenomenon which is fundamentally different from the classic (red loop), generally, it can be considered that $\vec{B}_{\text{induced}}$ is against the applied field $\vec{B}_0$, giving rise to a diamagnetic response above the plane of the benzene ring. Consequently, regardless of the nuclear spin studied, resonances arising from nuclear spins perpendicular to the carbon surface, *e.g.* the green nuclear spin in Figure 3.7, are shifted to lower frequencies relative to their free counterparts. Thus, the ring current effect is nucleus-independent to a first approximation.

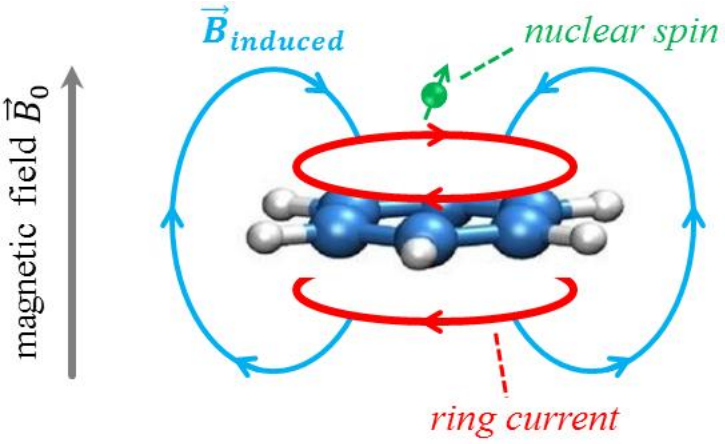

Figure 3.7 A diagram of the ring current effect in benzene. $\vec{B}_0$ is the applied magnetic field. The red ring shows the ring current, and the blue rings show the induced magnetic field $\vec{B}_{\text{induced}}$.

Recently, Yunzhao Xing *et al.* has applied DFT methods to calculate the NMR spectral features of nuclear spins above a graphitic carbon surface. The graphitic carbon surface was

mimicked by a circumcoronene molecule which is shown in Figure 3.8. The circumcoronene structure was optimized at the B3LYP/6-311G(d) level in Gaussian.

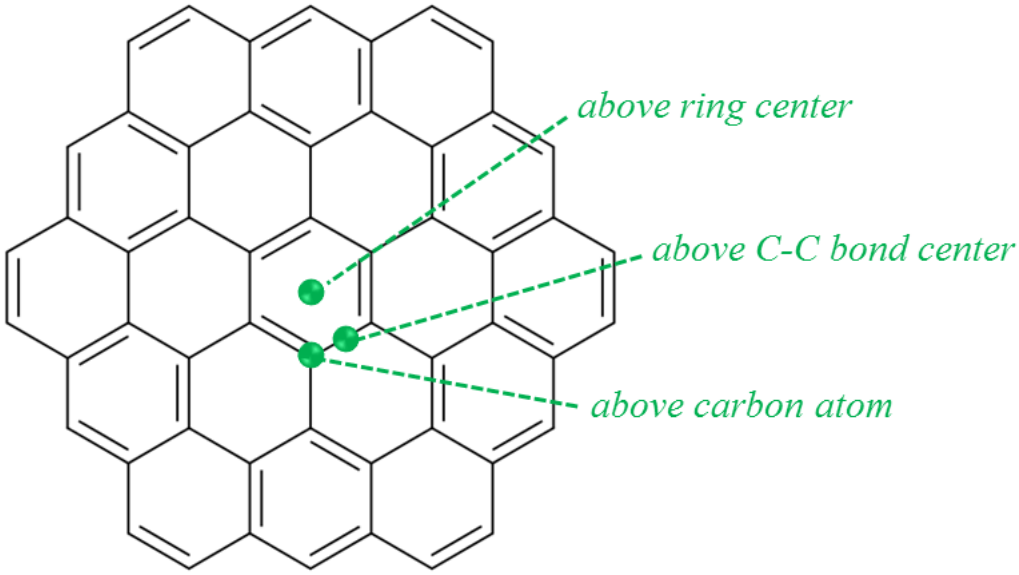

Figure 3.8 The graphitic carbon surface is mimicked by a circumcoronene molecule. Green dots are probe atoms at three different locations: above the ring center, above the carbon atom, and above the C-C bond center.(*34*)

In DFT calculations, the probe atom (green dots in Figure 3.8) is put at three different locations: above the ring center, above the carbon atom, and above the C-C bond center. Computed nucleus-independent chemical shift (NICS), δ, at three considered locations along a line perpendicular to the surface plane are plotted in Figure 3.9. First, negative NICS values were observed at all positions, meaning that the nuclear spins experience a shielded magnetic field in the proximity of the carbon surface. Second, the calculated NICS values at all the three locations are nearly identical, indicating that NICS value is independent of the horizontal position over the graphitic-like surface. For the purpose of convenience for future usage of the calculated $\delta(r)$, Yunzhao *et al.* fitted the calculated $\delta(r)$ in the region of 0.3 nm to 3.0 nm with a stretched

exponential function $\delta(r) = Ae^{-(\frac{r}{r_0})^{\beta}}$, where A = 24.5 ppm, r_0 = 0.227 nm, and β = 0.754. Such $\delta_{NICS} \leftrightarrow$ distance relationship provides NMR with very valuable spatial resolution near graphitic carbon surface.

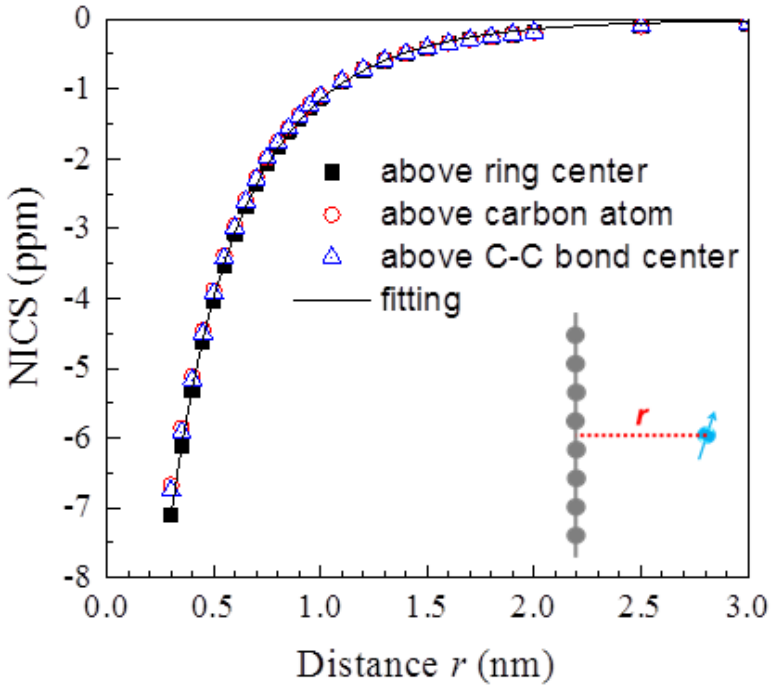

Figure 3.9 Calculated NICS $\delta(r)$ by DFT with the probe atom over the ring center, over the carbon atom, and over the bond center of the central carbon ring of circumcoronene. The solid line is an empirical fit of the numerical $\delta(r)$ with $\delta(r) = Ae^{-(\frac{r}{r_0})^{\beta}}$, where A = 24.5 ppm, r_0 = 0.227 nm, and β = 0.754.

CHAPTER 4 NUCLEATION AND GROWTH PROCESS OF WATER ADSORPTION IN MICROPORES OF ACTIVATED CARBON REVEALED BY NMR

4.1 Context and Scope

Activated carbons have gathered great attention owing to their wide applications, including gas storage, air purification, decaffeination, metal extraction, water purification, and many other applications.(*42-50*) They are inexpensive to produce and have a number of unique properties arising from their relatively small pore sizes, micropores (widths < 2 nm) or small mesopores (2-5 nm), and tremendously large internal surface areas.(*51*) In particular, activated carbons behavior in the presence of water is a decisive factor in determining whether real-world applications are realized.(*52*) Water vapor is ubiquitous in nature and in various industrial streams and must be accounted for when applying activated carbon for adsorption separation and purification systems. For example, the presence of water vapor severely handicaps the removal of volatile organic compounds (VOCs) from air due to the blocking of adsorption of VOCs by water clusters.(*53*)

The main aim of this chapter is to introduce NMR as a probe of water adsorption in microporous carbons and to demonstrate the key approaches and observations. In Section 4.1, I will first describe the definition of the isotherm. Subsequently, I will give an overview of water adsorption behavior in activated carbons. Experimental details and material preparations are summarized in Section 4.2. Finally, the application of NMR technique to study water adsorption in activated carbon is discussed in Section 4.3.

4.1.1 Classical Definition of Isotherm Types

Isotherm is the most common way to probe gas adsorption on porous materials. The adsorption isotherms are displayed in graphical form with the amount adsorbed plotted against the equilibrium relative pressure (P/P_0), where P_0 is the saturation pressure of the pure adsorptive at the operational temperature. Recommendations on the definition of adsorption isotherm types are outlined by an International Union of Pure and Applied Chemistry (IUPAC) report as shown in Figure 4.1.(*54*)

Three isotherm types are reversible: Type I, II, and III. Type I isotherms are concave to the pressure axis and the amount adsorbed approaches a saturation loading as $P/P_0 \sim 1.0$. The limiting uptake amount is governed by the accessible micropore volume rather than by the internal surface area. Type I isotherms are typically given by microporous adsorbents with strong adsorbate-adsorbent interactions. Type II typically corresponds to the gas adsorption on nonporous or macroporous solids and represents unrestricted monolayer-multilayer adsorption. Type III isotherms are convex to the P/P_0 axis across the entire range and also indicate a unrestricted multilayer formation process. It forms when adsorbate-adsorbate interactions are much stronger than adsorbate-adsorbent interactions.

Type IV and V are characterized by the hysteresis loop. Type IV isotherms are given by mesoporous adsorbents. In this case, gas adsorption proceeds via multilayer adsorption followed by capillary condensation. Type V isotherms are a combined result of relatively weak adsorbate-adsorbent interactions in the low P/P_0 range and pore filling in the higher P/P_0 range. Lastly, the reversible stepwise Type VI isotherm is representative of layer-by-layer adsorption on a highly uniform nonporous surface. Typical examples of this type are argon or krypton adsorbed on graphitized carbon black at 77 K.

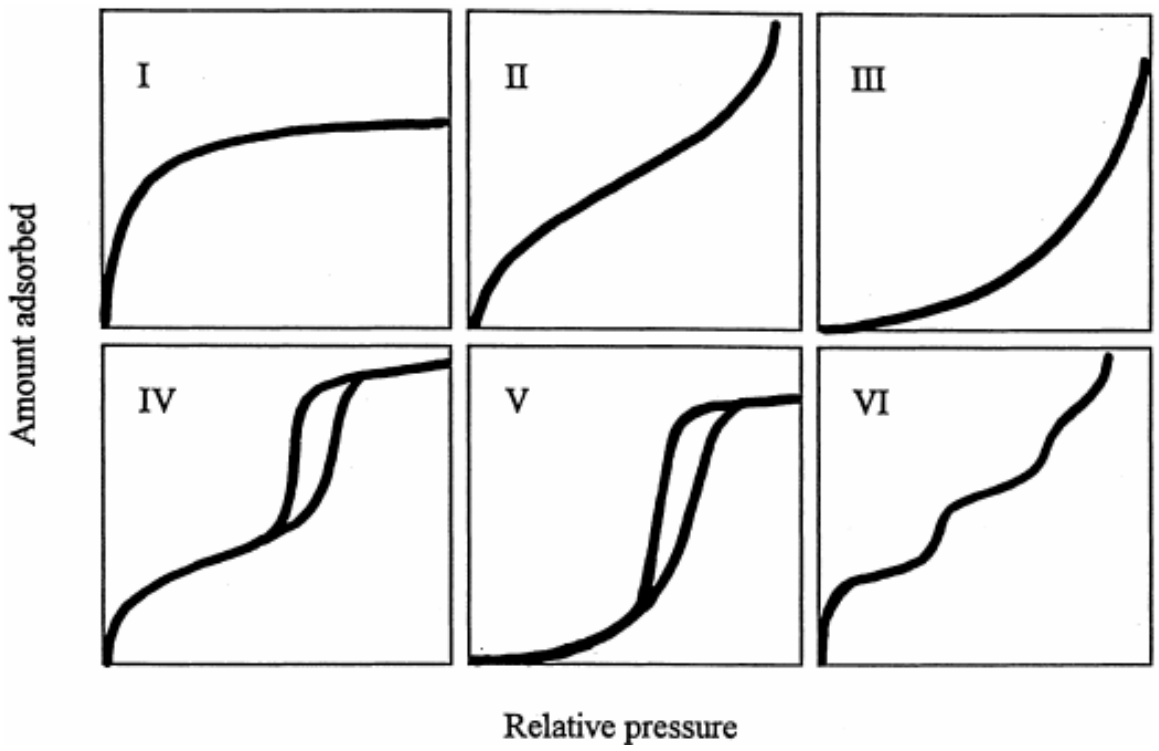

Figure 4.1 Classification of physisorption isotherms.(*55*)

4.1.2 Water Adsorption Isotherms on Nonporous and Porous Carbon

Activated carbon is characterized by small pores, micropores (widths < 2 nm) or small mesopores (2-5 nm), and hydrophobic surfaces. Consequently, the isotherms of water adsorption on activated carbon typically follow the Type V classification.(*56*) Therefore, in the following discussion, we are primarily concerned with Type V isotherms unless especially pointed out. However, some specially modified activated carbon samples are also known to exhibit other isotherm types. For example, Stefan Kaskel and co-workers have synthesized hydrophilic porous carbons by doping of the material with high ratios of N-groups in the graphitic frames. The materials exhibit marked adsorption uptake at low relative pressures, about 10 mmol/g at P/P_0 = 0.2, which corresponds to a high coverage of the pore wall surfaces.(*57*)

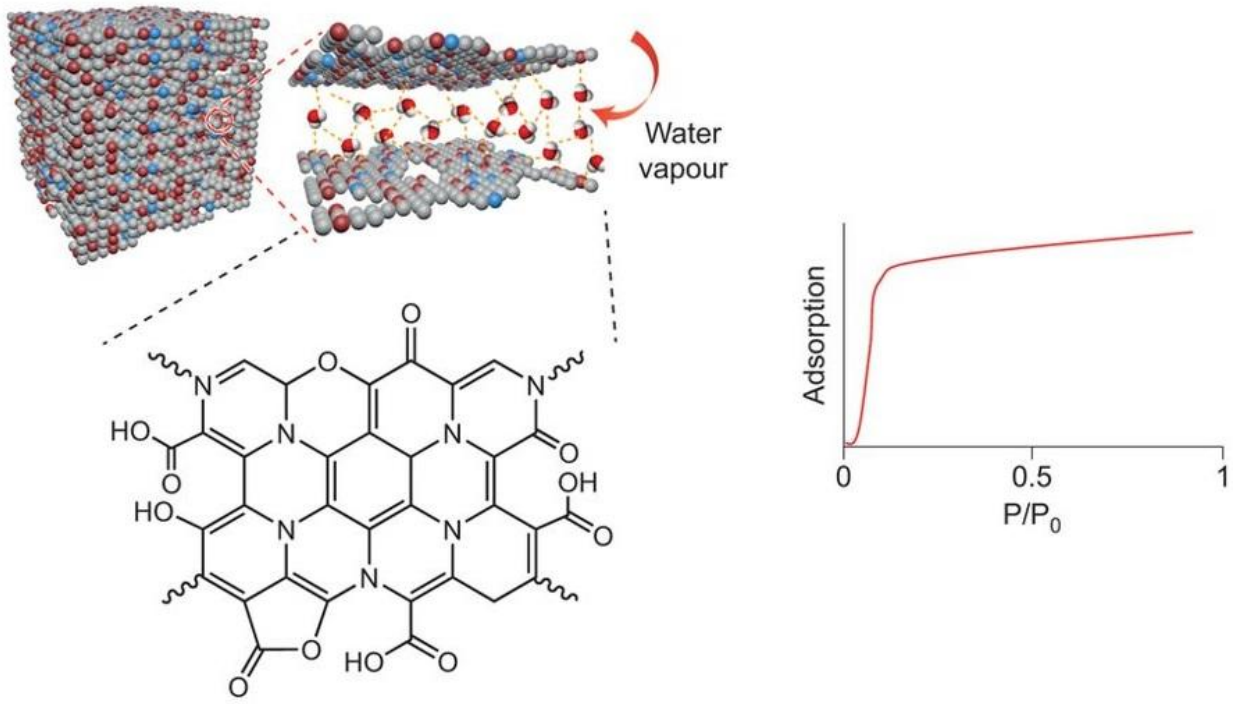

Figure 4.2 Left, model structure of the carbon cuboids, showing the heteroatom sites embedded in the graphitic sheets and water molecules filling the pores. The proposed structure of a typical sheet is shown below. Right, plausible adsorption isotherm of water in the carbon cuboid materials. Colour code of the atoms: grey, C; blue, N; red, O; white, H (omitted for clarity in the cuboid material).(*58*)

The graphitic surface is known to be hydrophobic. The contact angle of a water droplet on a fresh carbon surface is close to 90°. Isotherm results show that water vapor is not adsorbed on flat graphitic surfaces until it is approaching the saturation pressure P_0 (Figure 4.3).(*58*) This agrees with molecular dynamics (MD) and density functional theory (DFT) studies, which suggest that nucleation of water molecules are prohibited on such a hydrophobic solid.(*59-62*) However, activated carbons, though their surfaces are predominantly hydrophobic, they actually absorb water at pressures much lower than P_0.(*63*) A typical isotherm of water adsorption on activated carbon is shown in Figure 4.3. There is negligible water uptake at low P/P_0. Above a certain threshold pressure, typically around $P/P_0 = 0.5$, the amount of water adsorption increases

sharply and eventually reaches saturation. This unique adsorption behavior has gathered much attention since the pioneering work of Dewey *et al*. in 1932 and McBain *et al.* in 1933.(*64, 65*)

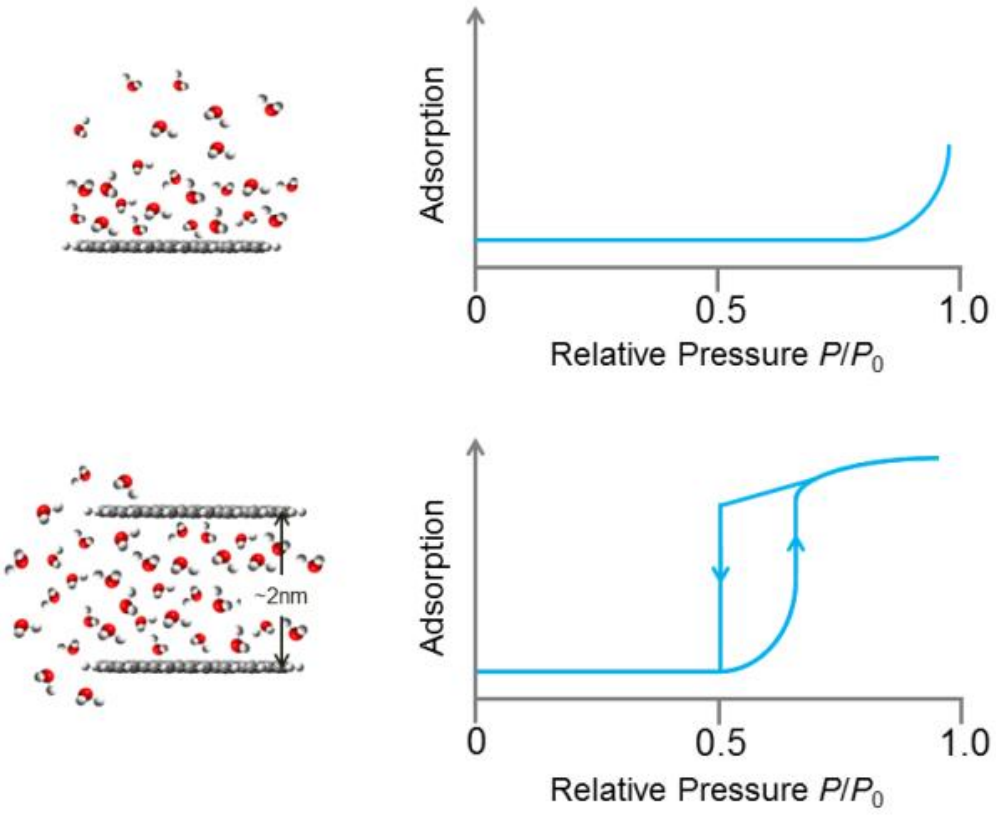

Figure 4.3 Top. Left, schematic representation of water adsorption on a flat graphitic surface; Right, typical isotherm of water adsorption on nonporous graphitic surfaces. Water adsorption is only observed at high relative pressure (P/P_0 ~ 1.0). Bottom. Left, schematic illustration of water adsorption on porous carbon; Right, typical water adsorption isotherm of carbon materials with micropores and small mesopores; significant water uptake has been observed at lower relative pressures (P/P_0 = 0.5-0.8).

4.1.3 Two Generic Mechanisms Explaining Water Adsorption on Carbonaceous Solids

Although further studies are needed to reach a firm understanding of the behavior of water in nanopores, currently there are two different mechanisms to explain this phenomenon. The first model proposes that the filling of carbon nanopores with water is a nucleation and growth process.(*63, 66-70*) It consists of multiple steps, including cluster formation, growth,

coalescence, and pore filling. On the basis of this scheme, some of the observed phenomena of water adsorption in carbonaceous materials of different pore sizes and at different temperatures can be readily explained. The other mechanism suggests that water uptake comes from losing the polar nature of the water molecules by cluster formation through hydrogen bonding.(*71-77*)

4.1.3.1 Nucleation-and-Growth Adsorption Mechanism

Figure 4.4 depicts the schematic of the nucleation-and-growth mechanism. At very low P/P_0, Stage I, since water does not directly adsorb on a graphitic surface, thus, defects, ultrafine crevices, and functional groups provide nucleation sites for the formation of stable water clusters. In terms of isotherm, as shown in Figure 4.5, the presence of nucleation sites shifts the onset of water adsorption to a lower relative pressure and also enhances the adsorption capacity. Additionally, at Stage I, the primary water clusters are likely to be small and separate, and to have convex interfaces.(*78*) Such convex interfaces are thermodynamically unfavorable to further growth. Therefore, those initial clusters cannot induce pore filling, as evidenced by the fact that condensation does not take place at low relative pressures.

As the pressure increases, Stage II, the initial nucleation clusters may grow and coalesce. In micropores, the growth of clusters can result in water bridges spanning the pore, which are supported by simulation studies.(*51, 66, 68*) On the other hand, in mesopores, since the pore size is bigger, the initial water clusters in Stage I continue to grow without inducing pore filling. This is consistent with isotherm results: pore filling occurs at P/P_0 = 0.3 in ultramicropores and at P/P_0 = 0.5 in micropores; while in mesopores the pore filling is delayed until P/P_0 reaches 0.8–0.9.(*79-82*) At Stage III and IV, the growth of water clusters completely fill the entire pore spaces. Therefore, adsorption occurs progressively from smaller to larger.

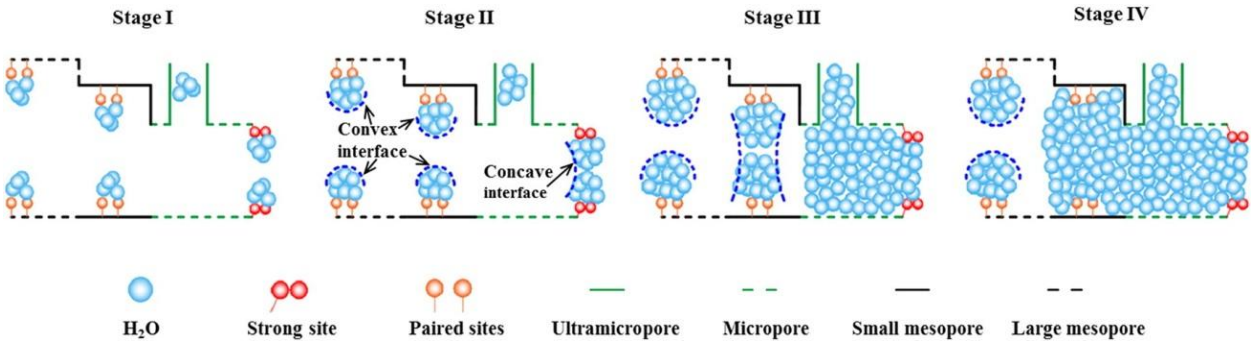

Figure 4.4 A schematic description of water adsorption in carbonaceous materials at stages I-IV.(*63*)

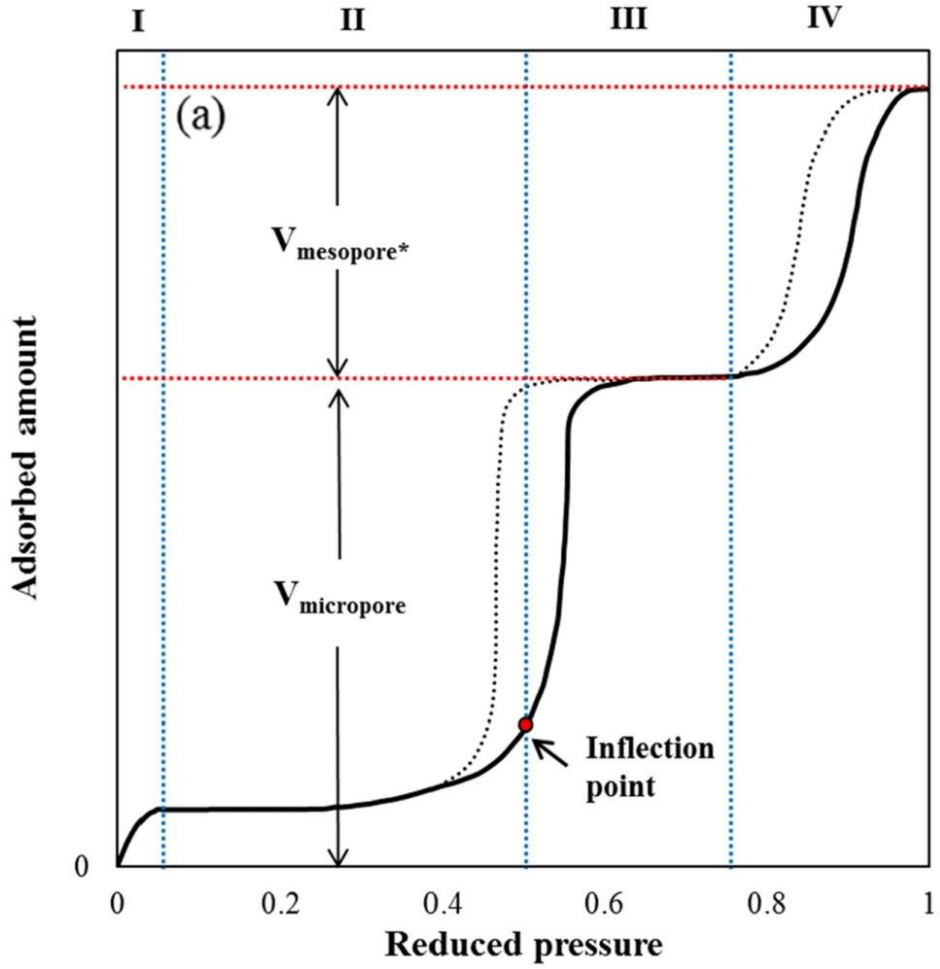

Figure 4.5 The generalized isotherm of water adsorption on carbonaceous materials. Stage I–IV: cluster formation, cluster growth and coalescence, micropore filling, and mesopore filling (the first two stages are magnified artificially). The schematic diagram of these stages is shown in Figure 4.4.(*63*)

4.1.3.2 Cluster-Associated Filling of Water in Hydrophobic Carbon Micropores

The nucleation-and-growth adsorption mechanism has been believed for a long time. However, similar adsorption appears for even microporous materials with a lower content of surface functional groups. To explain it, Kaneko and coworkers propose that the chemical affinity of water molecules can transform from hydrophilicity to hydrophobicity due to clusterization.(*71-77*) The cluster formation makes water molecules less hydrophilic because dipole-dipole interaction between water molecules reduces the dipole moment of the cluster as a whole. This reduction of hydrophilicity leads to higher affinity of water cluster for hydrophobic graphitic surfaces and induces further ordering of water molecules at filling.(*73*)

Figure 4.6 illustrates the cluster-associated filling of water in hydrophobic carbon micropores. When the water content is low, $0 < \phi < 0.1$, a small amount of water molecules can adsorb into the pores due to the slight molecule-pore wall interaction. Subsequently, more water molecules are adsorbed and small clusters are formed (Figure 4.6b).(*72*) At higher pressures, those clusters grow due to the enhancement of interaction between clusters and walls, which is confirmed by computational simulations. For example, Figure 4.7 shows the interaction potential of the clusters with the carbon nanopores.(*74*) A single water molecule interacts very weakly with the graphite slit pore. However, the greater the cluster size, the deeper the potential depth. This means once water molecules are associated to form a tetramer or a larger cluster, the cluster is remarkably stabilized in the nanopore to gain a marked hydrophobicity.

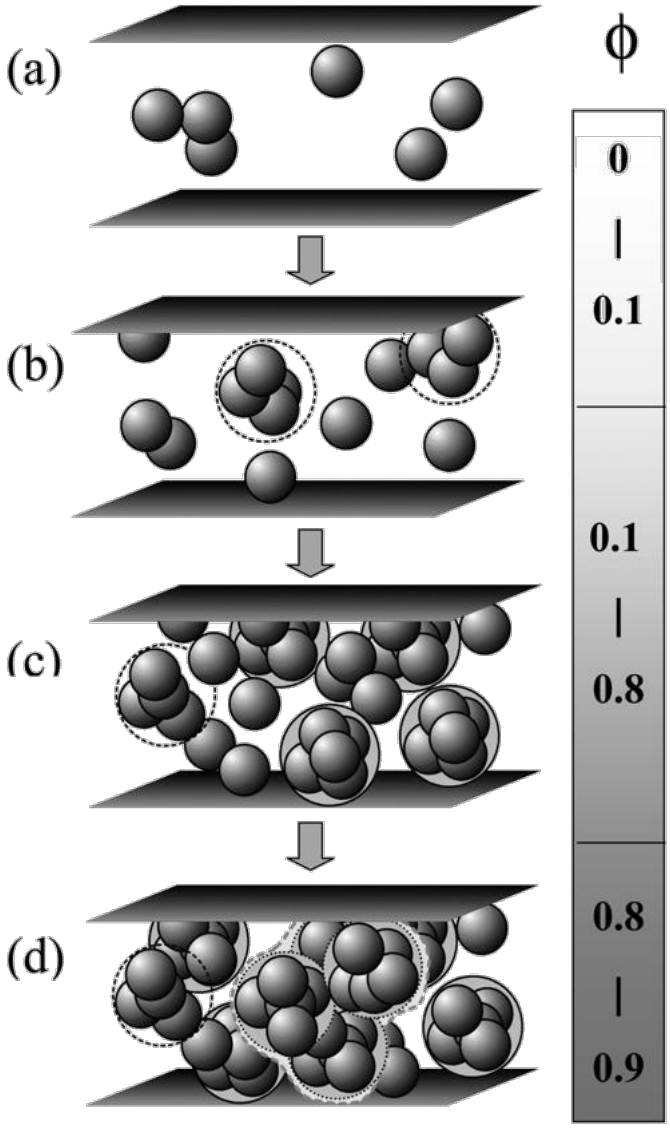

Figure 4.6 Mechanism of water adsorption: (a) association of water molecules, (b) cluster formation, (c) enhancement of interaction between clusters and walls, and (d) formation of highly ordered structures.(*72*)

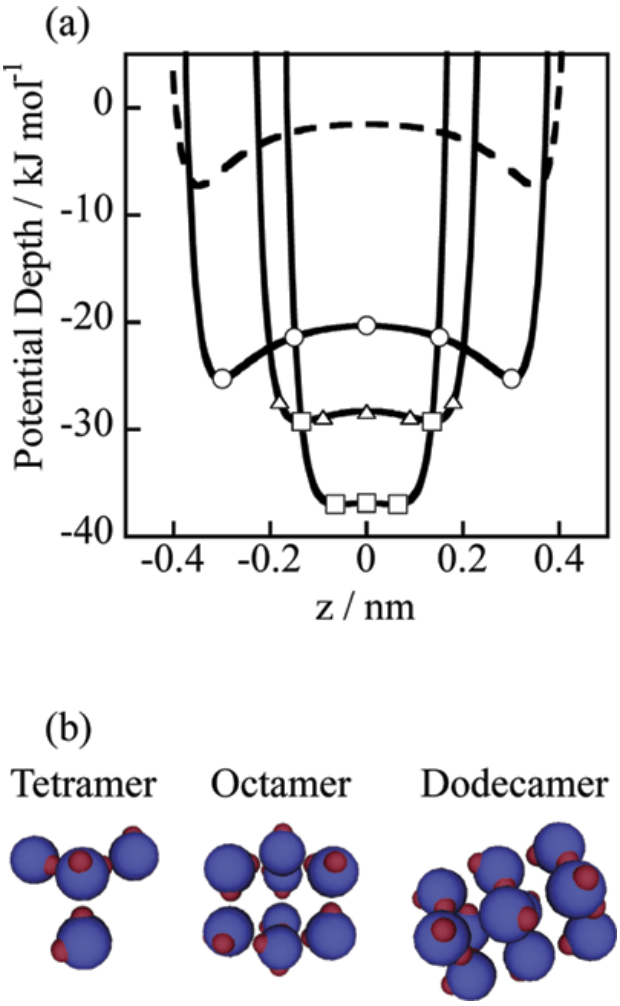

Figure 4.7 Interaction profiles of a water molecular cluster with the graphitic slit nanopore: (circle) tetramer, (triangle) octamer, and (square) dodecamer. The dashed curve denotes the potential profile for a single water molecule (a). Here, the structures of the model clusters are shown in (b).(*74*)

4.1.4 Water Adsorption in Micropores of Activated Carbon Revealed by NMR

The structural characteristics of water clusters have been observed in simulation studies. However, direct experimental validations of these proposed mechanisms are scarce. Although various analytical methods such as XPS,(*83*) AFM,(*84*) STM,(*85*) *etc.* have been applied to study this phenomenon, these techniques are not suitable for studying adsorbed water inside complex porous networks due to the difficulty of accessing the inside of pores. NMR is one of

the few experimental techniques that could look into the inside of nano-sized pores with the ability of acquiring structural and dynamic information of nanoconfined fluids.(*20, 86-88*) There is another very important NMR capability that has not been explored in studying nanoconfined liquids in carbon micropores, namely, the NMR imaging capability with sub-nanometer scale spatial resolution. Such imaging capability is obviously not based on applying an external magnetic field gradient as in conventional magnetic resonance imaging (MRI) but is based on a field gradient generated by graphitic-like carbon surface. Such internal field gradient is extremely strong in close proximity (nanometer scale) to the carbon surface, giving rise to a substantial nucleus independent chemical shift (NICS); the NICS depends sensitively on the distance between the nuclear spin and the carbon surface.(*34*)

The NICS-based sub-nanometer scale spatial resolution provides NMR with a unique imaging capability in studying physical and chemical processes near the surface. In this chapter, we use this approach to reveal the water adsorption process in activated carbon micropores. Combining the information on thermodynamics obtained from in situ NMR-detected water isotherm and spatially resolved information on structure and dynamics obtained by NICS-resolved NMR, the microscopic process of water nucleation and growth inside the micropores of activated carbons is investigated. The formation of water clusters at surface sites, the cooperative growth process of pore bridging, and the final stage of horizontal pore filling are revealed in detail, demonstrating the potential of this comprehensive NMR approach for studying microscopic mechanisms at solid/liquid interfaces including electrochemical processes.

4.2 Experimental Details

4.2.1 Synthesis of Microporous Activated Carbon

The sample studied is an activated carbon derived from the high-temperature polymer, polyetheretherketone (PEEK).(*89*) As shown in Figure 4.8, the sample preparation process consists of two steps: carbonization and activation. During carbonization, 2 g of granulated Victrex PEEK is heated in an argon gas tube at 900 ℃ for 30 min, yielding the carbonized product. Then, the product is cooled down to room temperature in an argon environment, and grounded into smaller particles. During the activation, water steam is introduced to enlarge the micropores created during carbonization. The grounded sample is then again heated at 900 ℃ under the water steam, carried by the Ar gas flow, for a certain time period. Different activation times lead to different mass loss amounts and micropore sizes. In this study, the sample (labeled as PEEK-90) is heated until 90% of the mass is lost; this mass loss refers to the ratio between the sample mass after activation and that before activation but after carbonization.

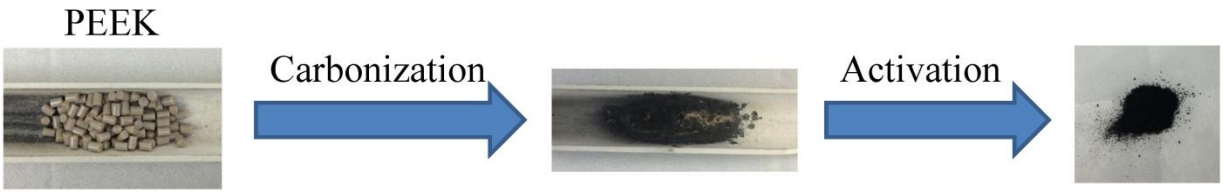

Figure 4.8 Sample preparation process of microporous activated carbon.

4.2.2 NMR Experiments

All ^{1}H magic-angle spinning (MAS) NMR spectra are obtained at 400 MHz, under MAS spinning speed of 8 kHz, and at room temperature (T = 296 K). Before NMR measurement, 15 mg of PEEK-90 sample is loaded into a 4 mm MAS NMR rotor and dried at 90 ℃ in vacuum for 24 h to remove preadsorbed water. Then, a background ^{1}H NMR spectrum of the vacuum-treated PEEK-90 is first recorded, showing a weak, broad peak of 40 ppm (full width at half-maximum,

FWHM) which is then subtracted from all presented spectra. Varying amounts of water vapor are added by placing the sample in a saturated water vapor system at 296 K for proportional durations. The amount of water loaded is determined by finding the mass difference between the vapor-loaded sample and the initial, dry sample. A single-pulse excitation with a pulse duration of 5 μs and a 5 s relaxation delay is applied. The longitudinal relaxation time (T_1) is measured by the standard inversion-recovery method (pulse sequence 180°- τ -90°).

4.2.3 *in-situ* NMR-based Isotherm Measurement

An *in-situ* NMR-based method is used to measure the water isotherm of the PEEK-90 sample. Detailed descriptions of the instrument can be found in Chong *et al*.(*90*) The water adsorption isotherm at 296 K is measured at ^{1}H frequency of 34.3 MHz. The ^{1}H free-induction-decay (FID) signal of the dry sample is firstly acquired by a single-pulse excitation with a pulse duration of 8 μs. A broad peak of 750 ppm (FWHM) is observed in the background spectrum and is subtracted from subsequent spectra. Water vapor is then loaded to the sample at varying vapor pressures and the NMR spectra of the hydrated samples are acquired. The loaded water mass is determined as follows: total water mass at saturation is found by direct weighing; then, the pre-saturation masses are determined by comparing the corresponding peak intensities to the saturation peak intensity. The adsorption isotherm is obtained by plotting the water-carbon mass ratio as a function of relative vapor pressure.

4.3 Results and Discussion

4.3.1 Nucleus-Independent Chemical Shift (NICS)

As discussed in Section 3.4, NICS originates from delocalized π electron orbitals in graphitic-like carbon surface giving rise to a diamagnetic response, reducing the local magnetic field at the nucleus near the graphitic carbon surface. Density functional theory (DFT)

calculations show that the NICS value of a nucleus increases rapidly as the distance of the nucleus and the carbon surface decreases, especially within the range of a nanometer.(*34*) The NICS value δ_{NICS} can be expressed as a function of the distance *r* between the probe atom and the carbon surface (atomic center to center):

$$\delta_{\mathrm{NICS}}(r) = Aexp\left[-\left(\frac{r}{r_0}\right)^{\beta}\right] + Aexp\left[-\left(\frac{d-r}{r_0}\right)^{\beta}\right], \quad (4.1)$$

with the parameters A = -24.5 ppm, r_0 = 0.227 nm, β = 0.754; d is the width of the slit-shaped pore (atomic center to center).(*34*) For a single nucleus inside a slit-shaped pore of 1.9 nm in width (atomic center to center), as illustrated in Figure 4.9, the δ_{NICS} of the nucleus is -5.7 ppm if it is 0.4 nm away from the surface (from the carbon atom center to the probing nucleus), while at a distance of 0.7 nm, δ_{NICS} = -3.0 ppm (δ_{NICS} = 0 ppm for nucleus outside the pore). Thus, several angstroms difference in position can cause a significant difference in δ_{NICS}, enabling NMR to evaluate the distance of the nucleus from the surface. For a molecular cluster that is liquid-like, motional averaging has to be considered in calculating the measured average δ_{NICS}. For example, as shown in Figure 4.9, a group of molecules form a cluster in which molecules move rapidly on the NMR timescale (around 10 ms) within the cluster. The measured δ_{NICS} is then the average of the δ_{NICS} values of all nuclear spins within the cluster. Additionally, it is worth noting that the measured δ_{NICS} cannot average over water in different micropores. On the NMR timescale and even over longer durations (20 ms), the ^{1}H NMR 2D exchange experiment shows there is no exchange between water in different micropores, and also no exchange between water in micropores and water in larger mesopores and in intergranular space.(*88*)

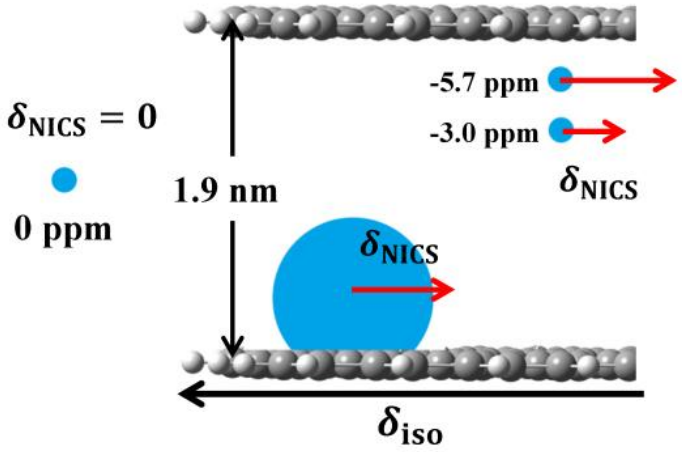

Figure 4.9 Illustration of molecules inside a slit-shaped pore of width 1.9 nm (carbon atom center to center). The grey spheres are carbon atoms and the blue spheres represent water clusters.

4.3.2 Pore Size Determination

Figure 4.10 shows the ^{1}H MAS NMR spectrum of PEEK-90 activated carbon sample fully filled with water (θ = 2.38). The left peak set at 0 ppm is due to water in the intergranular space (sharp peak) and large mesopores (broad shoulder); the right peak at -3.9 ppm is due to water inside micropores. The pore size distribution of PEEK-90 is obtained by NMR NICS analysis and is shown in the inset of Figure 4.10. Based on this analysis the average pore size (carbon atom center to center) of the PEEK-90 activated carbon sample is 1.90 nm. More importantly, the FWHM of the distribution is only 0.20 nm, showing that the pore size of the PEEK-90 activated carbon sample is rather uniform.

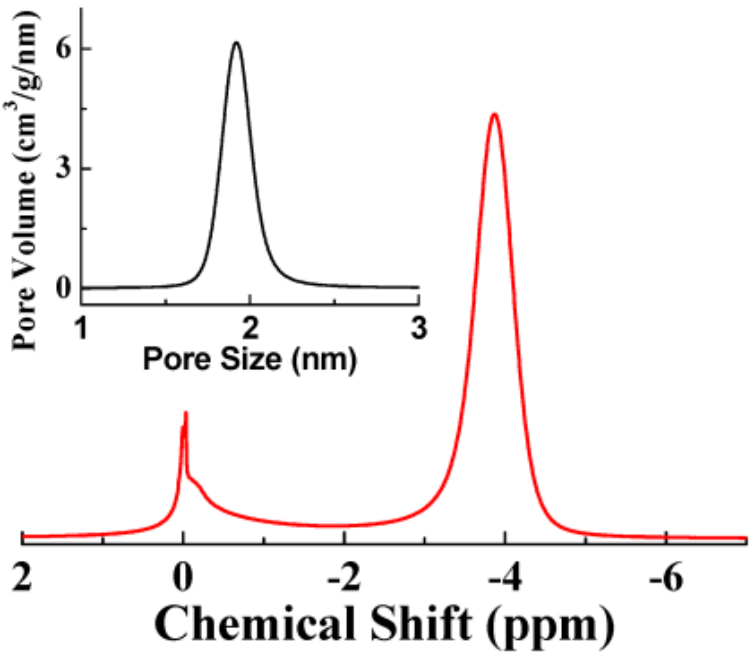

Figure 4.10 ^{1}H MAS NMR spectra of water in the PEEK-90 activated carbon sample. The chemical shift of the free water outside the pore (left peak) is set to 0 ppm. The inset is the pore size distribution of PEEK-90.

4.3.3 Water Adsorption Isotherm in Activated Carbon at 296 K

The water adsorption isotherm at 296 K is measured at ^{1}H frequency of 34.3 MHz equipped with an in situ water loading system under controlled relative water vapor pressure P/P_0. As shown in Figure 4.11, the adsorption isotherm of water in PEEK-90 is a typical Type V curve according to the IUPAC classification.(*54*) The isotherm is divided into four regions according to the information provided by the NICS-resolved NMR, which will be discussed below.

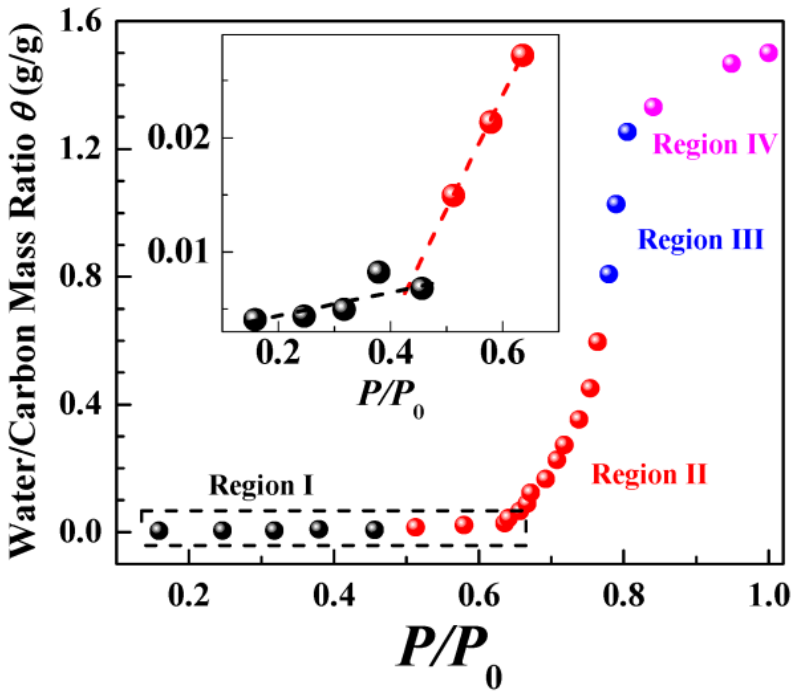

Figure 4.11 NMR-detected adsorption isotherm of water in PEEK-90. The curve is divided into four regions according to the water-carbon mass ratio θ. Black: $\theta < 0.01$, region I; red: $0.01 < \theta < 0.60$, region II; blue: $0.60 < \theta < 1.25$, region III; purple: $1.25 < \theta < 1.50$, region IV. The region in the dashed box is magnified in the inset of (c) showing the onset of cooperative adsorption at water relative pressure of $P/P_0 = 0.5$ ($\theta = 0.01$).

4.3.4 Structural Understanding of Water Adsorption on PEEK-90 Activated Carbon

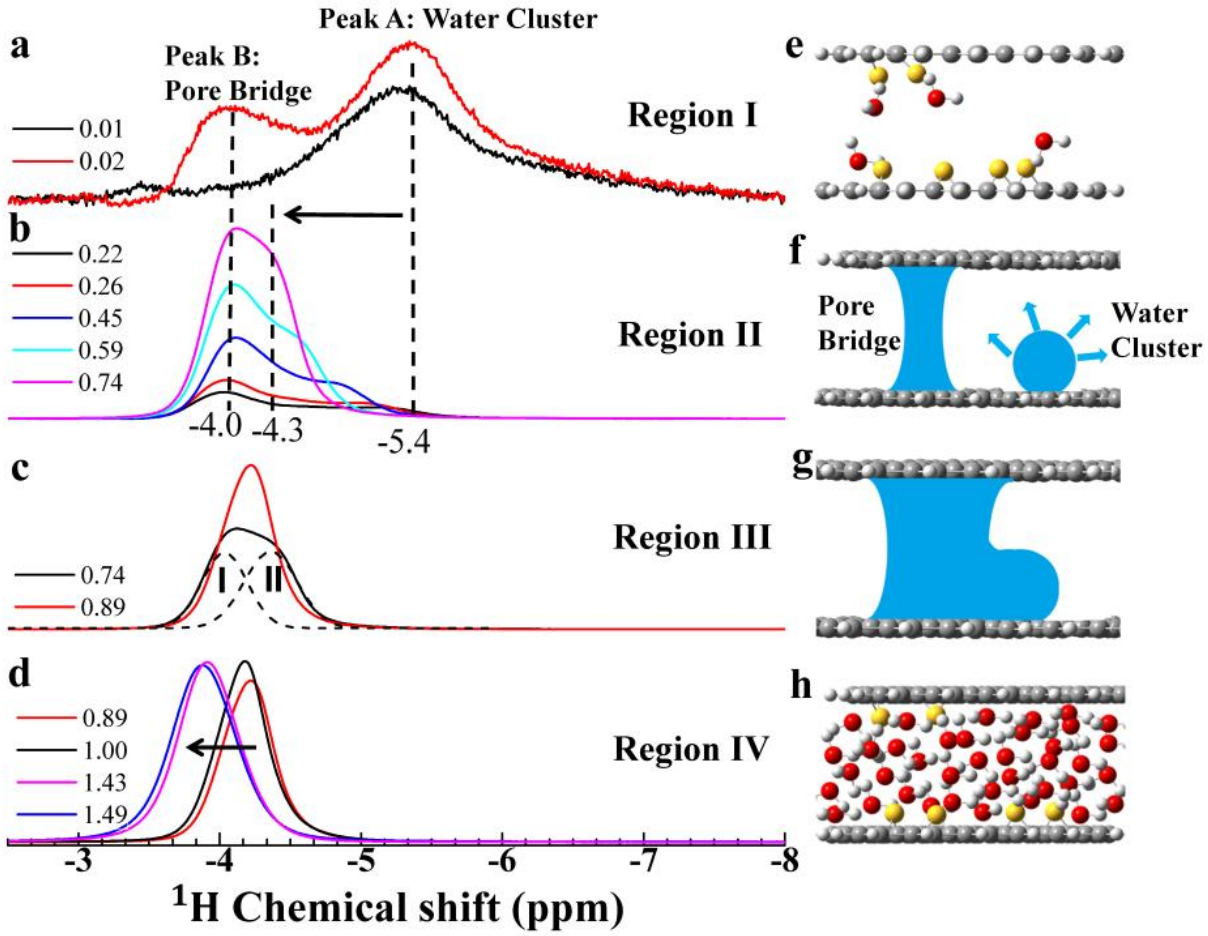

Figure 4.12 (a-d) ^{1}H MAS NMR spectra of water adsorbed in PEEK-90 activated carbon at different θ, ranging from 0 to 1.49. Varying amounts of water are added by placing the sample in a saturated water vapor system at room temperature for different durations; greater adsorption levels require longer durations in the water vapor system. (e-h) Schematic diagrams of water adsorption structures in activated carbon at different filling levels. The grey spheres are carbon atoms, the yellow spheres represent surface adsorption sites, the red spheres represent O, and the white spheres represent H.

Figure 4.12a shows the ^{1}H MAS NMR spectra for the two lowest water filling levels. At the water-carbon mass ratio θ = 0.01, the spectrum (black curve) consists only of a single broad peak, labeled as peak A. The NICS of peak A is -5.4 ppm, and is the most negative among all

spectra studied. As discussed above, the measured chemical shift is the average of the δ_{NICS} values of all protons within the water cluster. A simple model is applied to correlate the measured δ_{NICS} with the height of adsorbed water cluster. Here, it is assumed that the density spatial distribution (ρ) of water molecules throughout the water cluster is uniform, that is, the number of water molecules inside the cluster at each height is identical. For a slit-shaped pore of width 1.9 nm (PEEK-90), the averaged δ_{NICS}, δ_{avg}, of such adsorbed water cluster can be calculated as

$$\delta_{\mathrm{avg}} = \frac{\int_{0.32}^{h+0.17} \rho(r)\delta(r)dr}{\int_{0.32}^{h+0.17} \rho(r)dr}, \tag{4.2}$$

where *h* is the height of adsorbed water cluster, 0.17 nm is the radius of a carbon atom, 0.32 nm is the closest distance between a hydrogen atom and the carbon atom, *r* is the distance between the hydrogen atom center and the graphitic-like carbon surface (atomic center to center), and $\rho(r)$ is the density spatial distribution of the water cluster (assumed to be constant in this model).(*91*) Since the δ_{avg} of peak A equals to -5.4 ppm, the height *h* of adsorbed water cluster for peak A is 0.35 nm, which is in good agreement with the height of a monolayer water (0.37 nm).(*84*) Therefore, it can be concluded that water molecules associated with peak A are, on average, directly adsorbed on the carbon surface. Since water molecules do not have affinity to the hydrophobic carbon surface, they tend to nucleate at hydrophilic defect sites, usually oxygen-containing functional groups, via hydrogen bonding.(*92*) The broad ^{1}H NMR spectrum of peak A is a result of both the restricted mobility of the water molecules and the differences in chemical environments of water at defect sites. Such a surface site nucleation process is depicted in Figure 4.12e. Moreover, comparing to the isotherm (Figure 4.11) at $\theta < 0.01$, this spectrum corresponds to the initial adsorption region I of the isotherm ($P/P_0 < 0.5$ and $\theta < 0.01$, black dots). The amount of adsorbed water in region I is very small indicating that the density of surface

adsorption sites in the PEEK-90 sample is very low. There are very few surface sites for water to nucleate.(*93*)

When θ is increased slightly to 0.02 (red curve in Figure 4.12a), corresponding to the adsorption region II in the isotherm, two well-resolved peaks are clearly observed. One peak is broad and located at -5.4 ppm, having the same shift and shape as peak A for θ = 0.01, indicating a similar water cluster size. The other peak (peak B) is narrower and is located at -4.0 ppm. Peak B has a less negative δ_{avg} than peak A, indicating that the average distance of water molecules associated with peak B is larger than that of peak A. Upon further increase of θ up to 0.74 (Figure 4.12b), spectra continue to show two well-resolved peaks. However, these two peaks vary markedly differently with increasing θ. Peak B does not shift, staying constant at about -4.0 ppm, while peak A gradually shifts, from -5.4 ppm to -4.3 ppm. To analyze peak B, two distinct features of the spectrum are considered. First, the δ_{avg} of peak B is always at -4.0 ppm as the amount of adsorbed water increases. Second, the δ_{avg} of peak B (-4.0 ppm) is very close to the δ_{avg} of fully filled sample which is at -3.9 ppm. This indicates that the average distance of water clusters associated with peak B does not change with increasing θ. This suggests that water molecules associated with peak B form bridges across the opposing pore walls, spanning the height of the micropore (Figure 4.12f). The formation of pore bridges is a more cooperative process compared to nucleation at surface sites. The onset of cooperative bridging depends on the local density of surface defect sites, as suggested by previous simulation results.(*66, 68, 94*) In regions with denser defect sites, the opportunity for cooperative adsorption is high; a few water molecules could form more hydrogen bonds with neighboring adsorbed water molecules, by forming bridges across the pores. This cooperative adsorption process is energetically favorable, leading to a significantly enhanced adsorption with small changes in the relative water

vapor pressure P/P_0. While the shift of peak B stays constant, peak A gradually shifts to the left as θ increases, signifying that on average, water molecules are moving farther away from the carbon surface. Since, as mentioned above, peak A corresponds to water clusters adsorbed on the surface adsorption sites, the shift of peak A must be a result of the growth of water clusters at these sites. Eventually, the clusters grow large enough such that the NICS of peak A approaches that of peak B. Different from peak B, water molecules associated with peak A are in regions with sparse surface sites; they have less chance to bridging across the pores and their sizes grow gradually with a gradually shifting NICS rather than jumping immediately to -4.0 ppm. As illustrated in Figure 4.12f, water adsorption at this intermediate filling stage is controlled by two parallel processes: the cluster growth and the cooperative pore bridging. Comparing to the isotherm in Figure 4.11, this stage corresponds to the region II of $0.5 < P/P_0 < 0.75$ and $0.01 < \theta < 0.60$ (red dots). In the inset of Figure 4.11, the amount of adsorbed water in region II increases much faster than in region I. Thus, cooperativity of pore bridging plays an important role in the adsorption process.

When θ is increased to 0.89 (Figure 4.12c), the ^{1}H MAS NMR spectra are again dominated by a single peak. Comparing the spectra of $\theta = 0.89$ and $\theta = 0.74$ in Figure 4.12c, it is evident that the peak center of $\theta = 0.89$ is located in between the peak centers of the $\theta = 0.74$ spectrum. The disappearance of the two peaks is due to the coalescence of pore bridges and water clusters. At earlier stages, pore bridges and water clusters are spatially separated and unconnected, which is supported by the lack of exchange in the 2D exchange NMR shown in Figure 4.13. Figure 4.13 shows the ^{1}H 2D-EXSY NMR spectra of water absorbed in the PEEK-90 sample at $\theta = 0.12$ with different mixing times. Cross peaks are observed neither for long (50ms), nor for short (5 ms) mixing times, indicating that pore bridges and water clusters are

spatially separated and unconnected. Thus, the NMR spectra display two different peaks: one for the bridges and the other for the clusters. However, when the pore bridges and water clusters become connected with additional water adsorption, the peaks from distinct chemical environments finally merge and the NMR spectra display a single peak. As illustrated in Figure 4.12g, the newly adsorbed water fills empty space between water clusters and pore bridges, connecting clusters and bridges. This interpretation is supported by the following estimation. The spectrum of $\theta = 0.74$ can be fitted by two individual Gaussian peaks, peak I and peak II (dashed lines in Figure 4.12c). Peaks I and II represent pore bridges and water clusters, respectively. The peak centers of peak I and peak II are -4.03 and -4.36 ppm, respectively. Assuming a symmetric exchange between the two peaks, the peak center of the exchange spectrum is equal to -4.19 ppm. This value is in very good agreement with the experimentally observed chemical shift of -4.2 ppm when $\theta = 0.89$. Comparing to the isotherm, this stage corresponds to the region III of $0.75 < P/P_0 < 0.80$ and $0.80 < \theta < 1.25$ (blue dots). The amount of adsorbed water in region III increases even steeper than in region II. In this stage, the adsorption is mainly controlled by the coalescence of water clusters and pore bridges.

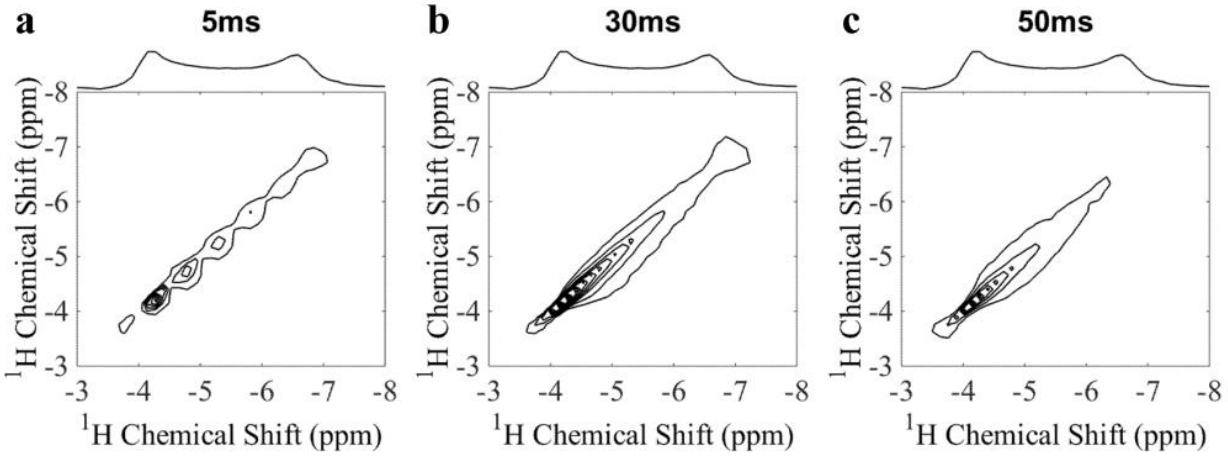

Figure 4.13 ^{1}H 2D-EXSY MAS NMR spectra of water absorbed in the PEEK-90 sample at θ = 0.12 with different mixing times.

In Figure 4.12d, the single peak gradually shifts to the left upon further adsorption because water starts to fill some remaining empty space, inducing horizontal pore filling along the pores (see Figure 4.12h). As θ reaches 1.49, no more water can be absorbed, indicating that the micropores in PEEK-90 have been fully filled by water. Comparing to the isotherm, this stage corresponds to the region IV of $0.80 < P/P_0 \leq 1$ and $1.25 < \theta < 1.50$ (purple dots). The amount of adsorbed water in region IV is small because most of the pores have been filled already.

4.3.5 Dynamics of Adsorbed Water Molecules in PEEK-90 Activated Carbon

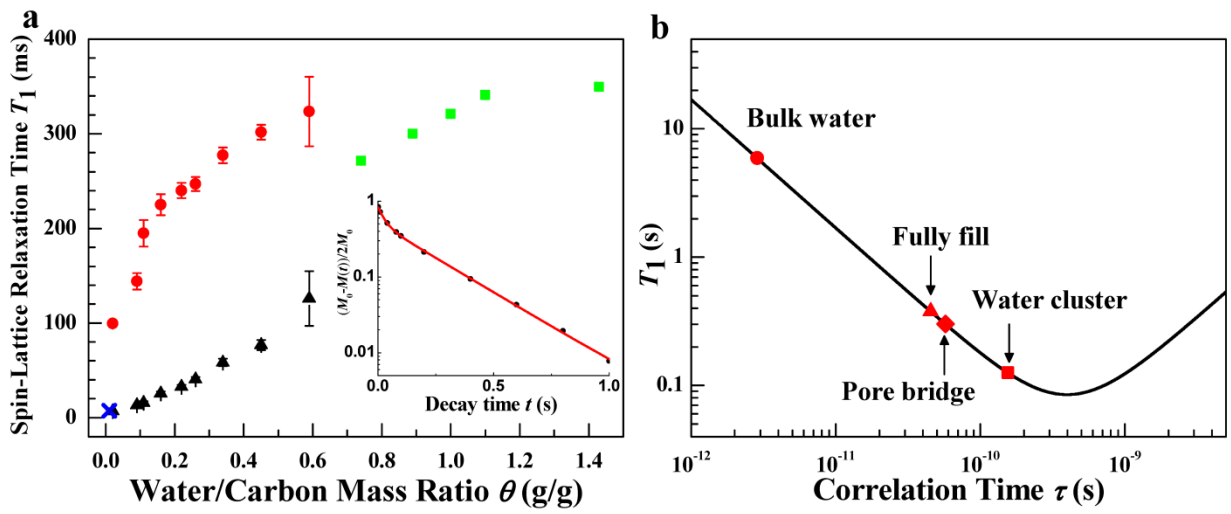

Figure 4.14 (a) The ^{1}H spin-lattice relaxation time (T_1) of adsorbed water at different stages of water adsorption. Blue cross: θ = 0.01, region I; black triangles: surface clusters; red spheres: pore bridges; green squares: single peak region with nearly filled pores, region III and IV. The standard deviations of the T_1 fitting are given by the error bars. The inset is the ^{1}H magnetization decay curve at θ = 0.16. The solid line is a fit using the double-exponential function. (b) The theoretical value of T_1 based on intramolecular dipolar interaction. The correlation times of bulk water, water in the fully filled PEEK-90 sample, pore bridge and water cluster at θ = 0.59 are 3.5, 49, 53 and 154 ps, respectively.

The dynamics of adsorbed water molecules is investigated by measuring the ^{1}H spin-lattice relaxation times (T_1) via the standard inversion-recovery method. Assuming that the ^{1}H T_1 relaxation process in water is dominated by the fluctuations of intramolecular proton-proton dipolar interaction, T_1 is given by

$$\left(\frac{1}{T_1}\right) = \frac{3\mu_0^2\gamma^4\hbar^2}{160\pi^2 r^6}\left(\frac{\tau}{1+\omega_0^2\tau^2} + \frac{4\tau}{1+4\omega_0^2\tau^2}\right), \tag{4.3}$$

where γ is the gyromagnetic ratio of proton, $2\pi\hbar$ is the Planck constant, r = 0.156 nm is the distance between the two protons in a water molecule, μ_0 is the magnetic permeability of free space, τ is the rotational correlation time, and $\omega_0/2\pi$ is the Larmor frequency (400 MHz).(*95*) The rotational correlation time τ is estimated by the average time taken for the molecule to rotate by 1 rad.(*96*) Small τ corresponds to fast molecular motion, while large τ corresponds to slow molecular motion.

Figure 4.14 shows the ^{1}H T_1 of confined water in different stages of water adsorption. In the surface site nucleation stage (θ = 0.01, region I), the decay curve can be fitted very well with a single exponential decay $M(t)/M_0 = 1 - 2\exp(-t/T_1)$, where M is the magnetization of ^{1}H nuclei and M_0 is the equilibrium magnetization. A very short T_1 of 8 ms is observed (blue cross in Figure 4.14a). This T_1 is significantly shorter than the value of bulk water (several seconds), and also shorter than the value of water in fully filled micropores (several hundred milliseconds). Such a short T_1 value is caused by the slowdown of water molecular motion. At the beginning, few water molecules nucleate on surface sites, forming water clusters which are quite different from bulk-water-like network. In these surface-nucleation water clusters, the molecular motions, such as rotation and translation, are highly restricted by surface sites, making the rate of molecular motion slowing down and causes effective spin-lattice relaxation with short T_1.(*95*)

In the cooperative filling stage (region II), two different T_1 values are observed. Specifically, the T_1 value of the water clusters increases from 10 ms to 110 ms. In the meanwhile, the T_1 value of the pore bridges increases from 100 ms to 330 ms. The inset in Figure 4.14a shows a typical ^{1}H magnetization decay curve in region II (θ = 0.16). It clearly shows two components of exponential decays and can be fitted very well with a double-exponential function (red solid line). Finally, in the final stage (region III and IV) where the two peaks merge together, there is only a single T_1 reaching a plateau around 350 ms, which is the typical T_1 value for water of filled micropores. Similar T_1 behaviors have been reported by Wang(*93*) and Khozina(*97*).

In contrast to the surface site nucleation stage, both water clusters and pore bridges in the cooperative and final filling stage contain more water molecules with more developed hydrogen network. Therefore, Equation 4.3 is applied to estimate the corresponding correlation times based on the measured T_1. Figure 4.14b plots the theoretical values of T_1 versus τ. According to the adsorption model, the pore bridging region is similar to the fully filled micropore, predicting that the correlation times of these two structures should be similar. Moreover, due to the less developed hydrogen network, the motion of water molecules in water cluster is slower than in pore bridges. Thus, the correlation time τ of water clusters should be longer than that of pore bridges. Both predictions are confirmed by the experimental results. As shown in Figure 4.14b, the τ of fully filled sample (θ = 1.49) is 49 ps, very similar to the τ = 53 ps of pore bridges. The τ of water clusters is 154 ps, which, as expected, is much longer than that of pore bridges.

4.4 Summary and Outlook

In conclusion, this study showcases the unique power of NICS-based NMR to probe the intricacies of confined fluid-solid interactions on the nanometer scale. While previous research

had focused on isotherms, which only provide information on the amount of adsorption, the present measurement directly images how the water clusters nucleate and grow during the adsorption process. This study provides direct experimental evidence of the detailed nucleation and growth processes of water inside activated carbon micropores. It is shown that water adsorption starts with nucleation at surface sites. This is followed by two growth processes. One is the gradual growth of water clusters and the other is the cooperative growth by pore-bridging. These two processes both contribute to the water adsorption associated with the sharp increase in the water isotherm. Finally, these two distinct water structures coalesce together, leading to the pore filling along the pores at the final stage. Future studies can make use of this NICS-based NMR method to study molecular and ionic processes nanoconfined by graphitic-like carbon surfaces.

CHAPTER 5 EXPLORING THE ADSORPTION-DESORPTION HYSTERESIS OF WATER ON NANOPOROUS CARBON USING NMR

5.1 Context and Scope

Porous materials such as zeolites, carbons, metal-organic frameworks (MOF), covalent organic framework (COF), clays, and silicates have a large spectrum of applications, including but not limited to, separation, purification, catalysis, adsorption, and energy conversion and storage.(*98-103*) Moreover, the use of porous solids is expected to grow in the future; for example, in energy-efficient devices for harvesting water from desert air and in controlled drug/cargo delivery and cancer therapy.(*104, 105*) An important feature of porous materials is the phenomenon of hysteresis: for a certain range of applied pressures, the adsorption and desorption curves do not coincide; typically, in the hysteresis range, the amount adsorbed by the porous host is higher during desorption than adsorption. Although this phenomenon has been known for over a century, the underlying structure and dynamics responsible for the hysteresis remain poorly understood. This defines the goal of this chapter: to correlate the macroscopic sorption isotherm with the microscopic molecular organizations and dynamics of adsorbates, and thus understand the adsorption hysteresis on porous materials.

Section 5.1 gives an overview of the adsorption hysteresis phenomenon, focuses on the classification and origin of hysteresis loops. In Section 5.2 and 5.3, we present a combined experimental study in which microscopic and macroscopic aspects of water adsorbed by the microporous carbon associated with hysteresis are quantified by direct measurement.

5.1.1 Classification of Hysteresis Loops

An empirical classification of hysteresis loops is given by an International Union of Pure and Applied Chemistry (IUPAC) report as shown in Figure 5.1.

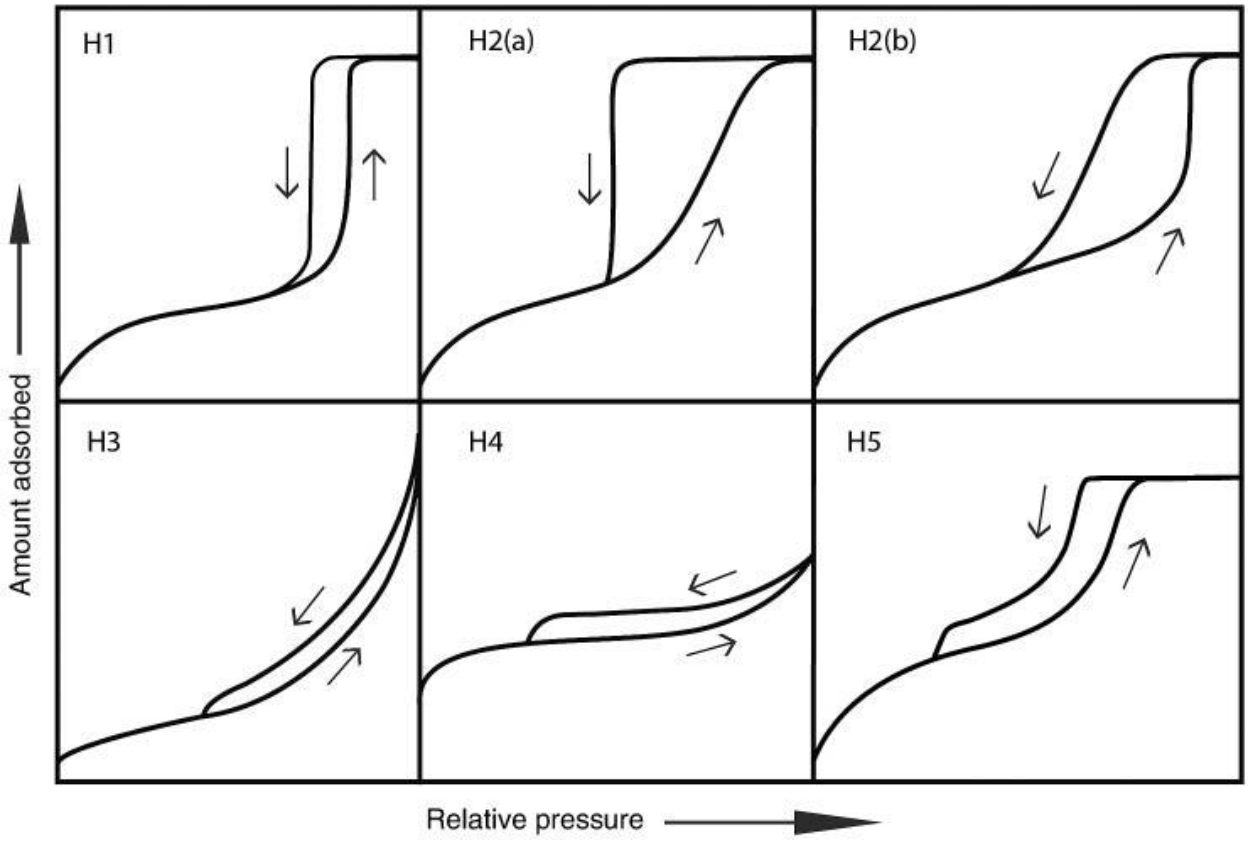

Figure 5.1 Classification of hysteresis loops.(*56*)

According to the IUPAC classification, Type H1 is often associated with ordered mesoporous materials which exhibit a narrow range of uniform mesopores, such as template silicas (e.g., MCM-41, MCM-48, SBA-15) and ordered mesoporous carbons. Type H2 is often given by disordered pore systems, in which network effects are important. In Type H2(a), the desorption branch of the hysteresis loop is significantly steeper than the adsorption branch. This can be attributed to pore-blocking/percolation in a narrow range of pore necks or to cavitation-induced evaporation. A distinctive feature of isotherms revealing Type H3 and H4 hysteresis is

that the adsorbate uptake does not exhibit any limiting amount at high P/P_0. Such a high adsorption capacity can be given by non-rigid aggregates of plate-like particles (e.g., certain clays), but also in the pore network consisting of macropores which are not completely filled with pore condensate. Type H5 hysteresis also contains the steep step down, but it has a distinctive form associated with certain pore structures containing both open and partially blocked mesopores (e.g., plugged hexagonal templated silicas). Thus, Type H5 has two distinct steps in the desorption branch. Examples of selected hysteresis loops types discussed above are shown in Figure 5.2.

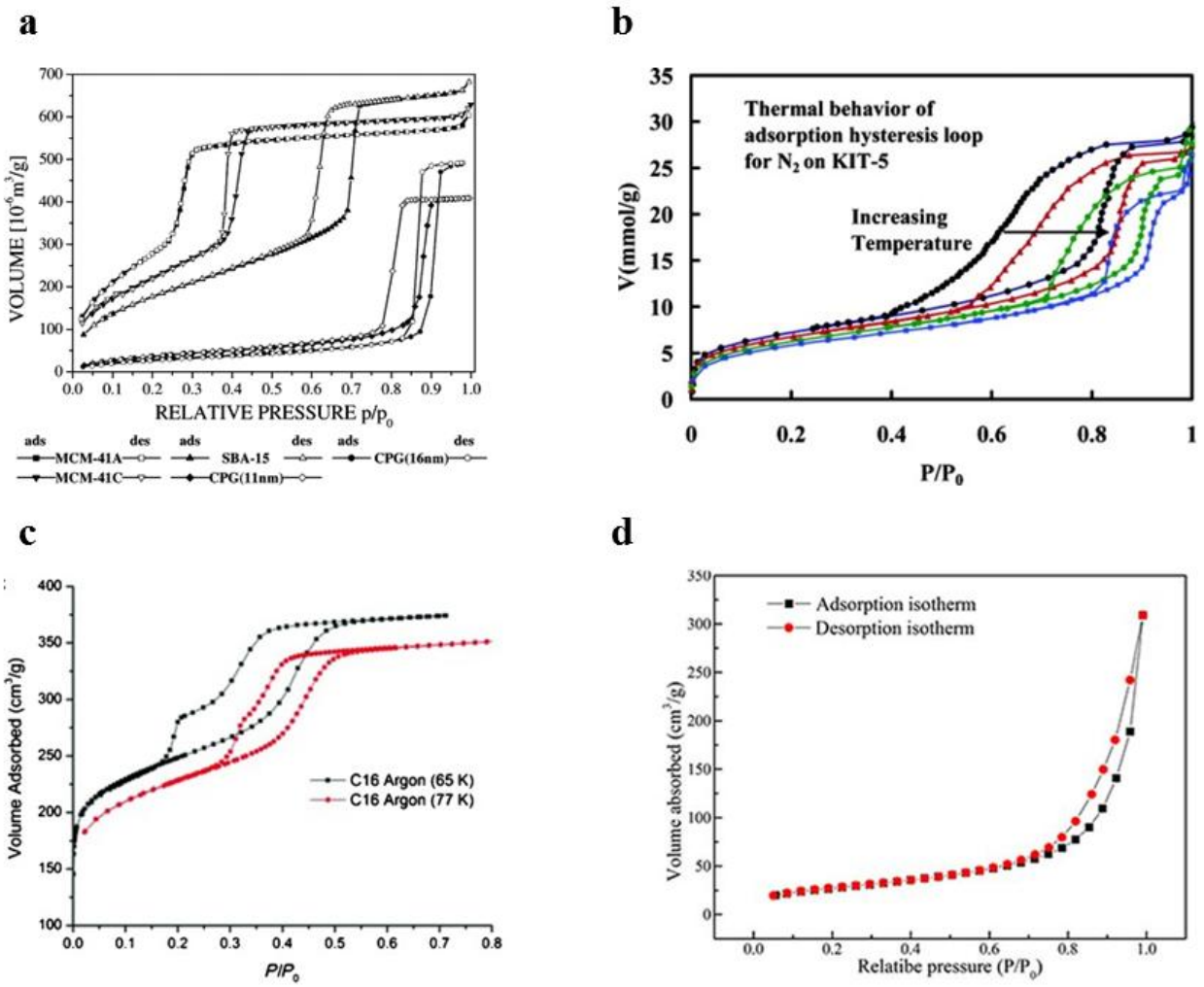

Figure 5.2 Examples of selected hysteresis loops types discussed in Figure 5.1. (a): Type H1, Argon sorption isotherms at 87 K in MCM-41, SBA-15 and CPG.(*106*) (b): Type H2, thermal behavior of adsorption hysteresis loop for N_2 on KIT-5.(*107*) (c): Type H5, Argon adsorption isotherms at 77 K and 65 K on zeolite Y.(*108*) (d): Type H3, N_2 adsorption-desorption isotherms on cellulose nanofibril/graphene oxide hybrid aerogel.(*109*)

5.1.2 Origin of Hysteresis

Although the adsorption hysteresis has been known for over a century, the origin of sorption hysteresis is still a matter of discussion. There are essentially two models that contribute to the understanding of sorption hysteresis: independent pore model and network model.

5.1.2.1 Independent Pore Model

According to the *independent pore model*, adsorption hysteresis is considered as an intrinsic property of the vapor-liquid phase transition in a single pore. That is, the desorption process is associated with the vapor-liquid transition, whereas hysteresis is caused by the fact that condensation (adsorption) is delayed due to the existence of metastable adsorption films and hindered nucleation of liquid bridges. The hysteresis loop expected for this case is of Type H1.

This idea has been confirmed by theoretical studies based on non-local density functional theory (NLDFT) and Monte Carlo simulation. For example, Alexander V. Neimark and coworkers applied Monte Carlo and NLDFT to study the sorption of N_2 in mesoporous siliceous molecular sieves of MCM-41.(*110*) Figure 5.3 compares the NLDFT and Monte Carlo simulation isotherms with the corresponding experimental sorption isotherm of N_2 on four MCM-41-like samples at 77.4 K. Both adsorption and desorption isotherms are in quantitative agreement with the theoretical predictions, in which the pores of MCM-41 are modeled as infinitely long cylindrical channels. Moreover, summarized in Figure 5.4, the molecular level theoretical models reveal that the desorption branch follows the theoretical prediction of equilibrium transitions; whereas the adsorption branch (pore condensation) is delayed due to the metastability associated with the nucleation of liquid bridges and thus resulting in hysteresis.

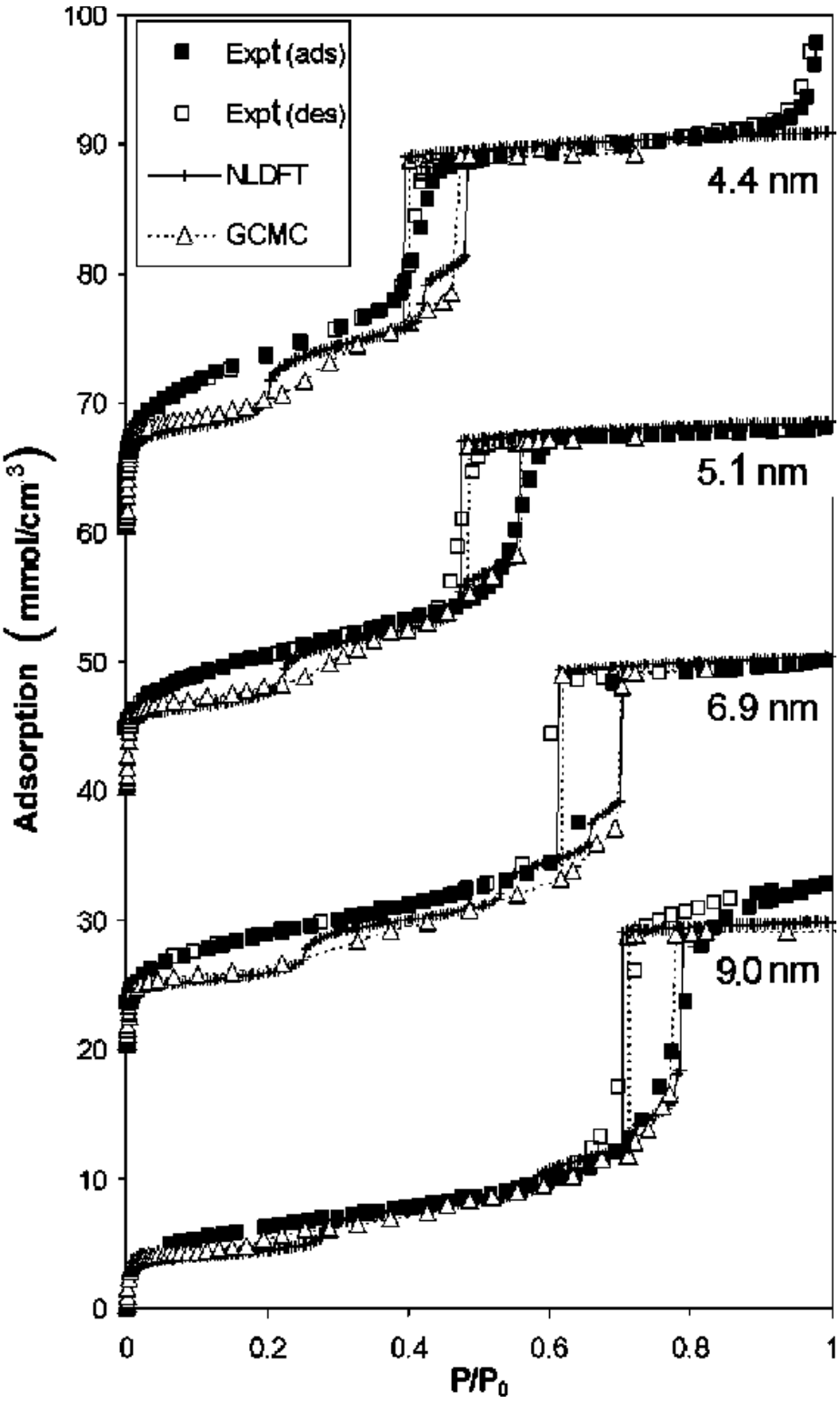

Figure 5.3 Isotherms of nitrogen adsorption on several MCM-41-like samples at 77.4 K. Pore widths are shown on the plot.(*110*)

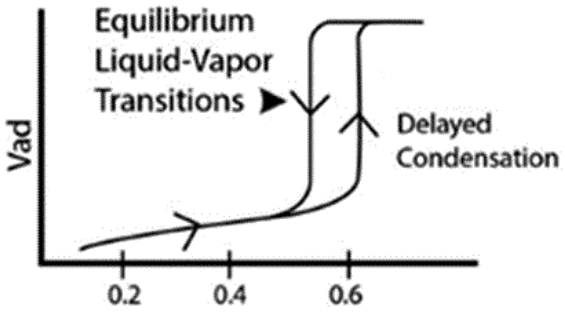

Figure 5.4 According to the *independent pore model*, the desorption process is associated with the vapor-liquid transition, whereas the adsorption (pore condensation) is delayed due to the existence of metastable adsorption films and hindered nucleation of liquid bridges.(*101*)

5.1.2.2 Network Model

According to the *network model*, adsorption hysteresis is a consequence of the pore blocking and cavitation effect in a three-dimensional network.(see Figure 5.5) For example in ink-bottle shape pores, pore evaporation is delayed because the wide body of the pore cannot evaporate until the narrow neck of the pore first empties. Thus, in a network of ink-bottle pores, the desorption branch does not occur at thermodynamic equilibrium, but reflects a percolation transition instead.

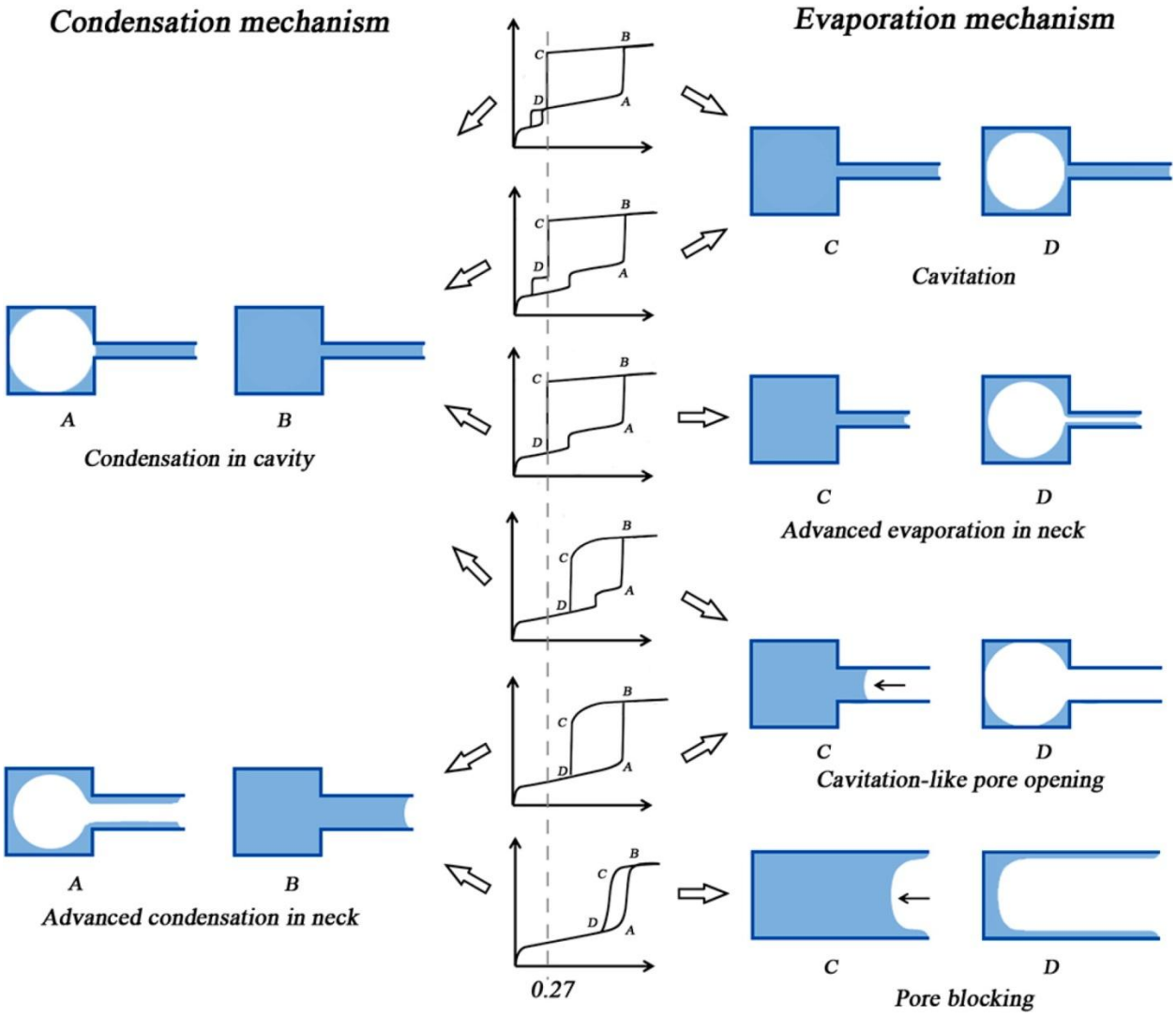

Figure 5.5 Evolution of condensation and evaporation mechanism in ink-bottle pores.(*111*)

However, the dominant role of the conventional pore blocking mechanism as described above is under discussion. For example, Sarkisov and Monson applied MD simulation to probe diffusive mass transfer into model pores of well-defined geometry, such as ink-bottle pores.(*112*) They found that the large can empty during desorption even while the small pore remains filled with fluid, which is different from the classical picture based on the concept of pore blocking. Indeed, by varying the temperature of the adsorption experiment for a given adsorbent with ink-bottle geometry, a transition from cavitation induced evaporation to pore blocking has been

observed.(*107*) Fumi Hirose and coworkers measured the temperature dependence of the sorption isotherms of N_2 on four kinds of KIT-5 samples in the temperature range 72-118 K. Figure 5.6 plots the temperature dependence of the adsorption-desorption isotherm of nitrogen on a KIT-5 sample with expanded cavities prepared by hydrothermal treatment for 7 days at 393 K. The gradual desorption branch became a sharp one with increasing temperature, suggesting that the desorption mechanism is altered from pore blocking to cavitation with temperature.

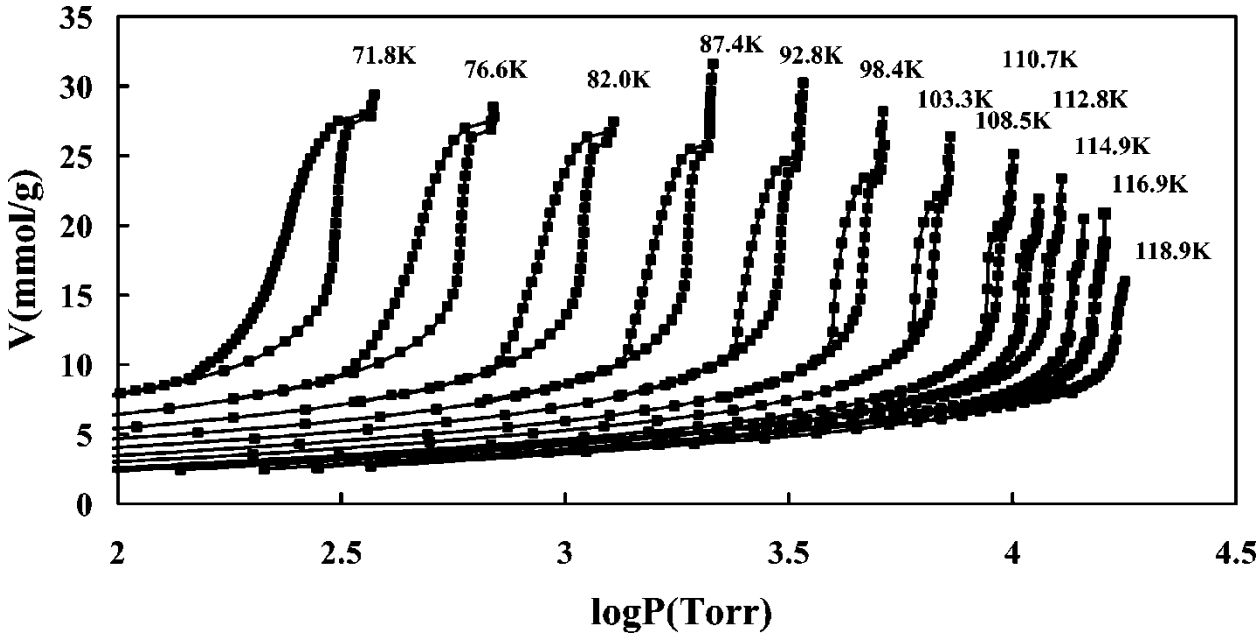

Figure 5.6 Temperature dependence of the adsorption-desorption isotherm of nitrogen on a KIT-5 sample with expanded cavities prepared by hydrothermal treatment for 7 days at 393 K.(*107*)

5.1.3 Hysteresis of Water Adsorption on Carbonaceous Materials

Hysteresis of water adsorption on porous carbons is one of the least understood phenomena in adsorption, due to the complex interplay between water-water interaction, water-carbon interaction, confinement, and functional groups. Figure 5.7 depicts water adsorption isotherms on carbon samples with different pore sizes. Adsorption isotherms of water on porous carbons generally show Type V, according to the IUPAC classification with a marked H1 or H2

hysteresis loop whose origin is believed to be different from simple gases adsorption in mesoporous solids.

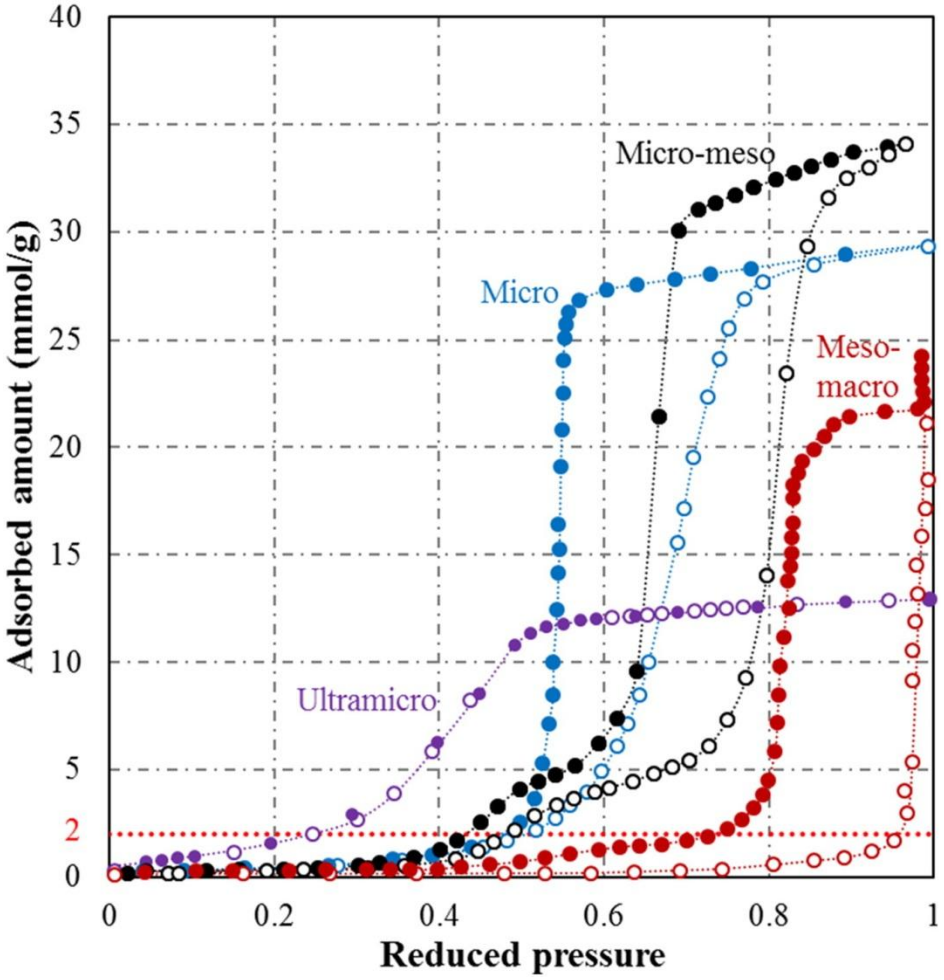

Figure 5.7 Water isotherms for highly ordered mesoporous carbon at 298 K, bimodal mesoporous carbon at 298 K, microporous wood-based AC at 297 K, and ultra-micropores at 303 K.(*79, 80, 82, 113*) Open circles: adsorption, solid circles: desorption.

The principal challenge in the interpretation of the water adsorption hysteresis on porous carbon is lack of a molecular level description of the states of the system and confined water along these isotherms. Recently, molecular simulations based on non-slit pore models have been used to explore the nature and spatial organization of the adsorbed states along the hysteresis

loop. For example, Lev Sarkisov and coworkers employed molecular simulation to study water adsorption on a high surface area activated carbon.(*114*) Figure 5.8, on the left, shows molecular visualizations of the structural element; on the right, shows the final pore network obtained after random packing of 190 structural elements in a cubic cell with a side length of 60 Å. The snapshots of different states of the system along the adsorption and desorption curve are shown in Figure 5.9. It can be seen that the adsorption is dominated by a two-phase process: coalesce of water clusters and formation of a single percolated water cluster. While the desorption is associated with a single water cluster shrinking in size via evaporation, followed by the disintegration in a series of smaller clusters.

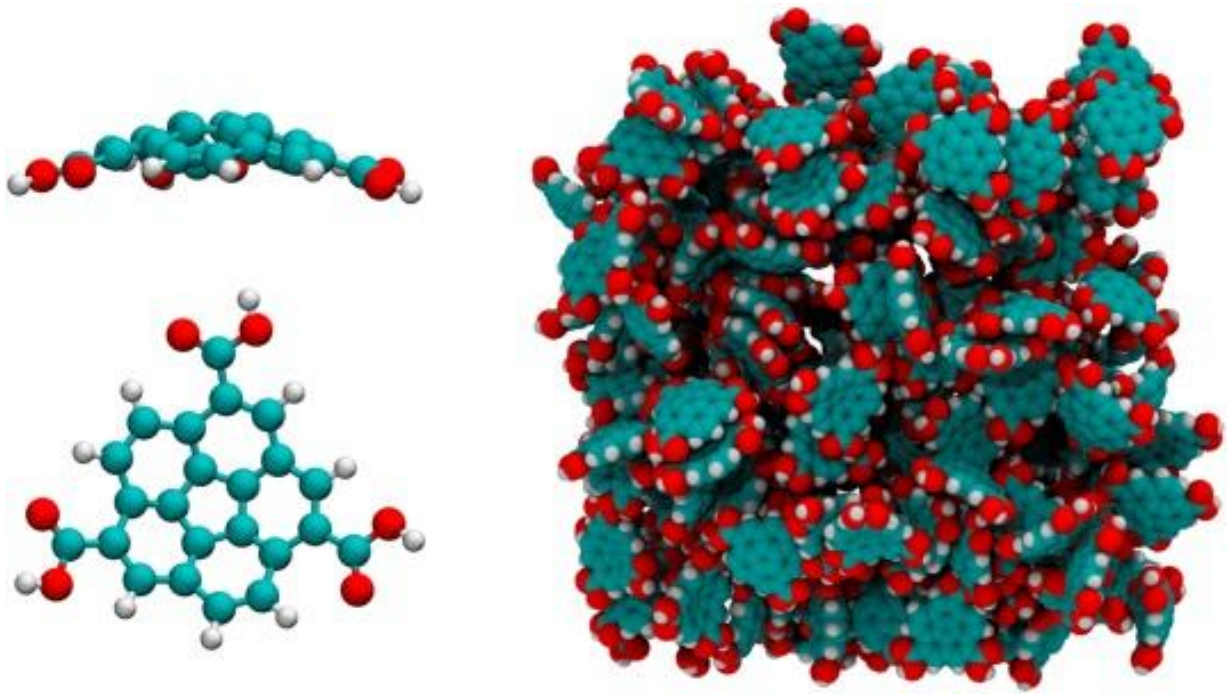

Figure 5.8 Left, computer visualizations of a corannulene-like element. Right, the final structure obtained from random packing of 190 elements. Cyan: carbon, red: oxygen, white: hydrogen.(*114*)

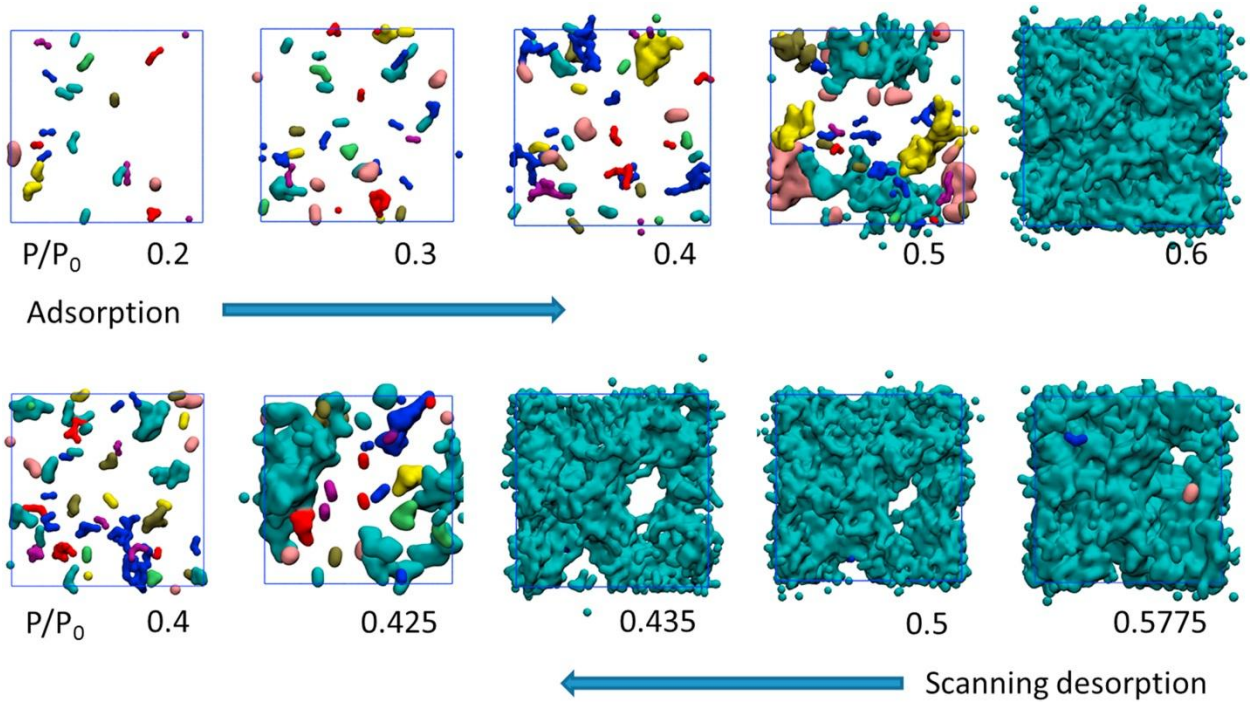

Figure 5.9 Molecular visualizations of the water clusters during different stages of adsorption and desorption. Coloring is used to distinguish separate clusters, however, the actual colors do not have any specific meaning.(*114*)

5.1.4 Structure Evolution of Water Clusters during Hysteresis Revealed by NMR

Those studies on the hysteresis of water adsorption on porous carbon have provided an important starting point for further studies. Of course, molecular simulations are not enough to build a valid picture of water in activated carbon. For this, in the current study, we applied NMR to correlate the macroscopic sorption isotherm with the microscopic molecular organizations of adsorbates, and thus understand the adsorption hysteresis on porous materials.

NMR has been used as a primary method to investigate fluids and gases inside porous media by applying external magnetic field gradients. In fact, when fluids are confined inside carbon nanopores, a spatially varying magnetic field, analogous to the field gradient in magnetic resonance imaging, appear naturally in the pore space due to the diamagnetic contributions of the

ring currents in the graphitic carbon surfaces. The NMR signals of molecules adsorbed inside carbon nanopores are shifted upfield compared to their freely moving counterparts. This upfield shift is called nucleus independent chemical shift (NICS) because it is not related to any chemical bond and thus is nucleus independent to a first approximation. NICS is determined by the distance between nuclei and surface and thus reflects a detailed molecular structure of adsorbate inside the nanoporosity. The comprehensive mechanism of water adsorption on microporous carbon revealed using NICS has been reported before and recently reviewed by Do et al.

In the following, we will deal with the adsorption hysteresis of water on nanoporous carbon, which is a typical example of the liquid partially wetting the solid surface. The water sorption isotherm detected by in situ NMR shows a marked hysteresis at moderate relative pressures (P/P_0 = 0.5-0.8). Furthermore, taking advantage of the intrinsic magnetic field gradient inside carbon nanopores, we succeed in directly probing the structural transformation of adsorbed water assemblies along the adsorption/desorption process. Based on these observations, we propose a microscopic mechanism of water adsorption/desorption by nanoporous carbon and clarify the physical explanation for this observed hysteresis.

5.2 Experimental Details

5.2.1 Carbon Material Preparation

The experimental sample used is derived from heated treatment of the microporous activated carbon polymer, poly-ether-ether-ketone (PEEK). The preparation of the particular PEEK90 sample used is comprised of two steps: carbonization and activation. Initially, 2g of Victrex PEEK pellets are carbonized after heated at 900 ℃ for 30 minutes in an argon environment. This carbonized product is then left to cool in an argon environment at room

temperature and ground into small pellets ~0.3 mm in diameter. Under steam carried by an argon flow, the sample is reheated at 900 ℃ for a given activation time. Greater activation time leads to larger micropore sizes in the sample, caused by mass loss in the sample. For PEEK90, the sample is heated until 90% mass loss is seen. Mass loss is calculated using the mass after activation compared to after carbonization. Activated carbon samples generally contain two distinct pore structures: intergranular pores of size 10nm and uniformly slit-shaped micropores of size 2 nm or less.

5.2.2 Adsorption/Desorption Set-up

During adsorption, the sample was hydrated in a closed water environment for a set time, and the mass difference before and after this hydration gave the mass of water added to the sample. For desorption, the sample was placed in a desiccant for a set time and the mass difference before and after this drying period was taken as the mass of water leaving the sample. In both cases, the sample was kept in a 4mm MAS NMR rotor with the airtight O-ring plug removed to allow for sample interaction with the environment.

5.2.3 NMR Experiment

All ^{1}H NMR spectra were obtained using a 400 MHz pulse magic angle spin (MAS) system at room temperature. For each level of hydration, on both adsorption and desorption measurements, sequences to obtain the FID and T_1 measurements were used. Initially, a baseline measurement is found by running sequences on the dry carbon, and then subtracted from all subsequent measurements. The MAS spectrum is obtained by spinning the sample in the magnet-inserted probe at a spin rate of 8 kHz and using a single 90-degree pulse. The recovery time is set to $> 5T_1$ to ensure full recovery of the sample after each pulse. The T_1 was obtained using the inverse recovery method.

5.2.4 NMR-Detected Isotherm

All hydration isotherms were measured in a lab-made in-situ NMR system with a 34 MHz magnet at 293 K. A dried carbon sample is loaded into a quartz tube that is lowered into the NMR environment. This tube is then set up to either connect to a vacuum pump or to be filled by the water vapor for adsorption. The mass adsorbed is determined by comparing the peak intensities at each partial saturation to that of the dry sample and the fully saturated sample peaks. An adsorption isotherm is then obtained through plotting this peak data using the water-carbon mass ration as a function of the relative vapor pressure used to introduce the water into the quartz tube.

5.3 Results and Discussion

5.3.1 Sorption Isotherm of Water on Microporous Carbon

Figure 5.10 shows NMR-detected sorption isotherm of water on microporous carbon at 293 K. The carbon sample is derived from polyether ether ketone (PEEK), with an average pore width of 2.0 nm. This pore-width classification lies between micro- and mesopores as defined by IUPAC and thus can portray the water sorption in typical carbon micropores (< 2 nm) and small mesopores (2-50 nm). The amount adsorbed is given as water content θ which is defined as the mass ratio of water to the dry carbon. In Figure 5.10, the isotherm exhibits an S-shaped type V curve: negligible uptake at low relative pressures ($0 < P/P_0 < 0.55$), followed by a sharp rise at medium relative pressures ($0.55 < P/P_0 < 0.85$), and then a small increase approaching the saturation vapor pressure ($P/P_0 = 1$). Such a type V isotherm is attributed to a combined effect of weak adsorbate-adsorbent interactions (e.g. water-carbon) and strong adsorbate-adsorbate interactions (e.g. water-water).(*56*) The relatively small amount adsorbed prior to $P/P_0 = 0.55$ demonstrates that the nanoporous carbon sample used in the current study is highly hydrophobic

and possesses very few functional groups on its surface.(*63*) Thus, the water-nanoporous carbon system can be modeled as water in slit-shaped and defect-free hydrophobic nanopores.

The observed hysteresis in Figure 5.10 is of the so-called type H1, which is typically found in materials with a narrow range of uniform mesopores.(*56*) Besides the difference in the quantity adsorbed, within the hysteresis region $0.55 < P/P_0 < 0.85$, the desorption branch of the hysteresis loop is steeper than the adsorption branch. Particularly, the adsorption path first increases gradually after an onset pressure of $P/P_0 = 0.55$, and then experiences a vertical uptake in the range of $0.8 < P/P_0 < 0.9$. In contrast, the desorption process starts with a plateau in the range of $0.63 < P/P_0 < 0.85$, followed by a steep drop in the range of $0.55 < P/P_0 < 0.63$. The phenomenon of hysteresis, as well as the distinct adsorption/desorption curve shapes, is due to different molecular organizations of water assemblies in the adsorption and desorption process, which is discussed below.

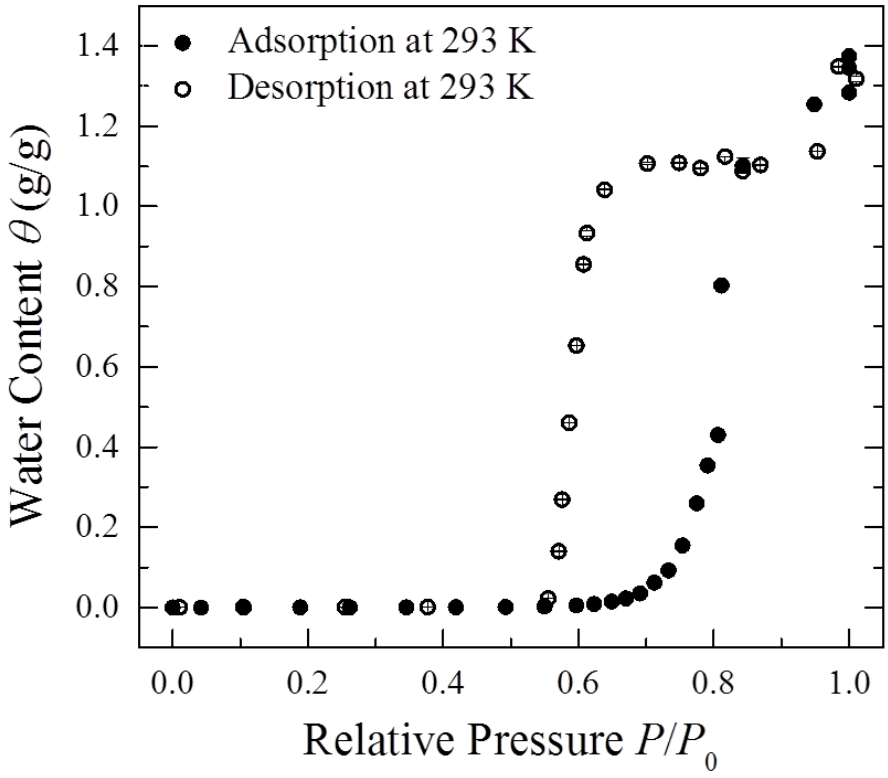

Figure 5.10 Experimental sorption isotherm of water on the PEEK-derived microporous carbon at 293 K. Filled and open symbols represent adsorption and desorption, respectively. Water content θ is defined as the mass ratio of water adsorbed to the dry carbon. P and P_0 are the equilibrium pressure and saturation pressure of water vapor at 293 K, respectively. At each pressure, NMR signal is measured five times when equilibrium is reached, and then the standard deviations of NMR peak areas are used to calibrate the error bars in the isotherms.

5.3.2 Structural Evolution of Water Assemblies in the Adsorption-Desorption Cycle

^{1}H MAS NMR spectra of water subject to microporous carbon in the hysteresis cycle are recorded, following the procedure given in ref 89.(*88*) Figure 5.11a shows ^{1}H MAS NMR spectra of water adsorbed by nanoporous carbon in the adsorption branch of the hysteresis. θ ranges from 0.04 to 1.09, corresponding to $0.55 < P/P_0 < 0.85$. The signal from the dry carbon has been subtracted from each spectrum. All the adsorption spectra have two peaks, both resonating at lower frequencies compared to the peak of the free bulk water (0 ppm). The

negative chemical shift of pore fluids (relative to the bulk) is due to the local magnetic field originating from the circulation of the carbon's delocalized π electrons in the applied magnetic field.(*20, 34, 115*) The two pore-fluid peaks are getting closer as θ increases and finally merge into a single peak at θ = 1.09. The left peaks centering at higher frequency (~ -4 ppm) correspond to water bridges spanning over the micropores, whereas the right peaks centering at lower frequency arise from water clusters nucleating on the surface functional groups.(*88*) This assignment is confirmed by the dependence of the chemical shift on θ: upon increasing θ, the water-bridge peaks stay constant at -4.1 ppm; in contrast, the water-cluster peaks shift gradually from -6.5 ppm to -4.5 ppm. The contrasting behaviors of water bridges and water clusters are due to their different growth mechanisms. Water bridges can only grow along the pore direction because of the constraints of pore walls. This horizontal expansion parallel to the pore surfaces does not alter the observed chemical shift. However, water clusters that sit on the surface of nanopores can grow towards the opposite wall. This cluster growth process shifts the water-cluster peaks to higher frequencies because the newly adsorbed water molecules experience less shielding from the carbon surface than the preadsorbed water. Another feature one needs to note that the water-cluster peak and water-bridge peak merge into a single peak at θ = 1.09 due to the coalesce of these two structures. While in the isotherm, the hysteresis ends at θ = 1.09, P/P_0 = 0.85, as well.

Figure 5.11b plots ^{1}H MAS NMR spectra of water-adsorbed microporous carbon in the desorption path of the hysteresis. Compared to the double-peaked adsorption spectra, all the desorption spectra are single-peaked, indicating a single percolating structure of water inside the nanopores.(*114*) In contrast to previous simulation studies which predict that the desorption

water clusters would disintegrate into a series of smaller clusters, our experimental results show that the in-pore water forms a single network throughout the entire desorption process.

Moreover, in Figure 5.12, individual ^{1}H NMR spectra of adsorption and desorption at the same hydration level are compared. Close to saturation θ = 1.10, the adsorption and desorption curve overlap with each other, displaying an identical state, i.e., nanopores fully filled with water. Besides this, two additional features should be noted. First, at each hydration level, the desorption peak is located between the two peaks of adsorption, indicating that the single peaks observed in the desorption process are equivalent to the coalescence of water clusters and water bridges. Second, the chemical shift of desorption peaks depend slightly on the water contents. In particular, the desorption peaks shift from -4.5 ppm to -4.9 ppm as θ decreases from 1.10 to 0.17, which is comparable to the shift of water-bridge peaks. The upfield shift of desorption peaks is because desorption occurs progressively from larger pores (1.37 nm) to smaller pores (1.24 nm).

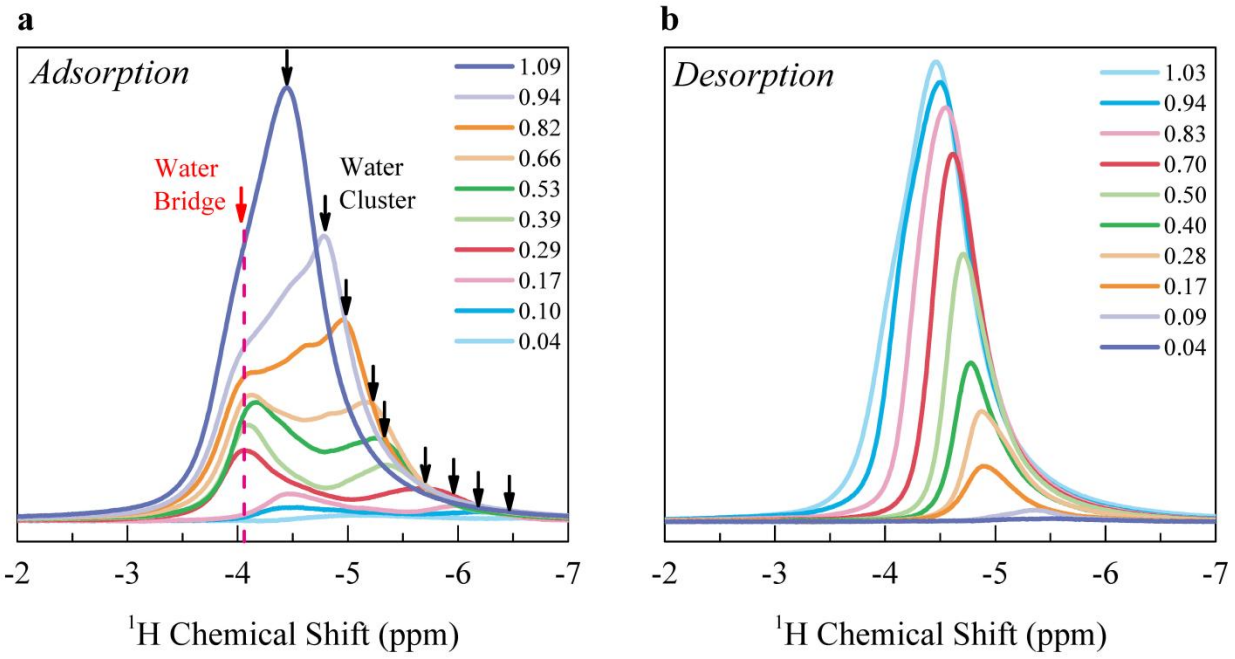

Figure 5.11 ^{1}H MAS NMR spectra of water subject to microporous carbon as a function of water content θ in the (a) adsorption and (b) desorption process, respectively. The vertical dashed line is shown as a reference so that the shift of peaks due to altering water contents can be distinguished.

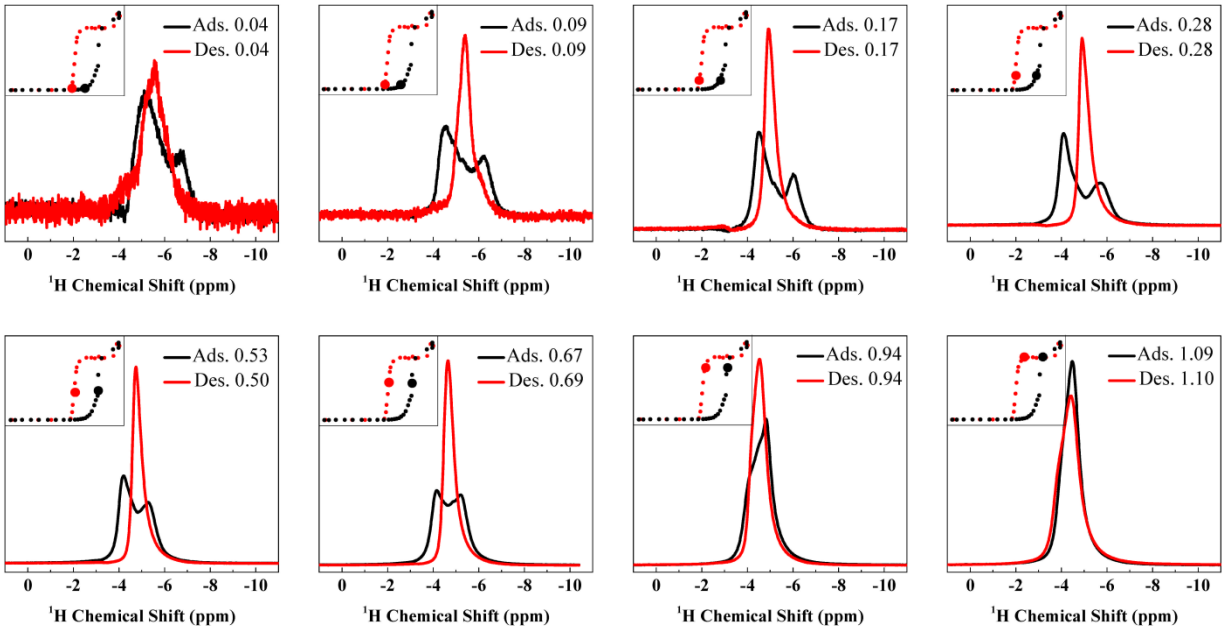

Figure 5.12 Individual ^{1}H MAS NMR spectra of water adsorbed in the microporous carbon at varying hydration levels in both the adsorption and desorption process. The inset figures mark the individual hydration level on the isotherm curve.

5.3.3 Mechanisms of Adsorption and Desorption of Water on Hydrophobic Micropores

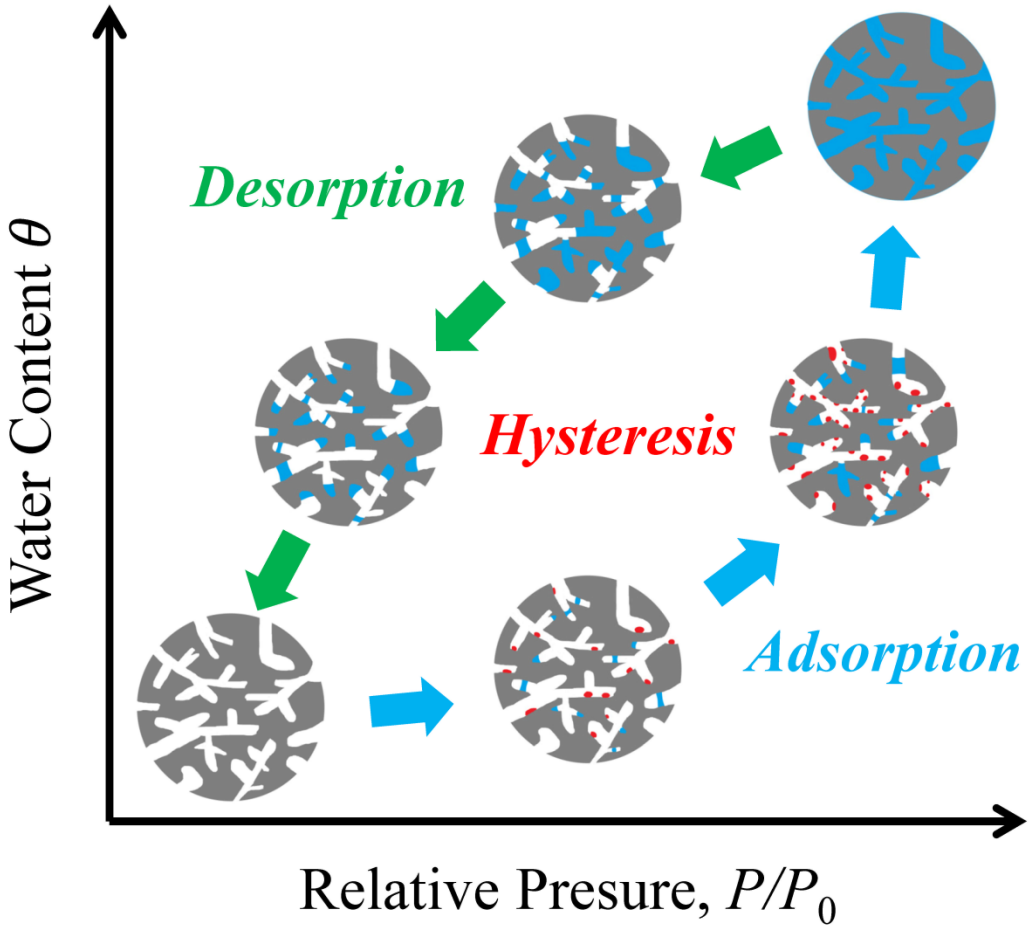

Figure 5.13 Proposed mechanism of adsorption and desorption of water on hydrophobic nanopores. Grey: nanoporous carbon. Red: water clusters. Blue: water bridges.

The combination of in situ NMR-detected isotherm and structural information obtained by NICS-resolved NMR provide the whole picture of the adsorption hysteresis for a case in which the liquid only partially wets the surface. A schematic illustration of the water in nanoporous carbon as an example is depicted in Figure 5.13.

In the adsorption branch, prior to the vapor condensation in pores (here at $P/P_0 = 0.8$), the filling of nanopores is induced by a cooperative process of nucleation of water clusters on

functional groups and formation of water bridges between pore walls. When these two structures are large enough, they form a percolating network to fill the nanopores. In the desorption branch, nanopores remain filled until the applied pressure decreases to the in-pore vapor-liquid transition pressure ($P/P_0 = 0.6$). The dehydration happens within an extremely narrow pressure range, $0.55 < P/P_0 < 0.64$, compared to the adsorption which is $0.55 < P/P_0 < 0.85$. Observations from NMR show that the desorption features a single percolating water structure; that is, a single cluster of water shrinks in size as water evaporates from nanopores. NMR study also reveals the water evaporation sequence: pore emptying occurs progressively from larger pores to smaller pores because larger pores imply less enhanced surface-water interactions.

5.4 Summary and Outlook

In summary, we report a microscopic scenario for the molecular mechanism responsible for the adsorption hysteresis for systems in which the bulk liquid partially wets the pore surface. While previous research had focused on isotherms, which only provide information on the quantity adsorbed, the present study directly monitors the structural changes of pore-fluids along the adsorption/desorption process, and thus correlates the macroscopic sorption isotherm with the microscopic molecular configurations. It is shown that the adsorption starts with the nucleation of water clusters on the functional groups and the formation of cooperative water bridges between the pore walls. This is followed by coalesce of these two structures, where the hysteresis loop ends. However, the desorption features a single percolating structure of water, which shrinks in size as water evaporates. The dehydration is associated with the equilibrium vapor-liquid transition in the pore, which depends only on pore size and is irrelevant to the functional groups that play a crucial role in the adsorption process. The distinct molecular configurations of

water assemblies in the adsorption and desorption process lead to different vapor-liquid transition pressures, resulting in the adsorption hysteresis.

CHAPTER 6 CAPTURE OF CHEMICAL WARFARE AGENTS (CWAS) SIMULANTS BY METAL-ORGANIC FRAMEWORKS IN PRESENCE OF WATER

6.1 Context and Scope

Metal-organic frameworks (MOFs) are an emerging class of porous materials consisting of metal nodes connected by organic linkers.(*116-118*) Compared to conventional inorganic porous materials such as zeolites, MOFs have ultra-high porosity (up to 90% free volume), enormous high surface area (extending beyond 6000 m^2/g) as well as the potential for more flexible rational design through control of the architecture and functionalization of the pores.(*119*) These unique advantages make MOFs an appealing class of materials for the capture and degradation of chemical warfare agents (CWAs).(*120*) For example, recent research has discovered that some MOFs can adsorb and catalytically degrade CWAs into nontoxic products via selective oxidation in addition to hydrolysis.(*121*) These detoxification methods are quite attractive because the harmful agent is contained within the MOF and destroyed within a matter of minutes.

However, fewer studies have been done to trace the adsorption of CWAs onto MOFs, in part due to the challenge of differentiating between in- and ex-pore adsorbates with common spectroscopies. Exploring these adsorption mechanisms in detail will allow researchers to better optimize MOFs catalysts for detoxification of CWAs and their analogs. Another important factor needs to be taken into account is MOFs behavior in the presence of water.(*122*) In fact, water or moisture is ubiquitous in practical processes and can greatly influence MOFs performance in some cases. For example, Randall Snurr *et al.* showed that small amounts of preloaded water (4

wt%) can enhance the CO_2 uptake capacity of HKUST-1; however, a fully hydrated HKUST-1 sample adsorbs very little CO_2 at all pressures.(*123*) In addition to the performance effects, the stability of MOFs under humid conditions must be considered as well. Earlier porous MOFs made from divalent metals, such as Zn^{2+} or Cu^{2+}, are rather unstable to moisture. For instance, MOF-5, a prominent milestone in MOF research, decomposes gradually upon exposure to moisture in the air.(*124*)

UiO-66 (Universitetet i Oslo) is a good adsorbent for CWAs detoxification due to its high surface areas and diverse functionality, and more importantly, owing to its remarkable thermal and chemical stability.(*125*) This chapter examines the adsorbate binding sites of CWAs simulant materials in UiO-66 with NMR spectroscopy. The effect of preadsorbed water on the uptake amount and mass transport of adsorbates is also investigated.

6.1.1 Structure and Properties of UiO-66

UiO-66 is made up of $Zr_6O_4(OH)_4$ nodes with 1,4-benzene-dicarboxylate (BDC) as linkers. (See Figure 6.1) The inner node has six Zr^{4+} ions in octahedral geometry and four oxygen atoms or hydroxyl at the centers of each of the facets of the octahedra. Each $Zr_6O_4(OH)_4$ node is coordinated with 12 BDC linkers to form a network with face-centered cubic (fcc) topology. A notable feature of UiO-66 is the high stability under thermal (up to 500 ℃) and chemical (pH = 1-12) conditions. This stability arises primarily from the strong Zr-O bonds formed between the node and linker.

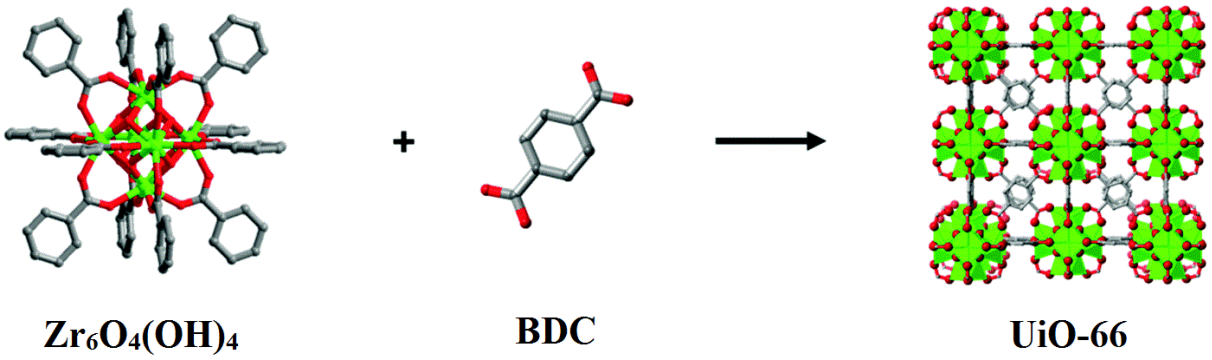

Figure 6.1 The building unit, linker and the structure of UiO-66.(*120*)

Another prominent property of UiO-66 is two types of cages with tetrahedral (0.7 nm) and octahedral (0.9 nm) shapes that can be accessed through triangular windows of about 0.6 nm. As illustrated in Figure 6.2, the orange and green sphere represents octahedral and tetrahedral pores, respectively; and the yellow cylinder represents the channel connecting these two pores. Given their known outstanding thermal and chemical stability, as well as high porosity, UiO-66 is among the most promising classes of potentially catalytic materials for deployment in personal chemical protection.

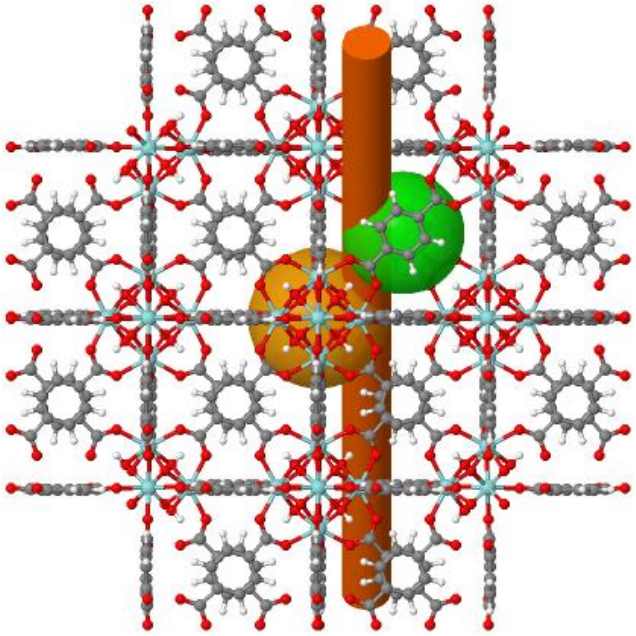

Figure 6.2 UiO-66 has two types of cages. Green sphere represents the tetrahedral pore (0.7 nm). Orange sphere represents the octahedral pore (0.9 nm). Yellow cylinder represents the channel connecting the tetrahedral and octahedral pores.

6.1.2 Nucleus-Independent Chemical Shifts (NICSs) of UiO-66

Our study (Chapter 4&5) of water confined in microporous carbons demonstrates that the guest molecules experience a reduced magnetic field next to the conjugated aromatic rings due to the aromatic ring current effect. Moreover, the quantitative relationship between measured δ_{NICS} and r can be exploited to probe the local environment of adsorbate molecules. Similarly, the abundance of conjugated aromatic rings in MOF linkers can also be explored to study molecular adsorption. In fact, DFT calculation shows that NICS due to organic linker ring currents dominate the observed chemical shifts for adsorbates when there are no chemically specific adsorbent-adsorbate interactions.(*126*) Jeffrey Reimer *et al.* calculated NICSs for the tetrahedral and octahedral pores of UiO-66. Heat maps of the NICS as a function of position inside of the tetrahedral and octahedral pores are shown in Figure 6.3.(*126*) It is revealed that adsorbates in

the tetrahedral pores exhibit negative NICS values, while adsorbates in the octahedral pores have positive values. The contrasting NICSs of adsorbates in the tetrahedral and octahedral pores indicate that we can use the NICS-based NMR technique to probe molecular binding sites in MOFs.

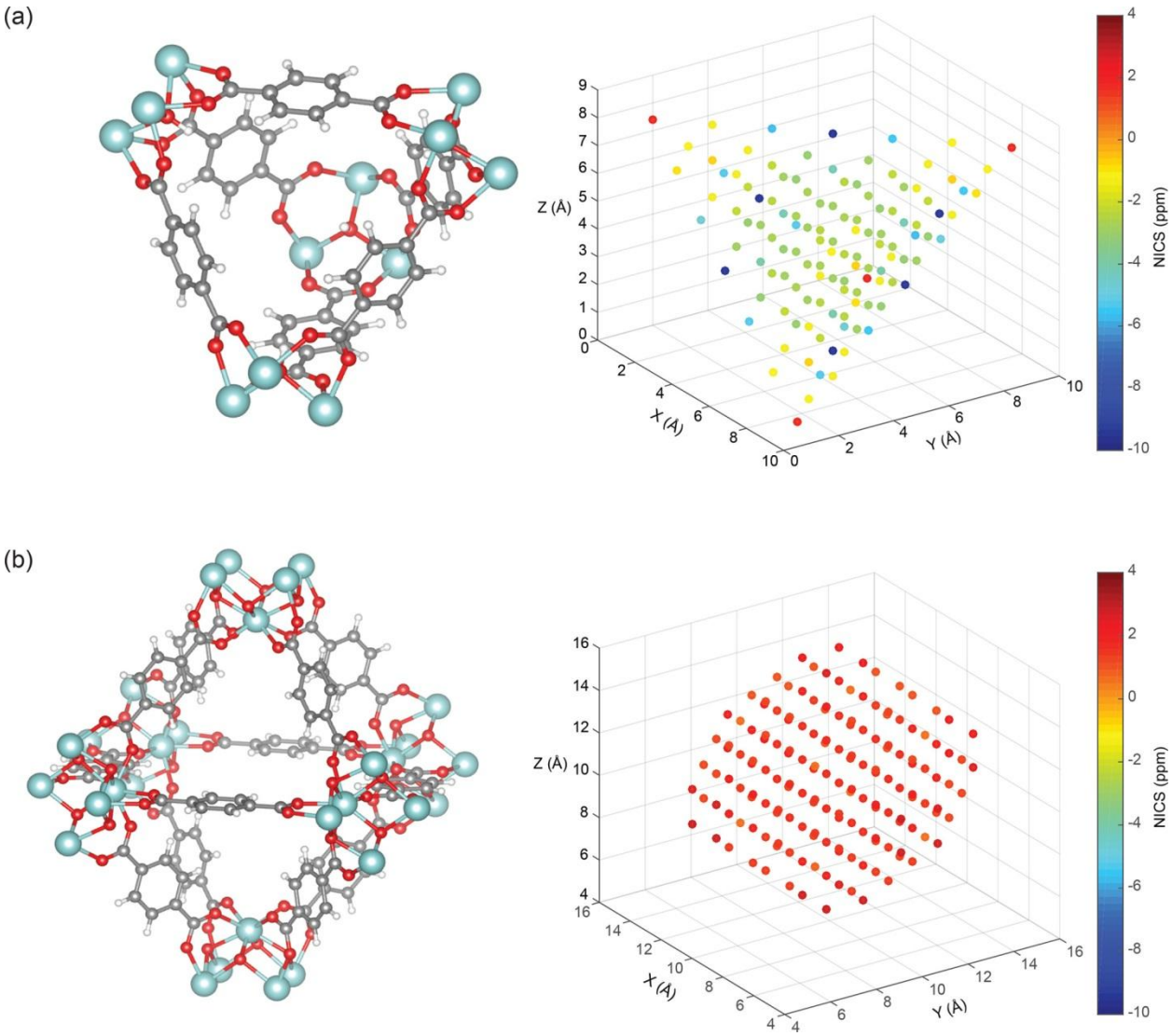

Figure 6.3 NICSs as a function of position inside of the (a) tetrahedral and (b) octahedral pores of UiO-66. The X, Y, and Z coordinates are arbitrary axes that define the coordinates of the pore.(*126*)

6.2 Experimental Details

First of all, I want to note that due to the danger involved in working with highly toxic CWAs, experiments are done using simulant materials (here we use isopropanol), which are safer to handle than actual CWAs but have similar chemical behavior and structure. (**Caution:** CWAs are *extremely dangerous* and should only be handled in a lab with proper facilities and certified personnel.) Later, the degradation performances of CWAs by MOFs will be carefully determined in a certificated lab. Here, we only discuss the adsorption of simulant materials on MOFs.

6.2.1 Isotherm Test: Single-Component Adsorption and Competitive Adsorption

In a single-component adsorption isotherm test, UiO-66 sample is first packed into an NMR quartz tube which is then attached to the lab-made NMR isotherm test system. After that, UiO-66 sample is evacuated for 24 h to remove any preadsorbed water. The ^{1}H FID signal of the dry sample is acquired by single-pulse excitation and is subtracted from subsequent spectra. Adsorbate vapor (water or isopropanol) is loaded to the sample at varying vapor pressures and the NMR spectra of the hydrated samples are measured. The adsorbate mass at saturation is found by direct weighing, while pre-saturation masses are determined based on intensity. The adsorption isotherms are obtained by plotting the adsorbate mass as a function of vapor pressure.

The competitive adsorption isotherm experiment is conducted in the following way. Dry UiO-66 is first loaded into the isotherm test system. Subsequently, water vapor is injected. After reaching equilibrium, the amount of adsorbed water on UiO-66 is determined to be 7 wt% (g water/g UiO-66), and $P/P_0 = 0.35$. Afterward, isopropanol vapor is loaded into the system.

6.2.2 Sample Preparation for Magic Angle Spinning (MAS) NMR

In a MAS NMR test, UiO-66 sample is packed into a 2 mm zirconia MAS NMR rotor. The rotor is weighed prior to and after packing to determine the mass of the packed UiO-66. For adsorption measurements, varying amounts of adsorbate are added by placing the rotor in a saturated vapor chamber at room temperature; for larger amounts of adsorbed vapor, the sample is immersed for a longer period, though the relationship is not consistently linear. (See Figure 6.4) The amount of adsorbate loaded is determined by finding the mass difference between the vapor-loaded sample and the initial, dry sample. Samples are also weighed after the completion of experiments and determined to be liquid-tight, with no sample loss.

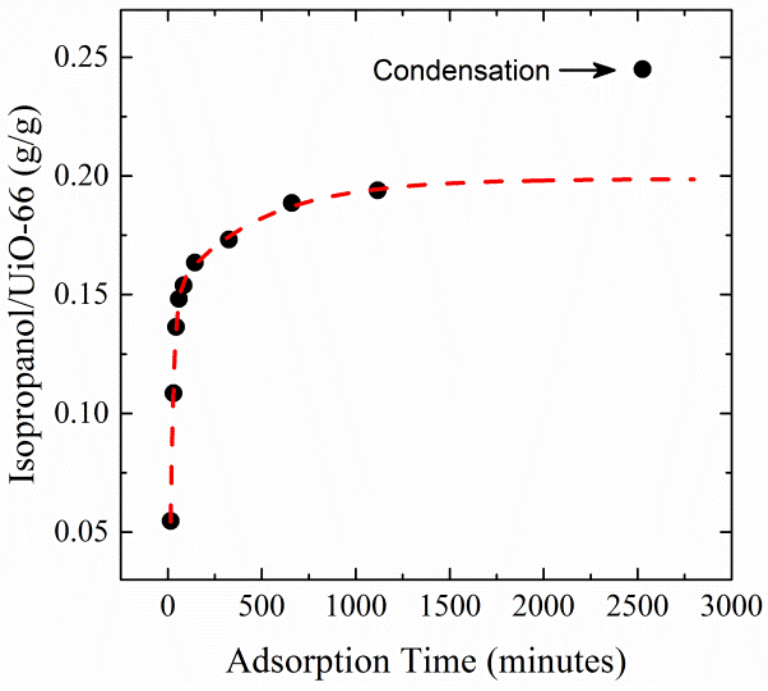

Figure 6.4 Time profile of isopropanol uptake in UiO-66. The sample reaches saturation ~1200 min. The abnormal high uptake at 2500 min is due to capillary condensation in the intergranular space.

6.2.3 NMR Experiment

All NMR spectra are measured on a 400 MHz pulsed NMR system at room temperature. The MAS NMR spectra are recorded at a spin rate of 25 kHz. ^{1}H adsorption experiments are performed using a spin echo (90°−τ−180°−τ−acquire) pulse sequence to eliminate the background signal, where τ is 1 ms in this test. The recovery time is set long enough (> $5T_1$) to ensure that the signal fully recovers after each scan.

6.3 Results and Discussion

6.3.1 Single-Component Adsorption Isotherm

In Figure 6.5 is shown the single-component adsorption isotherm for water in UiO-66. The amount adsorbed is given as water content which is defined as the water mass divided by the UiO-66 mass. Water adsorption in UiO-66 displays a reversible type V isotherm, which indicates that the material is weakly hydrophobic. The pore-filling step occurs near P/P_0 = 0.2 with very little adsorption below this point, and the saturation loading is approximately 0.25 g/g.

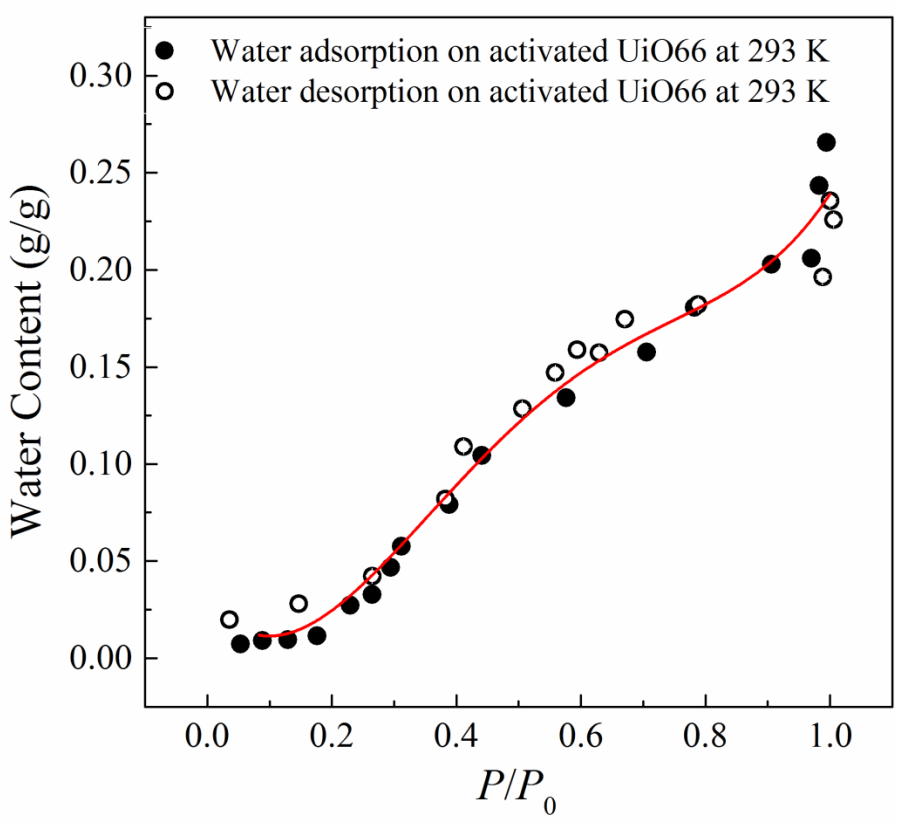

Figure 6.5 Amounts of water in activated UiO-66 as a function of relative vapor pressure P/P_0 on the adsorption (filled symbols) and desorption (open symbols) branches of the isotherm at $T = 293$ K.

Prior to the competitive adsorption of isopropanol in the presence of water, pure isopropanol isotherm on UiO-66 is measured at 293 K. As shown in Figure 6.6, the adsorption of isopropanol on UiO-66 exhibits a reversible Type II isotherm. The uptake amount increases rapidly at low relative pressure (below $P/P_0 = 0.2$), indicating a strong interaction between isopropanol and UiO-66. After that, the uptake amount of isopropanol increases gradually in the range of $0.2 < P/P_0 < 0.8$, followed by a vertical jump near $P/P_0 = 1$, which is due to the condensation of isopropanol in intergranular spaces.

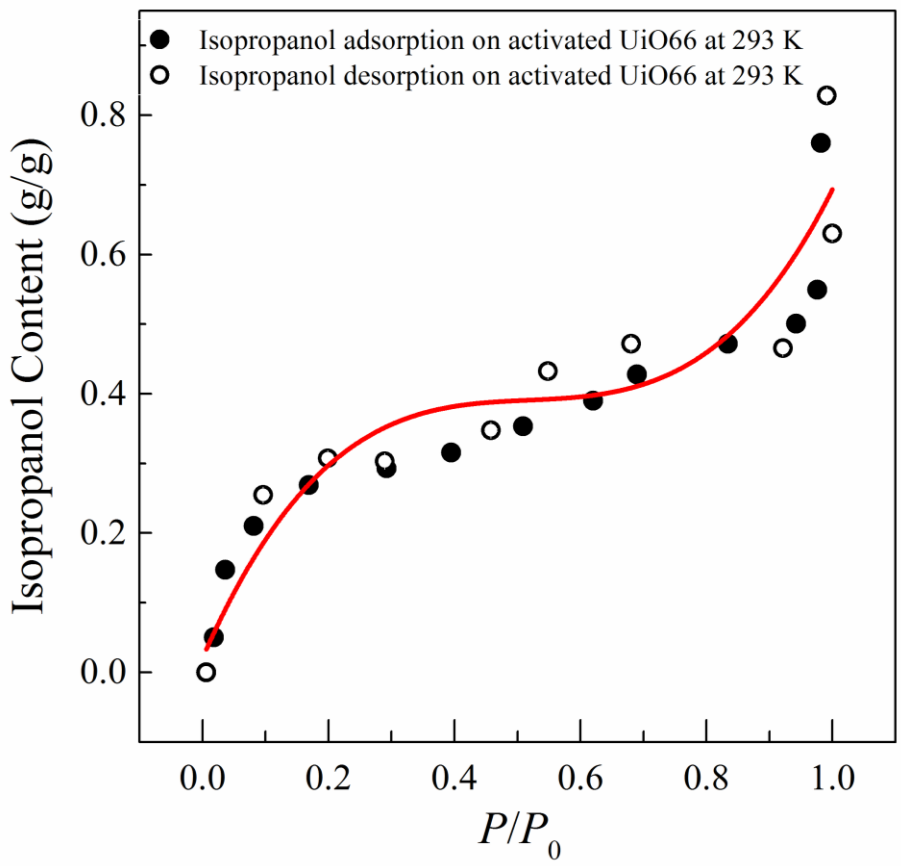

Figure 6.6 Amounts of isopropanol in activated UiO-66 as a function of relative vapor pressure P/P_0 on the adsorption (filled symbols) and desorption (open symbols) branches of the isotherm at $T = 293$ K.

6.3.2 Competitive Adsorption of Isopropanol on UiO-66 in the Presence of Water

Competitive adsorption of isopropanol on UiO-66 with preadsorbed water is conducted to follow the effect of water on isopropanol adsorption. Figure 6.7 shows the isotherms of isopropanol in a dry UiO-66 sample and in UiO-66 subjected to humidity $P/P_0 = 0.35$ (7 wt%). The adsorption isotherm on UiO-66 with preadsorbed water has a similar shape with that on dry activated UiO-66. This indicates that preadsorbed water has little effect on the interaction between UiO-66 and isopropanol. However, the uptake of isopropanol on the UiO-66 sample is reduced by 8 wt% in the presence of water, indicating that isopropanol and water have some identical binding sites.

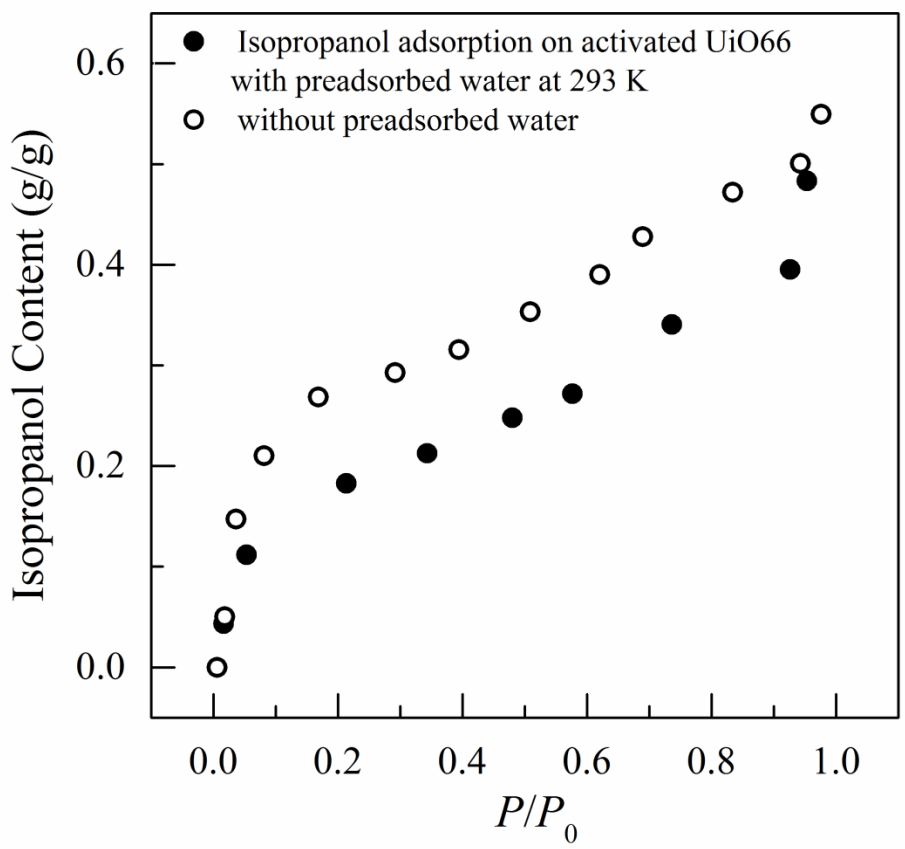

Figure 6.7 Adsorption isotherm of isopropanol on dry activated UiO-66 (open symbols) and on UiO-66 with preadsorbed water (filled symbols) at T = 293 K.

6.3.3 Diffusion of Isopropanol in Presence of Water

Figure 6.8 shows the time dependence of the uptake of isopropanol following a relatively small change of the relative pressure: for both dry and hydrated samples, Left, P/P_0 increase from 0.007 to 0.04; Right, P/P_0 increase from 0.04 to 0.20. Since the ^{1}H NMR test can be acquired typically in 30 s, it can be used to follow the fast mass transport of isopropanol into UiO-66. As shown in Figure 6.8, isopropanol adsorption on dry UiO-66 is quite fast; it took about 50 min to reach equilibrium. However, the presence of preadsorbed water significantly decelerates this process. It took over 300 min to get equilibrium. This slow process can be a rate-limiting step in decontamination applications.

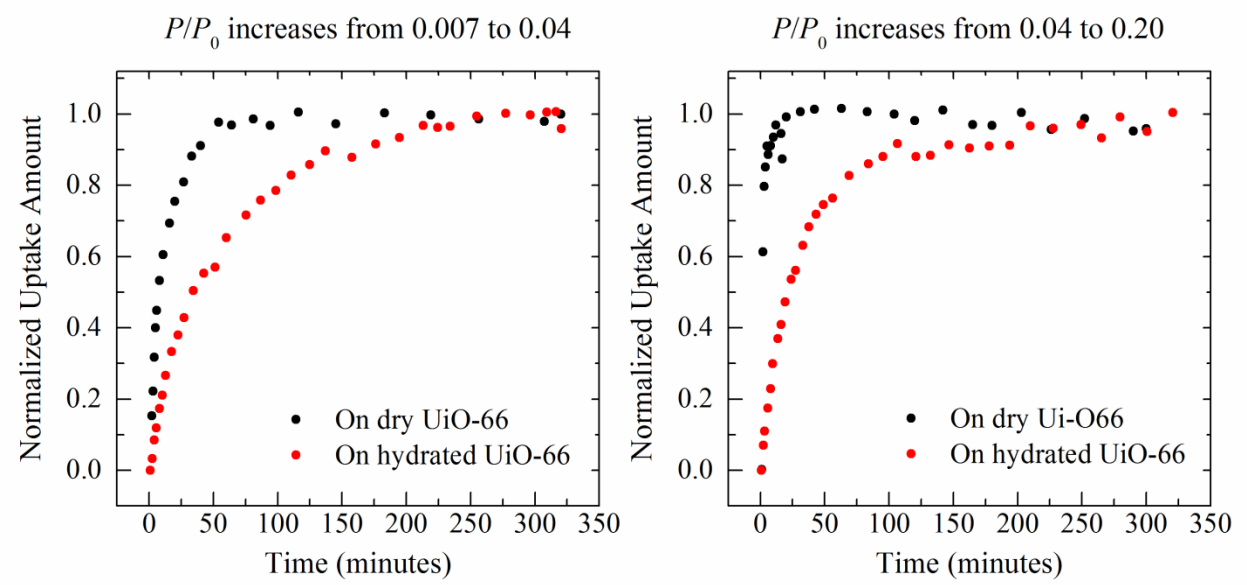

Figure 6.8 Adsorption kinetic data obtained upon stepwise change of the relative pressure. Left, for adsorption on dry UiO-66, P/P_0 increases from 0.007 to 0.04, while for adsorption on hydrated UiO-66, P/P_0 increases from 0.01 to 0.05. Right, for adsorption on dry UiO-66, P/P_0 increases from 0.04 to 0.18, while for adsorption on hydrated UiO-66, P/P_0 increases from 0.05 to 0.21.

6.3.4 ^{1}H MAS NMR Spectra

As discussed in Section 6.1, the NICS-induced chemical shift can be used to probe the binding sites of isopropanol inside UiO-66. ^{1}H MAS NMR spectra of the isopropanol adsorbed into UiO-66 for a range of mass loadings are shown in Figure 6.9. For ^{1}H NMR spectra at low isopropanol loadings (5.4 wt%, red), the spectrum contains a single peak, shifted significantly by -1.1 ppm to the right, at lower frequencies with respect to the bulk isopropanol -CH_3 peak (here set to 0 ppm). The observed negative chemical shift value (-1.1 ppm) suggests that isopropanol favorably adsorbs in the tetrahedral pores, based on NICS calculations. As the isopropanol loading increases, for example at 13.6 wt%, two peaks emerged, -0.28 and -0.38 ppm, both at lower frequencies with respect to the peak of neat isopropanol. We posit that the smaller NICS (-0.28 ppm) may correspond to a defective region (fewer terephthalate linkers result in fewer ring

currents to contribute to a negative NICS); whereas the larger NICS (-0.38 ppm) may due to exchange between the defective regions and tetrahedral pores, so averaging of the chemical shift is expected. Further increase in isopropanol loading to 18.9 wt% causes the line to broaden. When the isopropanol loading reaches 24.5%, a sharp peak emerged with a chemical shift identical to that of neat isopropanol, indicating saturation of the MOF pores and filling of the void space between crystallites. Moreover, a new peak with positive NICS value occurs at 0.25 pm, indicating that isopropanol also enters the octahedral pores.

The observed evolution of ^{1}H NMR spectra is exactly what expected in the following adsorption scenario. At low loading levels (< 10 wt%), isopropanol enters and resides in the tetrahedral pores of UiO-66. Upon further increase in loading (> 10 wt%), isopropanol molecules begin to occupy the defective regions of UiO-66. At even higher loading level (> 20 wt%) isopropanol molecules start to adsorb outside micropores in appreciable amounts, occupying the intergranular space.

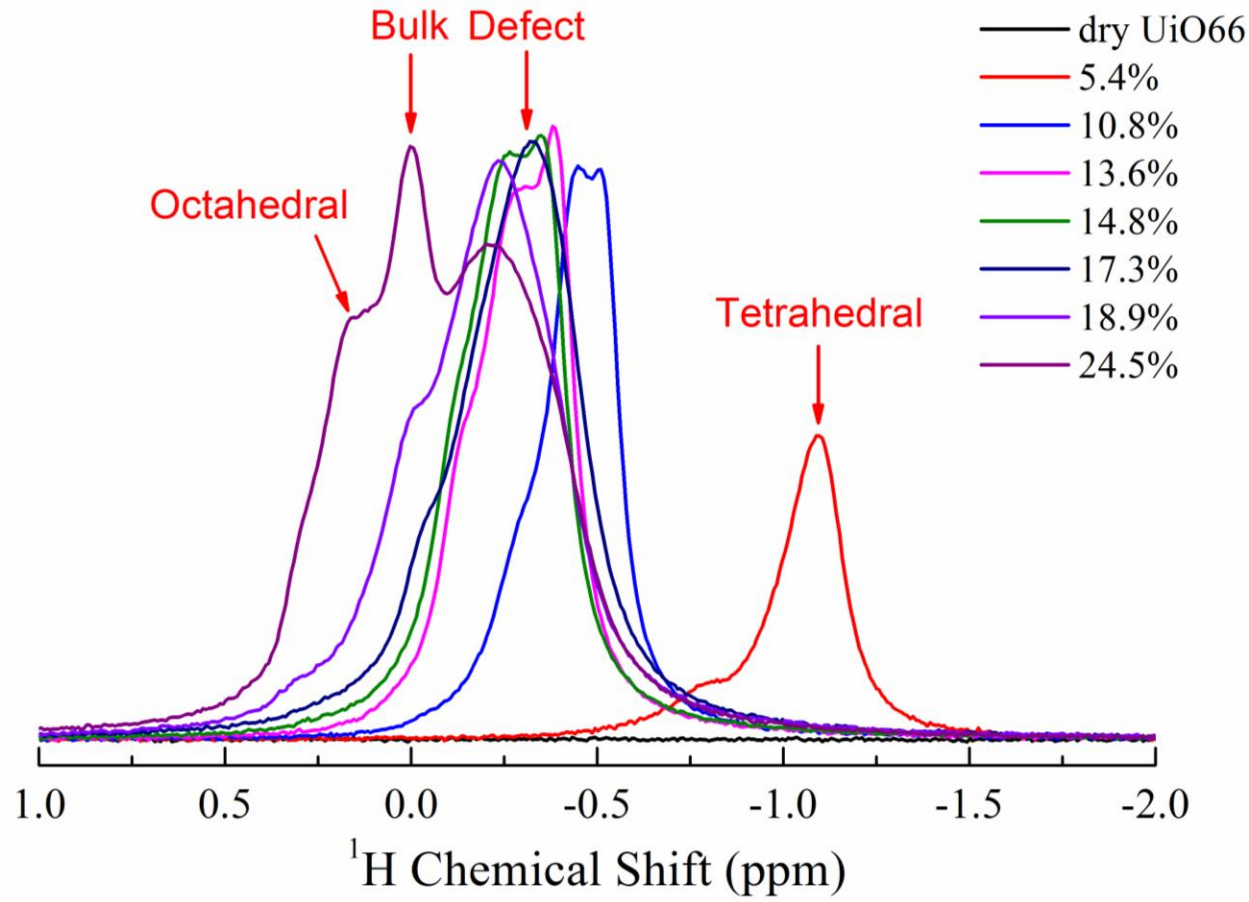

Figure 6.9 ^{1}H MAS NMR spectra of isopropanol adsorbed in UiO-66 at different loadings, ranging from 0 to 0.245.

6.4 Summary and Outlook

In this chapter, NMR spectroscopy has been used to probe the binding sites and mass transport rate of CWAs simulants inside the MOF UiO-66.

(1) Guest molecules adsorbed in the tetrahedral and octahedral pores of UiO-66 can be identified by resolved peaks with different chemical shifts. Specifically, adsorbates in the tetrahedral pores exhibit negative NICS values, while adsorbates in the octahedral pores have positive values.

(2) Depending on the relationship between chemical shift and adsorbate loading mass, a microscopic mechanism of isopropanol adsorption on UiO-66 has been proposed. It is

demonstrated that isopropanol fills the tetrahedral pores first and begins to occupy the defective sites and octahedral pores at higher loadings.

(3) The preadsorbed water has two effects on the isopropanol adsorption process. First, the preadsorbed water occupies some binding sites and thus reduce the saturation adsorption capacity for isopropanol. Second, the presence of preadsorbed water significantly decelerates the transport of guest molecules. The equilibrium time increases from 50 min on dry UiO-66 to over 300 min on the hydrated UiO-66, which could be a rate-limiting step in decontamination applications.

CHAPTER 7 DEMIXING OF WATER AND MISCIBLE ALCOHOLS UNDER NANOCONFINEMENT

7.1 Context and Scope

Interfacial phenomena at liquid-solid interfaces are of crucial importance in a wide range of natural and industrial processes, from biological processes to energy conversion.(*127-129*) Once in the interfacial region, models of bulk phase behaviors seldom survive intact due to the introduction of molecule-surface interactions. The interfacial effects are especially prominent when molecules are confined between solid surfaces separated by a few molecular diameters. In such systems, most of the molecules locate close to the interface and their properties are substantially altered by the surface, leading to interesting surface-driven phenomena.(*20, 130-139*)

Very recently, an increasing amount of experimental and simulation studies suggests that small miscible alcohols and water segregate at the hydrophobic interface under ambient conditions. This is quite surprising because, in the bulk phase, small alcohols such as methanol and ethanol are completely miscible in water across the entire range of concentrations, and the van der Waals interactions between the hydrophobic groups of small alcohols and the hydrophobic interface are usually considered too weak to stabilize alcohol molecules at the interface. More interesting, this microphase separation of alcohol/water mixtures is demonstrated to occur on many hydrophobic interfaces, including graphitic surfaces(*140, 141*), nanopores formed by graphene and mica(*4, 142, 143*), carbon nanotubes(*144*), graphene membranes(*145-148*), polyporous graphyne(*149*), hydrogen-terminated nanocrystalline diamond films(*150*),

hexagonal boron nitride (h-BN)(*148*), graphene oxide (GO) membranes(*151*), and highly ordered pyrolytic graphite (HOPG)(*152*). In the following, we firstly review the recently conducted research exploring the properties of confined alcohol-water mixtures. Then Section 7.2 and 7.3 show the application of NMR to reveal the physical insights into this novel phenomenon.

7.1.1 Experimental Studies of Confined Alcohol-Water Mixtures

Here I briefly discuss two main techniques that have been widely used to study the structure and dynamics of confined alcohol-water mixtures: atomic force microscopy (AFM)(*4, 152*) and scanning force microscopy (SFM)(*142, 143*). For example, Harold Zandvliet*et al.* sandwiched a monomolecular methanol-water film between few-layer graphene and mica. The experimental procedure is illustrated in Figure 7.1a. Figure 7.1b shows a typical AFM image of faceted methanol islands, formed by methanol-water mixtures confined between graphene and mica. Due to differences in dipole repulsion and mechanical deformation energy, methanol molecules deform graphene by approximately 0.8 Å more than water molecules, allowing for AFM imaging. This result shows a remarkable separation between water and methanol along the single molecular layer.

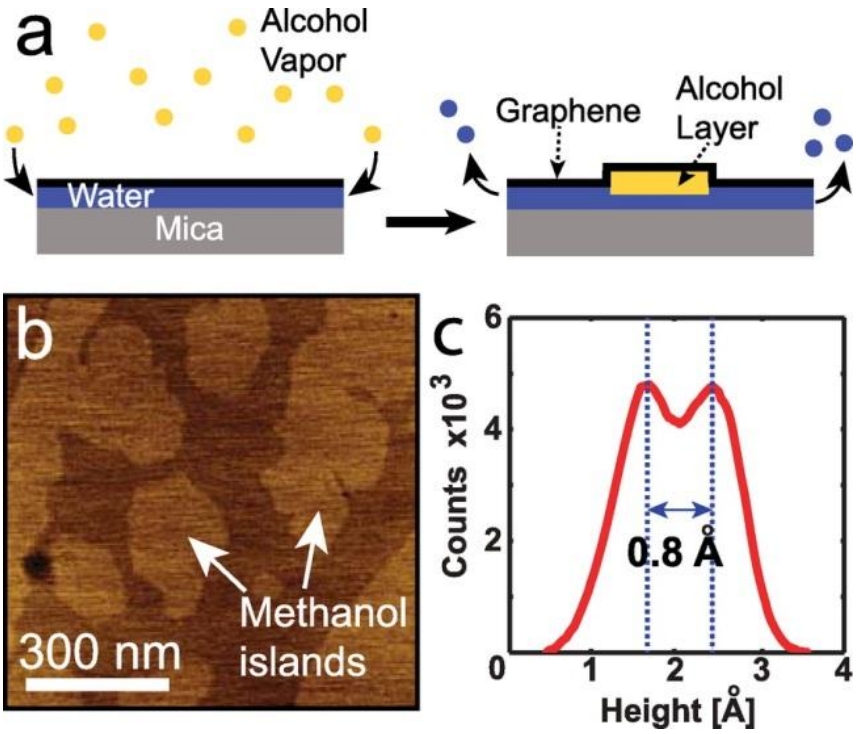

Figure 7.1 (a) Cartoon of the experimental procedure. Upon a change of the ambient vapor to alcohol vapor, water molecules evaporate from the graphene-mica interface through a pore, whereas alcohol molecules condensate via the pore and form 2D islands. (b) Methanol islands formed by the adsorption of methanol from methanol vapor. (c) Height distribution of the islands and their surroundings.(*4*)

Recently, Kislon Voïtchovsky applied *in situ* AFM to image the molecular arrangement of aqueous alcohol solutions at the interfaces with highly ordered pyrolytic graphite (HOPG).(*152*) Typical molecular structures formed by water and alcohol at the surface of HOPG are visible in Figure 7.2. In a ternary mixture of water, methanol, and ethanol the interface appeared covered by a regular array of longitudinal rows (white arrow in Figure 7.2a) running in parallel, with a periodicity of 6.1±0.2 Å (Figure 7.2b). This structure (6.1 Å) is too large for the HOPG itself and has been assigned to the self-assembly of the liquid molecules perpendicular to the direction of the main rows. Moreover, they also find that once formed, these structures are remarkably stable over a broad range of temperatures, from 10 to 60 ℃.

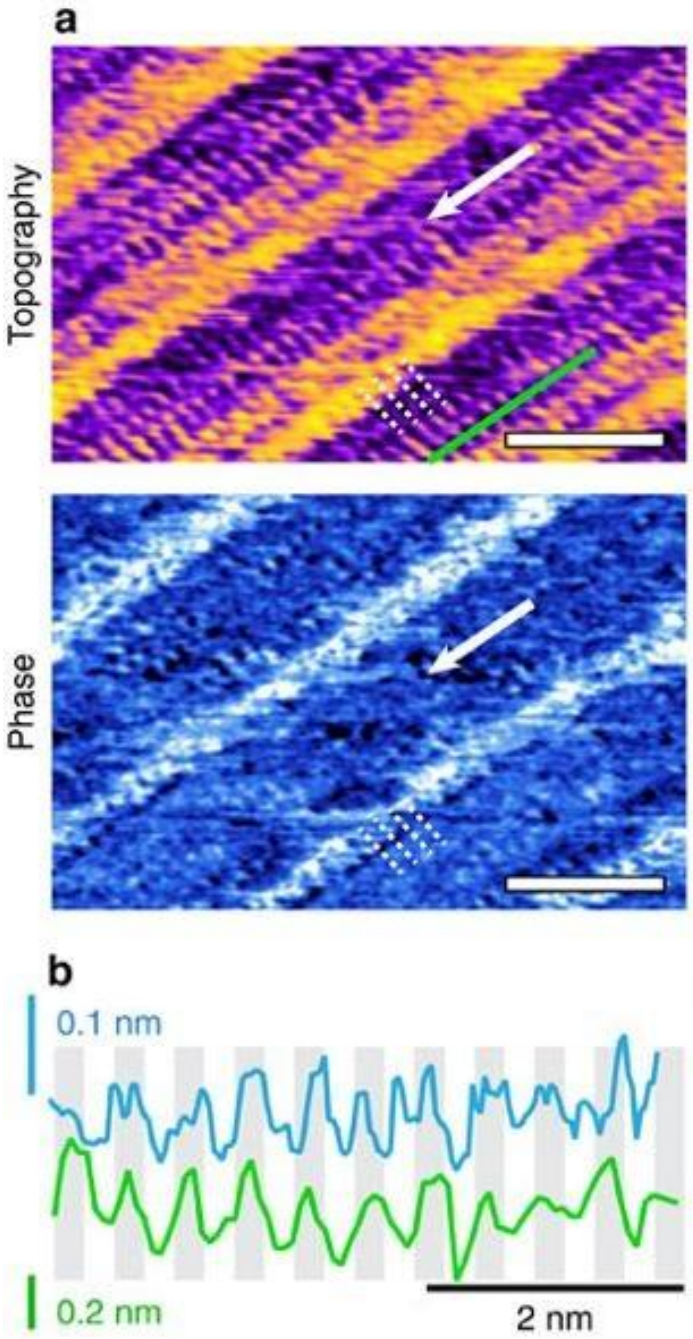

Figure 7.2 (a) Regular array of longitudinal rows (white arrow) obtained in a 1:1 water-methanol mixture spiked with < 1% ethanol. Each row is composed of several ~5 Å wide sub-rows running in parallel, and epitaxially following the underlying HOPG lattice. Finer structure with 6.1 ± 0.2 Å periodicity can also be seen perpendicular to the rows (dotted white lines), as evidenced by the green profile in (b) where the periodicity is highlighted.(*152*)

7.1.2 Molecular Simulation Studies of Confined Alcohol-Water Mixtures

A number of MD simulation studies have been implanted to probe the behavior of confined alcohol-water mixtures. For example, molecular dynamics (MD) simulations by Zhao *et al.* showed that a layered structure is formed within slit-shaped graphene nanopores. In Figure 7.3, they found that ethanol molecules are preferentially adsorbed on graphene surfaces and water molecules are displaced to the center of the pores.(*146*) Similar segregation phenomenon is also observed by a combined method of DFT and molecular mechanics simulations. As shown in Figure 7.4, Kislon Voïtchovsky *et al.* performed simulations using a super-cell geometry comprising eight graphite layers aligned along the *x*,*y* plane and separated by the methanol-water mixture. For five different methanol compositions, they consistently observed the formation of a strongly structured surface layer, with preferential segregation of methanol molecules in the first layer above the surface (Figure 7.4b).

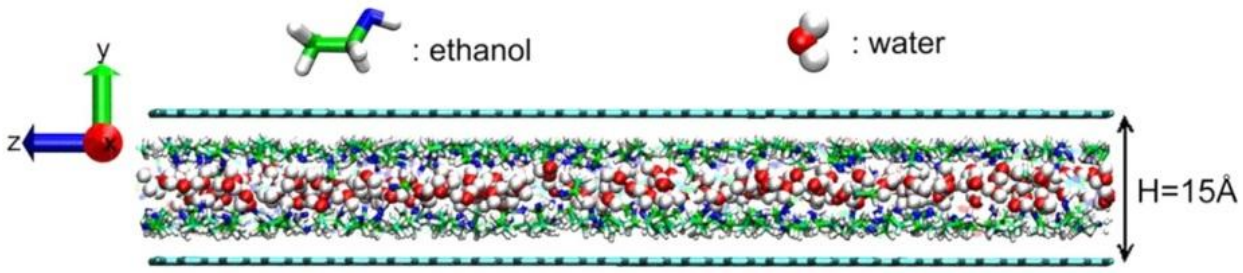

Figure 7.3 Simulation systems and typical snapshots. The cyan walls represent the graphene sheets.(*146*)

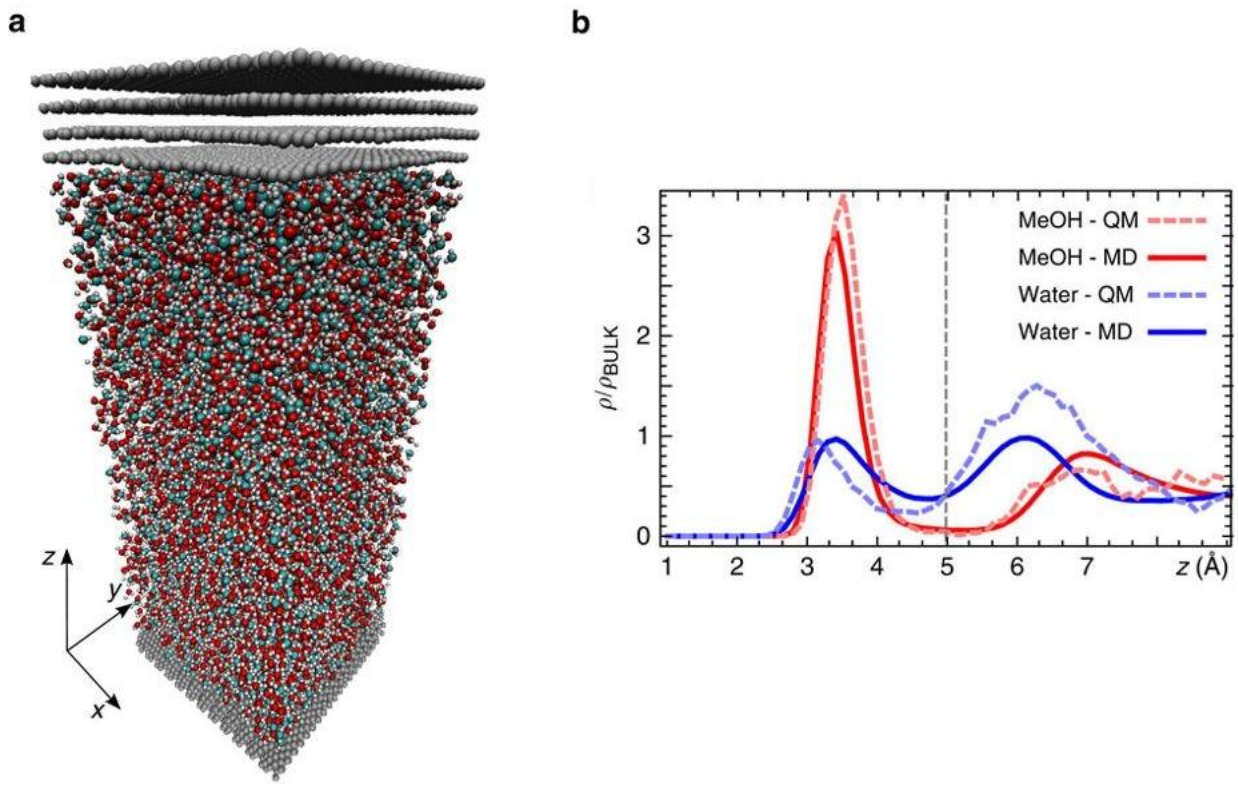

Figure 7.4 The simulations are performed to explicitly model mixtures of different concentrations on the surface of graphite. (a) A snapshot of the (50 × 50 × 150 Å) simulation supercell, using slab geometry with periodic boundary conditions. (b) The density profile along *z* for a 1:1 water:methanol mixture shows strongly structured water and methanol layers between 1 and 5 Å.(*152*)

7.1.3 Imaging Nanoconfined Aqueous Alcohol Solutions using NMR

Although significant progress has been made, there are many fundamental questions remained to be answered. First, a natural question raised is what the phase diagram of the system is and at what temperature this phase separation behavior would eventually disappear. Second, this demixing phenomenon needs to be experimentally confirmed because simulation studies cannot capture the formation of stable ordered structures at the interface due to the slow dynamics of demixing.(*152*) Third, previous experimental studies, either using AFM(*4*) or SFM(*142, 143*), could only investigate single or few-layer alcohol-water film sandwiched

between two solid surfaces. An experimental study of aqueous alcohol solutions under nanoconfinement is still yet to be done. Fourth, all previous experimental studies could only reveal the segregation of alcohol and water parallel to the surface. The demixing phenomenon normal to the surface has not been observed though it has been predicted by many MD simulations.(*140, 141, 144-149, 153*) Last but not least, the driving mechanism for this anomalous demixing phenomenon has yet to be accurately modeled. A variety of mechanisms have been proposed, such as differences in affinities to pore walls(*145, 146*), deformation energy of graphene sheets,(*142, 143*) and an energetic barrier caused by hydrogen bond loss(*149*). However, it is difficult to deem one better than another because current understanding of these mechanisms is hampered by the system complexity comprising of binary liquids and solid surfaces, and the difficulty in experimentally accessing their microscopic structure and dynamics. Furthermore, none of these studies take the hydrophobic effect into account. Yet, the hydrophobic effect is likely to play an important role because of the hydrophobic nature of both the solid surface and alkyl groups in alcohols.(*154*)

NMR has been used as a primary method to investigate confined fluids by applying external magnetic field gradients.(*155*) In fact, when fluids are confined in graphitic nanopores, a spatial-varying magnetic field, analogous to the field gradient in magnetic resonance imaging (MRI), appear naturally in the pore space due to the diamagnetic response of the ring currents in the graphitic surfaces.(*34, 88, 91, 156, 157*) Such an internal field gradient enables NMR to map confined fluids in carbonaceous materials with sub-nanometer scale spatial resolution.

Here, we took advantage of this NMR imaging capability to study the molecular organization of aqueous alcohols confined in graphitic-like nanopores. A systematic study of various miscible alcohols has been done, including methanol, ethanol, 2-propanol, and *tert*-

butanol. We find that the nanoconfined alcohol-water mixtures separate into an alcohol-rich phase in proximity to the pore surface and a water-rich phase at the pore center; while the unconfined mixtures have the same property with the bulk. Moreover, the segregated state remains significant at high temperatures up to 90 ℃. We also discussed the driving mechanisms for this unusual phase separation phenomenon by quantifying thermodynamics information from in situ NMR-detected vapor isotherms and from recent molecular simulations. Furthermore, it is demonstrated that this microscopic phase separation has important consequences for macroscopic properties, which is recognized by the contact angle measurements and vapor isotherm tests.

7.2 Experimental Details

7.2.1 Carbon Material Preparation

The sample studied is a microporous activated carbon derived from the high-temperature polymer, poly-ether-ether-ketone (PEEK). Generally, there are two different pore structures in each activated carbon sample: the intergranular pores of size larger than 10 nm and uniformly slit-shaped micropores smaller than 2 nm. The sample preparation process consists of two steps: carbonization and activation. During carbonization, 2 g of granulated Victrex PEEK pellets are heated in an argon atmosphere at 900 ℃ for 30 min, yielding the carbonized product. Then, the product is cooled down to room temperature in an argon environment, and ground into smaller particles of ~0.3 mm in diameter. The ground sample is again heated at 900 ℃ under water steam, carried by the argon gas flow, for a certain activation time. Different activation times lead to different micropore sizes. Due to possible inaccuracies in the BET techniques for pores of sizes smaller than 3 nm, a newly developed NMR method is used to characterize the pore size distribution.(*34*) The average pore sizes of the three samples used in this study are determined to

be 0.5 nm, 1.0 nm, and 1.6 nm, respectively, from the wall surface to wall surface, assuming a slit-shaped pore. (See Figure 7.5) The X-ray photoelectron spectrometry (XPS) data indicate that the surface chemistry of these nanoporous carbons is largely graphitic, suggesting a locally slit-shaped pore morphology.

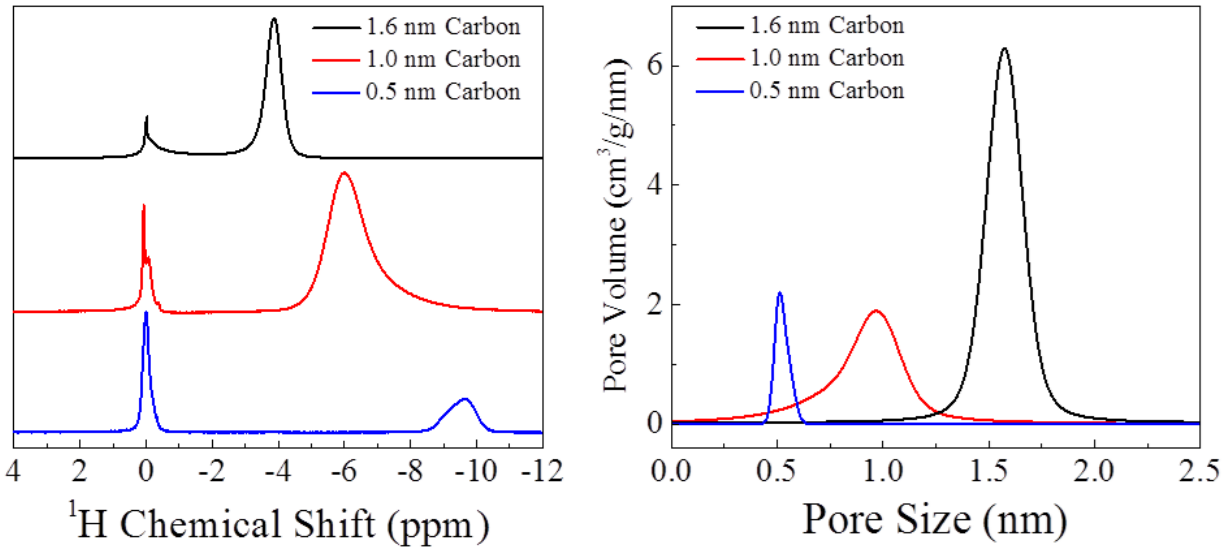

Figure 7.5 Micropore sizes of the three PEEK-derived carbon samples. Left: ^{1}H MAS NMR spectra of water in three microporous carbon samples. The chemical shift of the free water outside the pore (left peak) is set to 0 ppm. Right: Pore size distributions of the three microporous carbon samples. The main micropore sizes of the three samples are 0.5, 1.0, and 1.6 nm, respectively.

7.2.2 Alcohol-Water Mixture Preparation

The alcohols (methanol, ethanol, 2-propanol, and *tert*-butanol) and deuterium oxide (D_2O) are all purchased from Sigma Aldrich (purity > 99.9%) and used as received without further purification. Aqueous alcohol solutions are prepared by dissolving the alcohol in the D_2O with the desired mass fractions. The mixtures are subsequently vibrated in a multi-tube vortexer (Fisher Scientific) for 24 h to ensure thorough mixing.

7.2.3 NMR Experiment

All of the ^{1}H MAS NMR spectra were measured on a 400 MHz pulsed NMR system. The MAS NMR spectrum is obtained at a spin rate of 8 kHz by recording the free induction decay after a single 90-degree pulse (~ 5 μs). The recovery time is set long enough (> $5T_1$) to ensure that the signal fully recovers after each scan. In a typical measurement, 15 mg of the vacuum-treated activated carbon sample is loaded into a 4 mm rotor. Then, ~30 μL of aqueous alcohol solution is injected into the dried activated carbon and is then tightly sealed. Samples are weighed before and after experiments and determined to be liquid-tight. In the temperature-dependent test, the sample was heated to 90 ℃ first. Subsequently, a total of 4 scans (about 30 s) were accumulated for each measurement during the continuous cooling process at 1 K/min.

7.2.4 NMR-Detected Isotherm

The adsorption isotherms are measured in a lab-made *in situ* NMR system on a 34 MHz (0.8 T) magnet at 293 K. The dried 1.6-nm graphitic carbon is first loaded into a quartz tube inside the NMR detection coil. Then the sample tube is connected to a quartz manifold that can be either evacuated by a mechanical pump or filled with the desired adsorbate vapor for adsorption. The vapor pressure can be varied from millitorrs to the saturated vapor pressure P_0 of the adsorbate under study. After setting a certain pressure in the reservoir, opening the valve causes a stepwise increase of pressure in the sample. At each pressure, the NMR signal is measured 5 times after reaching equilibrium, and the average signal intensity $S(P)$ is used as the adsorption amount. The adsorption isotherm is obtained by plotting the normalized adsorption amount $\theta = S(P) / S(P_0)$ versus the relative vapor pressure P/P_0.

7.2.5 Contact Angle Measurement

Thee soda-lime glass slides purchased from Fisher Scientific are used as received. Hydrophobic surface is obtained via the silane-coating method in which glass slides are immersed in the chloro(dodecyl)dimethylsilane for 24 h. The reaction can be represented as follows.

$$CH_3(CH_2)_{11}Si(CH_3)_2Cl + \text{-Si-OH} \rightarrow \text{-Si-O-}Si(CH_3)_2(CH_2)_{11}CH_3 + HCl$$

Following the silane coating, the treated glass slide is rinsed with ethanol to wash off any remaining organic materials. Static contact angles are measured using CAM 200 optical contact angle meter (KSV instruments). A liquid droplet of 2 μL is formed at the end of the syringe and carefully deposited onto the soda lime glass slide. The images of static contact angle are taken within 5 s of liquid deposition by a charge coupled device (CCD) camera. The static contact angle is calculated by the vendor-supplied software.

7.3 Results and Discussion

7.3.1 Distance-Dependent NICS Effect

Principals of the distance-dependent magnetic resonance effect are illustrated in Figure 7.6.(*34, 115, 156, 158-160*) In NMR spectroscopy, the externally applied magnetic field ($\vec{B}_{\text{external}}$) induces interatomic ring currents (red circle) within the delocalized π orbitals in the sp^2-hybridized carbon surface.(*161*) In turn, the ring current creates a local magnetic field ($\vec{B}_{\text{induced}}$) above the carbon surface. Density functional theory (DFT) calculations show that the induced local field $\vec{B}_{\text{induced}}$ opposes the applied field $\vec{B}_{\text{external}}$, giving a diamagnetic response.(*34, 156*) The interfacial nuclei are thus subject to a measurable magnetic shielding effect. Consequently, in the Fourier-transform NMR spectrum, the interfacial nuclei exhibit a resonance frequency shift and thus can be resolved from the bulk counterparts which are away from the surface and experience

no shielding effect. That is, using the corresponding peak of bulk species as reference, the interfacial peak would occur in the upfield portion of the NMR spectrum, centering at more negative chemical shifts. Since this phenomenon is not related to any chemical bond, the ring current effect is nucleus independent to a first approximation, *i.e.* the chemical shift of any nucleus will be shifted by a fixed amount, depending only on its location with respect to the carbon surface. The chemical shift caused by this ring current effect is referred to as the nucleus independent chemical shift (NICS), δ_{NICS}. Furthermore, the quantitative relationship between δ_{NICS} and the distance r between the nuclei being probed and the carbon surface allows the distance-dependent NICS effect to be utilized as a nanoscale ruler. As shown in Equation 7.1, δ_{NICS} is exclusively governed by r:

$$\delta_{\mathrm{NICS}}(r) = -24.5exp\left[-\left(\frac{r+0.17}{0.227}\right)^{0.754}\right].(34) \quad (7.1)$$

In short, using the distance-dependent NICS effect, we can easily distinguish the interfacial nuclei from the bulk signal and measure the nuclei-surface distance.

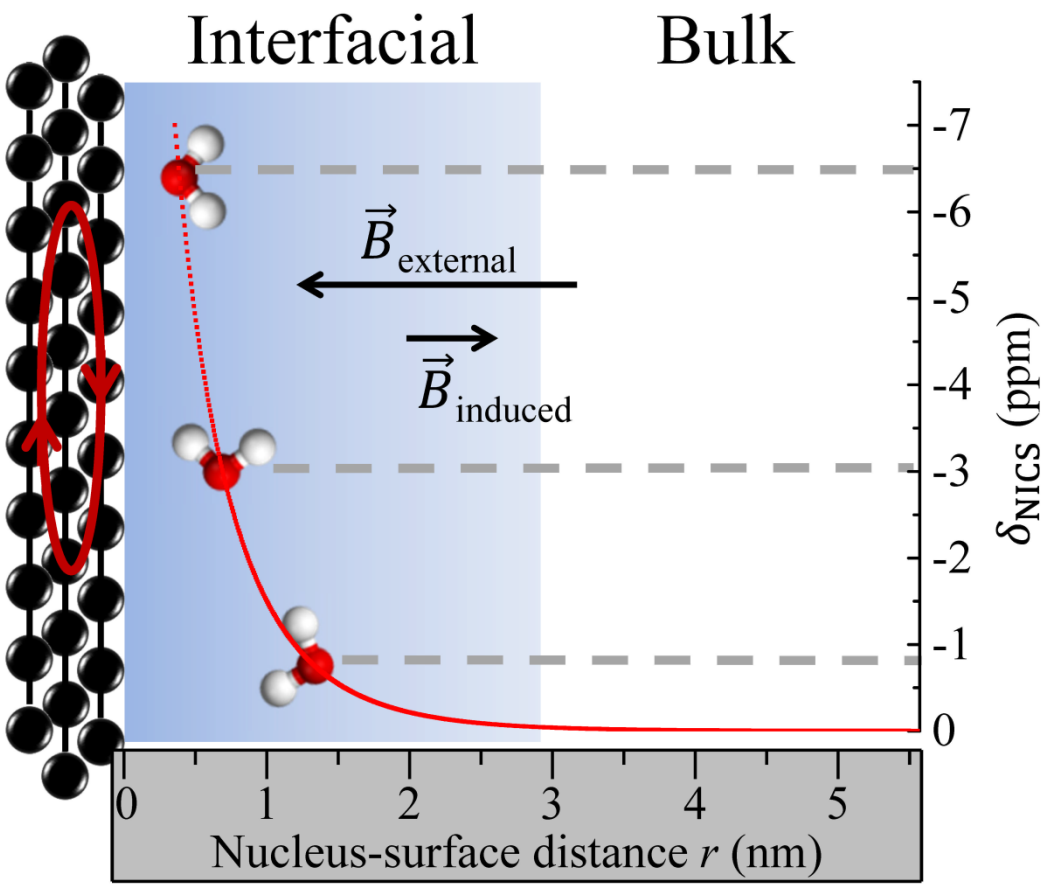

Figure 7.6 Principal of the distance-dependent NICS effect. Interfacial species are subject to a discernible diamagnetic response due to the interatomic ring current at the graphitic carbon surface. The chemical shift difference between bulk and interfacial species, δ_{NICS}, depends only on the distance r between the nuclei and the carbon surface. In the figure, the black spheres are carbon atoms and the red circle represents the induced interatomic ring current on the carbon surface.

7.3.2 NICS of Confined Binary Mixtures

Figure 7.7a demonstrates a binary mixture sandwiched between two planar graphitic surfaces. If the pore width is a few molecular diameters, the confined nuclei would experience a strong NICS effect. Note that in NMR timescale, confined molecules move rapidly inside the micropore and spend time both close to and away from the surface. The measured chemical shift of confined species is δ_{NICS} averaged over the pore space. In the *homogeneous* model, the

confined liquid mixture mixes completely, same as in the bulk. Hence, δ_{NICS} of a homogeneous mixture is independent of concentration: $\delta_{\mathrm{Low}} = \delta_{\mathrm{High}} = \delta_{100\%}$ as shown in Figure 7.7a. A typical example of the homogeneous model is aqueous electrolyte in nanoporous graphitic-like carbon. Figure 7.7b shows ^{1}H, ^{23}Na, and ^{19}F magic angle spinning (MAS) NMR spectra of aqueous $NaBF_4$ electrolytes in 1.6 nm graphitic nanopores. For all the three nuclei (^{1}H, ^{23}Na, and ^{19}F), δ_{NICS} of the 0.01, 0.1 and 1 M aqueous $NaBF_4$ electrolytes are equivalent, following the predictions of the homogeneous model. Conversely, in the *heterogeneous* model, if we assume that solute molecules aggregate in the vicinity of the surface, δ_{NICS} would vary with the solute concentration. At low solute concentrations, the majority of solute molecules are close to the interface, resulting in a more negative δ_{NICS}. While increasing the solute concentration leads to less negative δ_{NICS}. Thus, in the heterogeneous model, $\delta_{\mathrm{Low}} < \delta_{\mathrm{High}} < \delta_{100\%}$, markedly different from the homogeneous model.

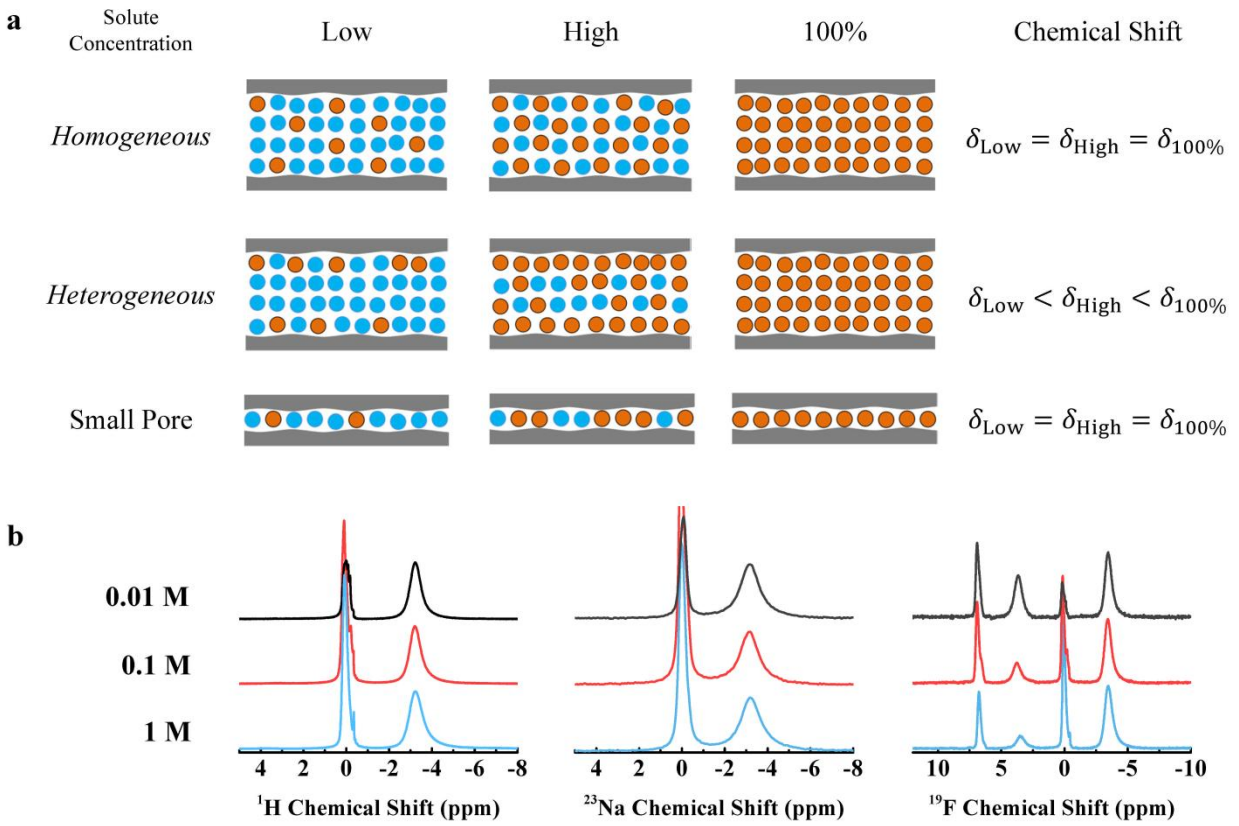

Figure 7.7 Two-dimensional illustrations of binary liquid mixtures between two planar carbon surfaces. (a) Yellow balls represent solute, the blue represents solvent, and thick grey lines are planar graphitic surfaces. δ is the NICS-induced chemical shift of the solute. *Homogeneous model*: the homogeneous model assumes complete mixing, leading to $\delta_{Low} = \delta_{High} = \delta_{100\%}$. *Heterogeneous model*: suppose that the surface has a preferential attraction to the solute. The molecular separation leads to $\delta_{Low} < \delta_{High} < \delta_{100\%}$. However, when the pore size is comparable to the thickness of alcohol monolayer, no demixing would occur because there is not enough space for alcohol and water to layer. Thus, in the *Small Pore* case, $\delta_{Low} = \delta_{High} = \delta_{100\%}$. (b) ^{1}H, ^{23}Na and ^{19}F MAS NMR spectra of aqueous $NaBF_4$ electrolytes in 1.6 nm graphitic nanopores. From top to bottom, the concentration of $NaBF_4$ is 0.01, 0.1 and 1 M, respectively. For all the three nuclei (^{1}H, ^{23}Na, and ^{19}F), δ_{NICS} of 0.01, 0.1 and 1 M aqueous $NaBF_4$ electrolytes are independent of concentration, following the predictions of the *homogeneous* model.

7.3.3 Experimental Characterization of Nanoconfined Methanol-Water Mixtures

To better understand the molecular arrangement of alcohol and water at the graphitic surface, we explore in depth the interface formed by nanoporous graphitic-like carbon and methanol-water mixtures using the distance-dependent NICS effect. The concentration of methanol varies from 5 to 100 wt %, corresponding to molar fractions from 3 to 100 mol %. To avoid the strong ^{1}H signal from H_2O, deuterium oxide (D_2O) is used instead of water (H_2O). The micropore sizes of the three carbon samples are 0.5, 1.0, and 1.6 nm, measured from the carbon atom surface to the carbon atom surface at each interface.

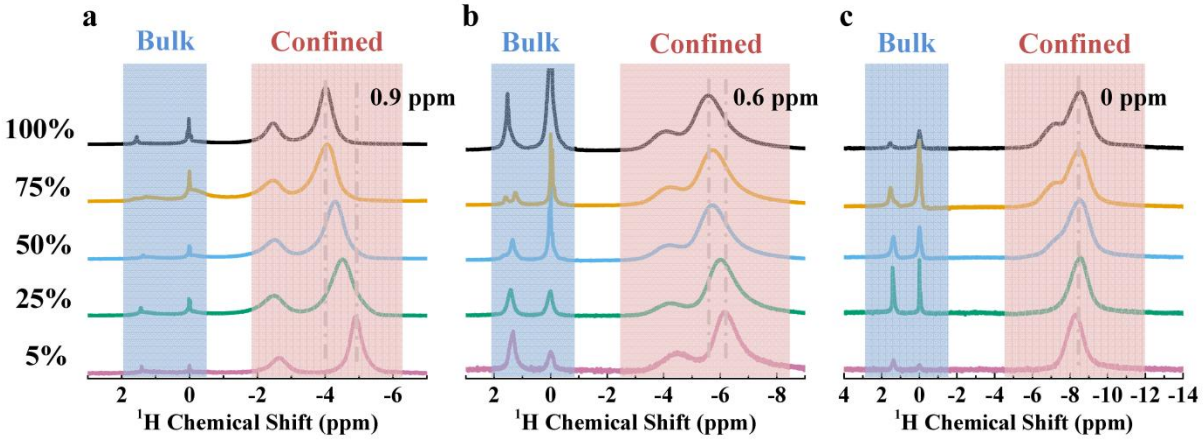

Figure 7.8 Methanol-water mixtures in nanoscale confinement. (a-c) ^{1}H MAS NMR spectra of methanol-water mixtures in nanoporous graphitic-like carbon with (a) 1.6 nm, (b) 1.0 nm, and (c) 0.5 nm micropores, respectively. From top to bottom, the concentration of methanol decreases from 100 to 5%. The bulk CH_3 proton peaks are chosen as the reference (0 ppm).

Figure 7.8a shows ^{1}H MAS NMR spectra of aqueous methanol solutions in the highly ordered microporous carbon with 1.6 nm pores. Each spectrum consists of four peaks which can be classified into two groups: interfacial fluid inside nanometer-sized regions confined by hydrophobic graphitic surfaces and bulk fluid outside the nanopores.(*20, 34, 88, 156*) Take the 100 wt % spectrum for example, from left to right, the four peaks are bulk OH (1.5 ppm) and CH_3 (0 ppm) proton peaks from intergranular spaces, and interfacial OH (-2.5 ppm) and CH_3

(−4.0 ppm) proton peaks from nanopores, respectively. The chemical shifts of bulk species are independent of methanol concentration, which is identical to the water/methanol solutions (Figure 7.9). However, the bulk and interfacial signals behave differently when methanol content changes. Increasing the methanol concentration shifts the interfacial OH and CH_3 signals toward downfield region. The clearly different response to the methanol concentration between the bulk and interfacial species is quite important because it suggests that the dependence of interfacial signals upon methanol concentration is an interface-induced phenomenon rather than a bulk property.(*162, 163*) Compared to the binary liquid mixture model above, it can be concluded that methanol and water forms a homogeneous solution in the intergranular regions, and forms a heterogeneous mixture in the nanopores.

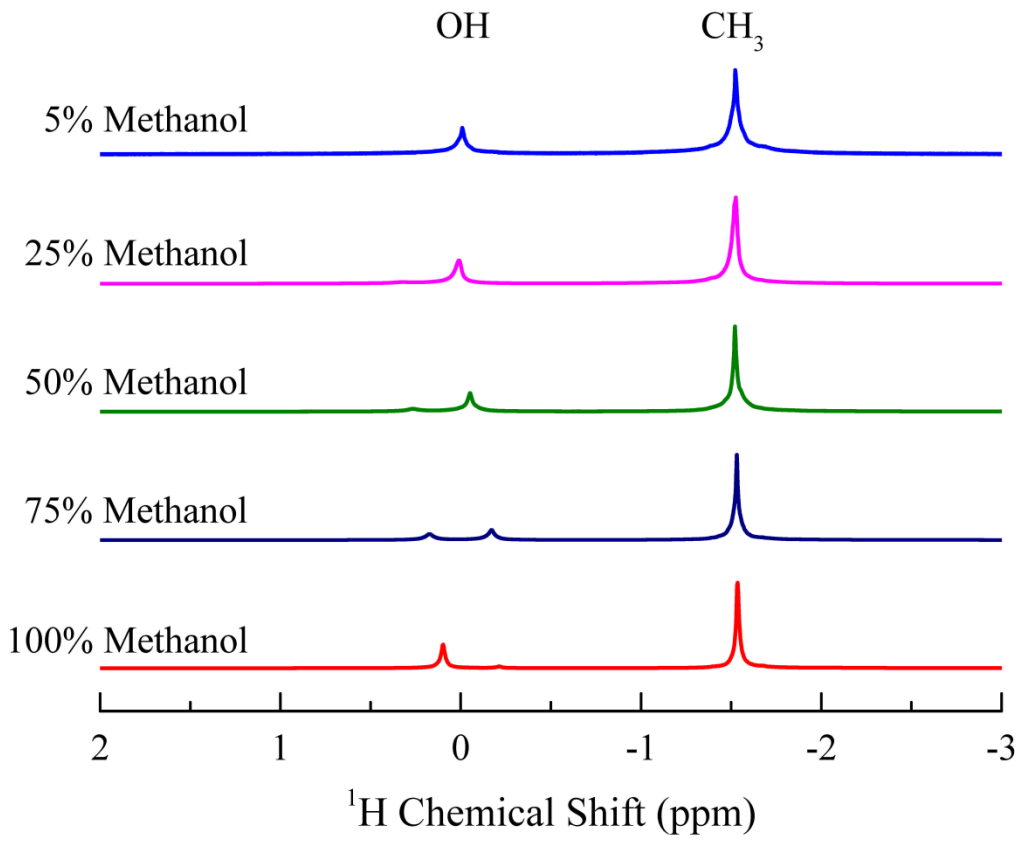

Figure 7.9 ^{1}H NMR spectra of bulk methanol-water mixtures. From top to bottom, the concentration of methanol varies from 5 to 100 wt %. The bulk H_2O proton peaks are chosen as the reference (0 ppm).

Kislon Voitchovsky *et al.* found that in a 1:1 water:methanol mixture (corresponding to 64 wt %), methanol forms a segregation layer above the carbon surface with a distance of 0.35 nm. This agrees well with our observations. It should be noted that MD simulations cannot fully capture the formation of the layered structure due to the slow dynamics and glassy behavior of the solutions above the hydrophobic interface. To verify that this molecular separation behavior is stable, we repeated the same tests after a 2-day interval. No obvious changes in NMR spectra were observed, proving that the layered structure above the hydrophobic interface is stable in room ambient conditions (Figure 7.10). Moreover, we find that the methanol clustering layer is largely dependent on methanol concentration. The dependence on methanol concentration

indicates that a picture in which all alcohol molecules adsorbed at the surfaces and water molecules are in the pore center is an over-simplification. Rather than forming a clear boundary between methanol and water, the molecular separation leads to a local concentration gradient normal to the pore surface although the overall composition averaged over a system is fixed. Kislon Voitchovsky *et al.* shows that the concentration of water in the first layer is comparable to its bulk counterpart, yet the methanol concentration in the first layer is three times greater than its bulk counterpart.(*152*) Moreover, outside of the carbon/alcohol-water interface, Mathieu Salanne *et al.* also observed a similar distribution of ionic liquids at the planar graphite and carbide-derived carbon (CDC) surfaces, suggesting that the surface segregation is a general feature of organic compounds at hydrophobic interfaces.(*164*)

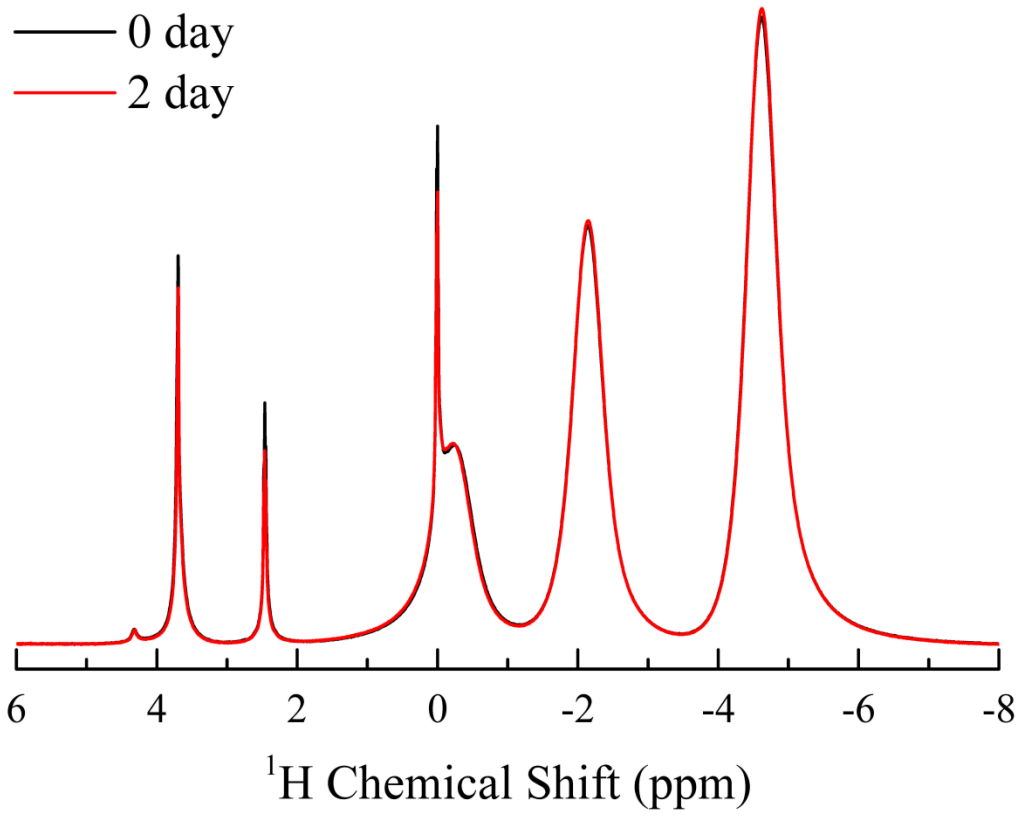

Figure 7.10 Stability of the demixing phenomenon. ^{1}H NMR spectra of 50 wt % ethanol-water mixtures in the 1.6 nm carbon samples. The black curve was obtained first and the red curve was

acquired two days later. The black and red curves overlap with each other very well, demonstrating the demixing behavior is stable. The bulk CH_3 was chosen as the reference (0 ppm).

7.3.4 Pore-Size Dependent Demixing under Nanoconfinement

Similar ^{1}H NMR spectrum is observed for methanol-water mixtures inside the 1.0 nm nanopores. As the pore size is further reduced to 0.5 nm, in Figure 7.8c, δ_{NICS} of nanoconfined methanol is independent of the methanol concentration and equals -8.5 ppm, which disagrees with the heterogeneous model. However, this does not indicate that there is no methanol-water separation in the 0.5 nm nanopores; instead, as illustrated in Figure 7.7a, in small pores, e.g. 0.5 nm, only monolayer or few-layer coverage is possible. This coverage prevents molecular separation perpendicular to the wall surface, but separation along the pore direction is possible, which is similar to the demixing observed in confined alcohol-water films using AFM.(*4*, *142*, *143*)

7.3.5 Ethanol-Water Mixtures at Graphitic Surface

While the discussion thus far has been centered on methanol, a systematic study of various miscible alcohols, including ethanol, 2-propanol, *tert*-butanol, and TFE, has been undertaken to fully understand the demixing phenomenon. Figure 7.11a displays ^{1}H MAS NMR spectra of aqueous ethanol in nanoporous carbon with 1.6 nm micropores. The situation qualitatively looks like the concentration profiles of methanol in Figure 7.8. The six peaks in each plot are, e.g. 100 wt %, from left to right, bulk OH (4.1 ppm), CH_2 (2.4 ppm) and CH_3 (0 ppm) protons and interfacial OH (-0.1 ppm), CH_2 (-1.8 ppm) and CH_3 (-4.2 ppm) protons, respectively. Additionally, when the ethanol concentration increases, both interfacial CH_2 and CH_3 proton peaks shift to less negative values, suggesting a molecular separation of ethanol and

water at the interface as well. In spite of these common characteristics, two new features are observed.

First, interfacial CH_2 proton peaks have the same shape as the CH_3 proton peaks, and δ_{NICS} of CH_2 and CH_3 protons are equal to each other across all the concentrations. For example, at 5% ethanol, both interfacial CH_2 and CH_3 protons shift -5.7 ppm when compared with their bulk counterparts. Additionally, in Figure 7.11b, the density profiles of CH_2 (dash line) and CH_3 protons (solid line) overlap with each other, demonstrating that the CH_2 and CH_3 group remain equidistance from the carbon surface at all concentrations. Therefore, it can be concluded that the ethyl group is parallel to the surface, consistent with previous DFT simulations.(*146, 165*) Second, compared to aqueous methanol solutions in 1.6 nm micropores, at the same content, δ_{NICS} of ethanol is always more negative than methanol, suggesting that ethanol is closer to the surface than methanol. For example, at 5% concentration, δ_{NICS} of ethanol is -5.6 ppm and r is 0.23 nm, while δ_{NICS} of methanol is -4.9 ppm and r is 0.29 nm. Furthermore, the δ_{NICS} change between 5% and 100% solution of ethanol is greater than methanol as well.

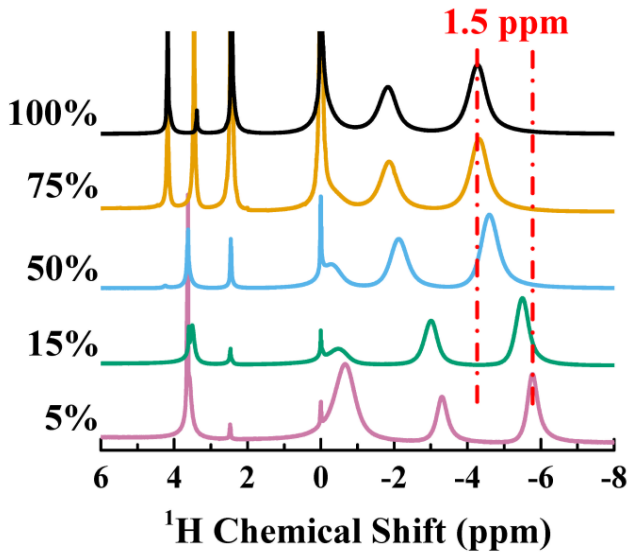

Figure 7.11 ^{1}H MAS NMR spectra of ethanol-water solutions in the nanoporous carbon with 1.6 nm micropores. The bulk CH_3 proton peaks are chosen as the reference (0 ppm). The six peaks observed in each plot are, from left to right, bulk OH, CH_2 and CH_3 protons and interfacial OH, CH_2 and CH_3 protons, respectively.

7.3.6 Effect of Hydrophobicity of Alcohol Molecules on Phase Separation

Aside from methanol and ethanol, similar ^{1}H NMR spectra are obtained for other aqueous alcohols in nanoporous carbon, which indicates that the observed phase separation of alcohol and water at graphitic surface is a common phenomenon. Despite the common features, a significant difference in the degree of separation is observed among those miscible alcohols. To study this, the differences in the δ_{NICS} of alcohol at 5% and 100% alcohol content are chosen as a characteristic parameter. This produces $\Delta\delta_{\mathrm{NICS}} = \delta_{\mathrm{NICS}}^{100\%} - \delta_{\mathrm{NICS}}^{5\%}$ values in Figure 7.12a. We must mention that 5% is not an arbitrary choice. It is found that δ_{NICS} remains constant as alcohol content is lower than 5% because almost all alcohol molecules are adsorbed in vicinity of the interface in low concentrations. For example, in Figure 7.13, δ_{NICS} of 5% and 1% methanol-water mixtures in the 1.6 nm carbon sample are same. We chose 5% to be the characteristic

concentration because it can give us a good signal-to-noise ratio and could reduce the systematic error arising from the solution preparation as well.

Figure 7.12a plots $\Delta\delta_{\mathrm{NICS}}$ versus the micropore size of carbon samples. The three points for each alcohol, from left to right, are for 0.5 nm, 1.0 nm, and 1.6 nm micropores, respectively. It is evident that as the number of alcohol's carbon atoms (N_{carbon}) increases, the corresponding aqueous alcohol solution experiences a larger change in δ_{NICS}, suggesting a greater degree of phase separation. It is noted that at 100% concentration, δ_{NICS} for all miscible alcohols are nearly the same, about 4.1 ppm. Hence, the variation in $\Delta\delta_{\mathrm{NICS}}$ is caused by the range of values observed for the 5% alcohol solutions. In the 100% solution case, the alcohol is modeled to be spread fairly evenly throughout the pore. Thus, at the 5% level, smaller alcohols (e.g. methanol) must be more spread out than larger alcohols (e.g. *tert*-butanol). In other words, in order to show a larger $\Delta\delta_{\mathrm{NICS}}$ *tert*-butanol molecules would need to adhere, on average, much closer to the pore walls in comparison to the methanol.

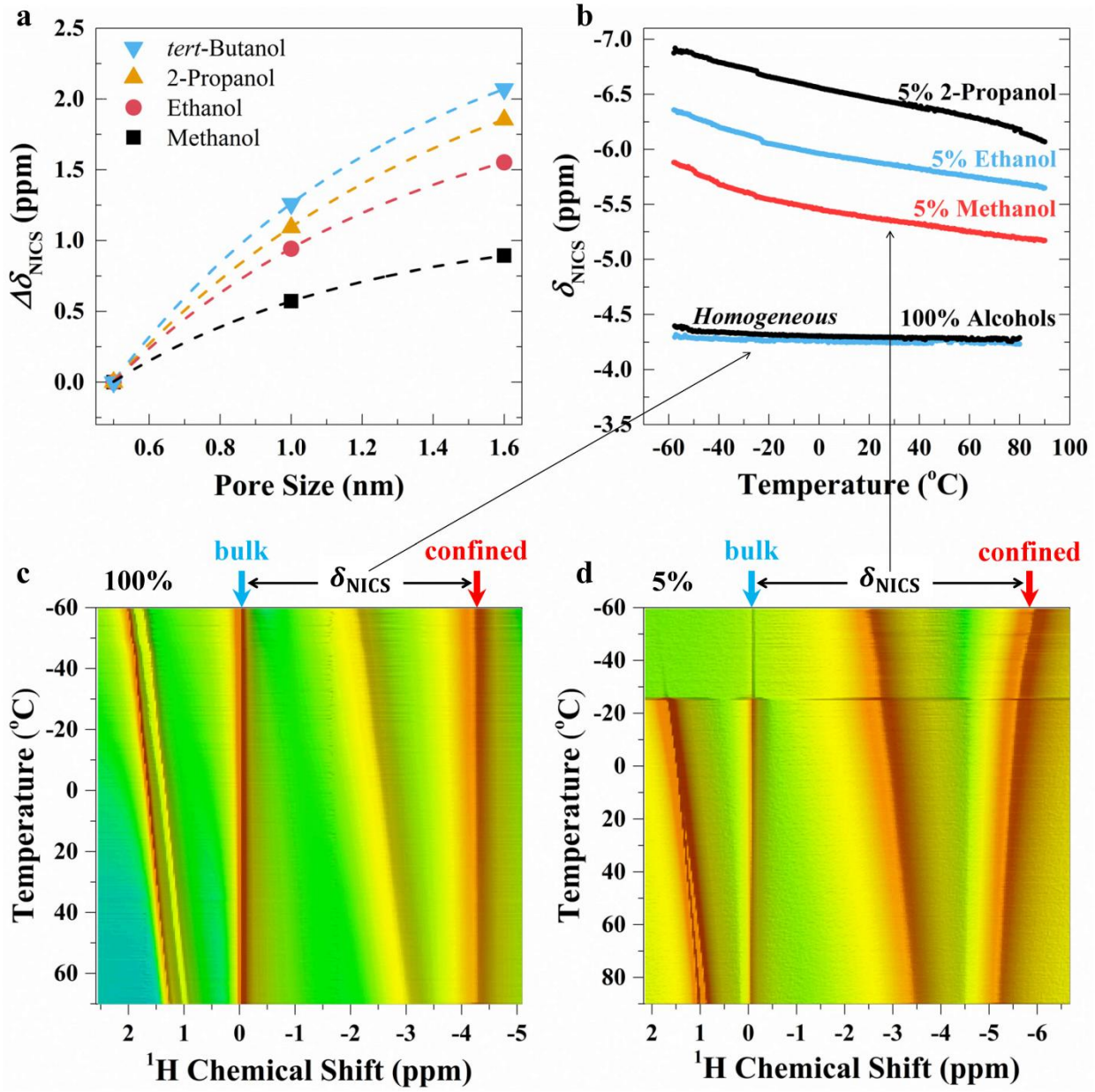

Figure 7.12 Micropore size and temperature dependence of nanoconfined alcohol-water mixtures. (a) $\Delta\delta_{NICS}$ versus the micropore size of carbon samples. The three points for each alcohol, from left to right, are for 0.5 nm, 1.0 nm, and 1.6 nm micropores, respectively. The dashed line simply serves as a guide for the eye. (b) Variable-temperature δ_{NICS} data for nanoconfined aqueous alcohols. (c,d) Image plots of ^{1}H NMR spectra of 100% methanol (c) and 5% methanol (d) solutions during the continuous cooling process. The horizontal axis represents

the selected chemical shift regions, and temperature is on the vertical axis. Blue arrows: reference bulk CH_3. Red arrows: nanoconfined CH_3.

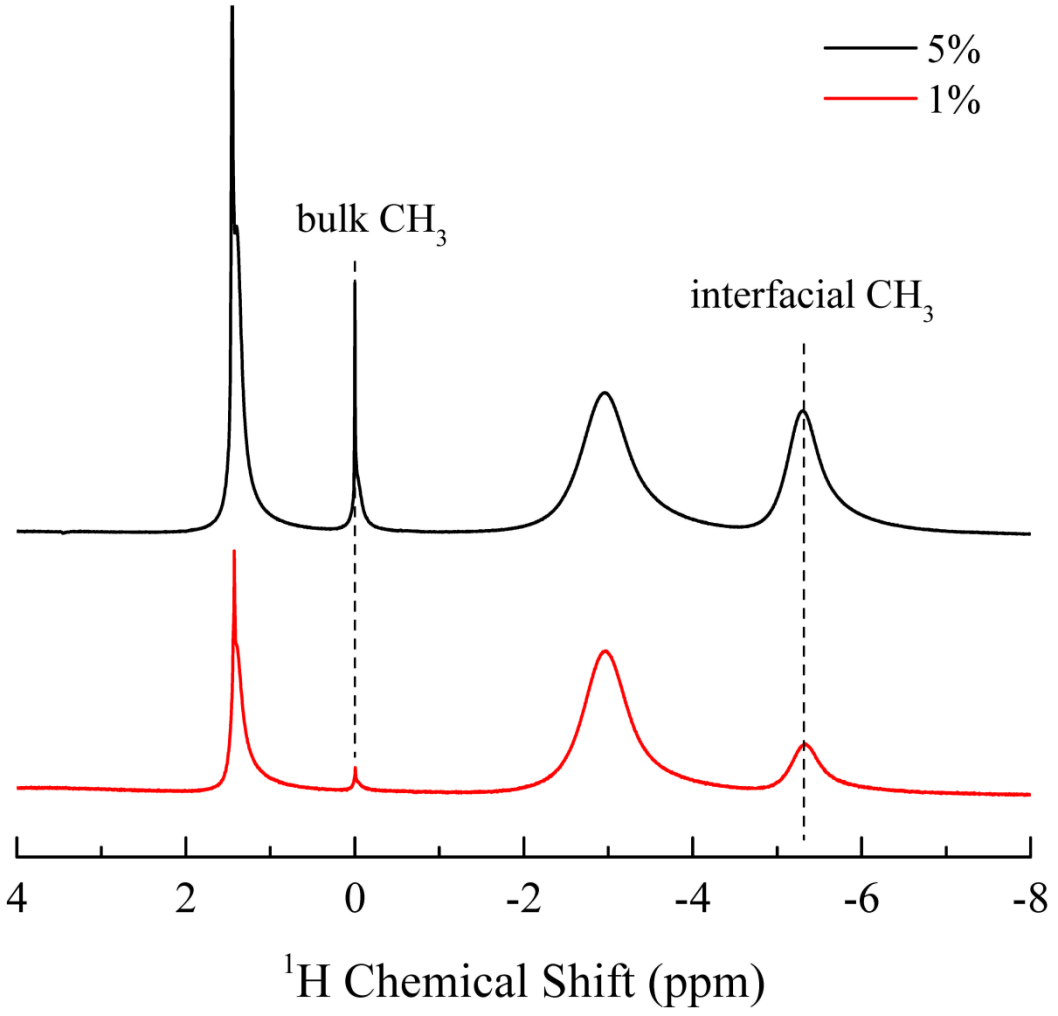

Figure 7.13 ^{1}H NMR spectra of 5% and 1% methanol-water mixtures in the 1.6 nm carbon samples. The concentrations of red and black are 1 and 5 wt %, respectively. δ_{NICS} of the two solutions are equal, suggesting that below 5 wt % δ_{NICS} remains constant because almost all alcohol molecules have aggregated above the interface.

7.3.7 Demixing of Nanoconfined Aqueous Alcohols at High Temperatures

At high temperatures, where the free energy of mixing is dominated by the entropic component, multicomponent system tends to mix to gain higher entropy. If true for nanoconfined

mixtures, this, in turn, suggests that $\delta_{\text{Low}} = \delta_{\text{High}} = \delta_{100\%}$ at high temperatures. To determine the phase diagram of nanoconfined aqueous alcohols, in situ ^{1}H NMR spectra were recorded when alcohol-water mixtures are cooled from 90 ℃ to -60 ℃ at a rate of 1 ℃/min. Figure 7.12b plots δ_{NICS} of nanoconfined alcohols versus the temperature. Figure 7.12c and d show image plots of ^{1}H NMR spectra of 100 and 5% methanol-water mixtures during the continuous cooling process, respectively. In the 100% solution case, the confined fluids are modeled to spread fairly evenly throughout the pore. Thus, δ_{NICS} of 100% alcohols, including methanol, ethanol, and 2-propanol, overlap with each other. Additionally, δ_{NICS} of 100% alcohols are also nearly independent of temperature (~ -4.25 ppm). Unexpectedly, up to 90 ℃, δ_{NICS} of 5% alcohols, including methanol, ethanol, and 2-propanol, deviates considerably from 100% alcohols, indicating that nanoconfined alcohol-water mixtures still undergo phase separation. Moreover, this also suggests that the critical temperature T_c would be much higher than 90 ℃ if it exists. This is in contrast to the previous report that T_c is around -30 ℃.(*166*)

7.3.8 Driving Forces for Demixing under Nanoscale Confinement

The tendency for the phase separation of binary mixtures depends on free energy. The demixing of nanoconfined alcohol-water mixtures is opposed by the entropy, small alcohols and water tend to mix to gain translational entropy. On the other hand, the phase separation is favored by the enthalpy; that is, if alcohol molecules neighbor the graphitic surface, the system has lower energy than if alcohol molecules neighbor water molecules. The energy reduction by demixing is caused by two factors: (*i*) attractive interactions between alcohols and graphite; (*ii*) favorable hydration of alcohols at the hydrophobic interfaces. The three factors are analyzed below.

First, the entropy increase of mixing water with amphiphilic molecules (e.g. alcohols) is far less than expected for an ideal solution.(*162, 163, 167*) This anomalous small entropy gain of mixing, in turn, suggests that the entropy tradeoff for alcohol-water demixing is much smaller than generally believed. Consider first methanol-water mixtures. The mixing entropy of an ideal solution is given by $S_{\mathrm{id}} = -kN\sum x_j \ln x_j$, where x_j is the mole fraction of each component. Thus, at 298 K, TS_{id} is 0.49 kJ/mol for 5 mol% methanol in water, and 1.72 kJ/mol for 50 mol% methanol in water. While the corresponding experimental entropy TS_{exp} is 0.09 kJ/mol for 5 mol% methanol in water, and 0.66 kJ/mol for 50 mol% methanol in water; both are significantly less than their ideal values.(*168*) For other aqueous alcohol solutions (i.e., ethanol-water and 2-propanol-water), their real mixing entropies are also fairly reduced compared to corresponding ideal values; for example, at 298 K, TS_{exp} is 0.59 kJ/mol for 50 mol% ethanol in water, and 0.80 kJ/mol for 50 mol% 2-propanol in water. This phenomenon, small entropy of mixing, results in a favorable driving force for the demixing of water and lower alcohols.

Second, attractions between alcohols and graphite tend to bring alcohol molecules into contact with the pore surface. The resultant close proximity of alcohols to the carbon surface decreases the energy of the system. The energy reduction, which reflects the work required to transfer an alcohol molecule from infinity to the surface, can be determined through adsorption isotherm measurements. Four single-component adsorption isotherms are shown in Figure 7.14 together with a binary-component adsorption isotherm. The alcohol adsorption isotherms have a concave shape with respect to the P/P_0 axis; while the water adsorption curve is S-shaped, indicating that graphite 'likes' alcohols than water. More insight can be gained by analyzing isotherms with Dubinin-Astakhov (D-A) equation, which characterizes the strength of interaction

between the adsorbent and adsorbate molecules residing within the micropores.(*169*) The D-A adsorption isotherm equation is

$$\theta = \exp\left\{-\left[\frac{RT}{E}\ln\left(\frac{P_0}{P}\right)\right]^m\right\} \tag{7.2}$$

where P is the absolute pressure, P_0 is the saturation vapor pressure, θ is the fraction of complete pore filling, E is the characteristic interaction energy between adsorbate and adsorbent, R is the gas constant, T is the temperature, and m is the fit parameter that is considered to be a measure of the heterogeneity of the porous materials. The fitted isotherms (solid lines) are shown in Figure 7.14 with fitting parameters listed in Table 7.1. Here, the affinity between alcohol and graphite (4~6 kJ/mol) is about six times of that of water and carbon (0.73 kJ/mol). In addition, the interaction strengths between adsorbate and adsorbent follow the trend water < methanol < ethanol < 2-propanol, consistent with our observation that larger alcohols experience stronger phase separation than smaller alcohols. Both of these observations confirm that the attraction between alcohol and graphite is the crucial factor in the nanoconfined phase separation.

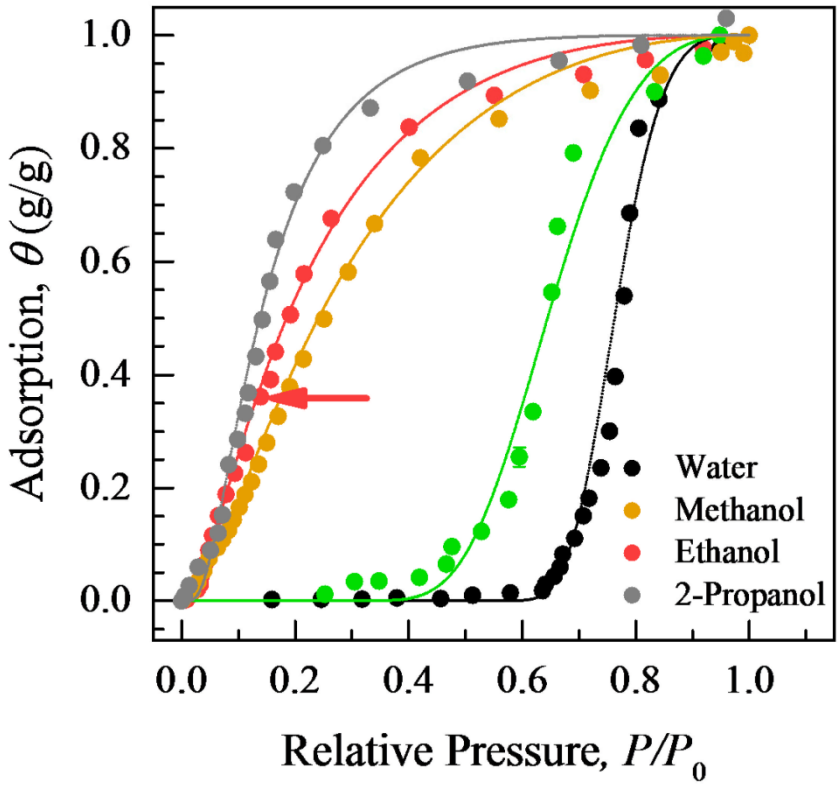

Figure 7.14 Normalized adsorption θ of alcohols or water on the nanoporous carbon with 1.6 nm micropores at 293 K. Green dots are the water adsorption isotherm in presence of the preadsorbed ethanol on the carbon sample. Isotherms are fitted to the D-A model (solid lines, fitting parameters shown in Table 7.1) for comparison purposes. At each pressure, the NMR signal is measured 5 times after reaching equilibrium, and then the standard deviations of NMR peak areas are used to calibrate the error bars in the isotherms.

Table 7.1 Dubinin-Astakhov adsorption isotherm parameters.a

	n_0/g g^{-1}	E/kJ mol^{-1}	m
Water	1.50	0.73	3.65
Methanol	1.08	4.2	1.90
Ethanol	1.31	4.8	2.14
2-propanol	1.25	5.4	3.20

Water in presence of ethanol	0.68	1.2	2.80

[a]n_0 is the maximum adsorption amount and is obtained from the isotherm experimental data. *E* and *m* are parameters to fit the adsorption isotherms.

The lower solvation free energy of alcohols at the interface than that in the bulk water also favors the demixing of alcohols and water. The free energy for solvating small alcohols either in the bulk water or at the interface can be approximated by considering the free-energy contributions of the hydrophobic head (alkyl groups) and ignore the contributions of hydroxyl group: because the hydroxyl is always in the aqueous environment. Patel et al. studied the size dependence of cavity hydration in the water and at hydrophobic interfaces.(*170*) MD simulation shows that, at 300 K, for a cuboidal cavity ($0.8\times0.8\times0.3$ nm^3), as would be appropriate for small alcohols, the solvation free energy difference between the interface and bulk $\Delta G_{\text{solvation}}$ is about -4.4 kJ/mol. Furthermore, $\Delta G_{\text{solvation}}$ become more favorable as the size of the cavity increases, consistent with our observation that larger alcohols cluster closer to the interface. Patel et al. also predicts that for small cavities with a length of ~ 0.75 nm, $\Delta G_{\text{solvation}}$ becomes more favorable with increasing temperature; for a cavity ($0.5\times0.5\times0.3$ nm^3), $\Delta G_{\text{solvation}} = -2.75$ kJ/mol at 300 K, while $\Delta G_{\text{solvation}} = -4.95$ kJ/mol at 320 K. This thermodynamics signature could explain the observed stable separation structure at high temperatures.

Taking account all these three factors, we find that the intrinsic microimmisibility of alcohols and water is crucial for the demixing of nanoconfined water and small alcohols. Take 5 mol % methanol-water solutions for example. The change in enthalpy on demixing is -0.43 kJ/mol: -0.21 kJ/mol from surface attraction and -0.22 kJ/mol from surface solvation. This

enthalpy change on demixing is greater than the entropic penalty for the real methanol-water solution, 0.09 kJ/mol, however, is smaller than 0.49 kJ/mol for an ideal solution, indicating that the separation cannot happen according to the ideal solution model. Thus, our data validate the molecular segregation observed in a concentrated alcohol-water solution.(*163*)

7.3.9 Microscopic Separation Alters Macroscopic Properties

The microscopic separation of alcohol and water at the hydrophobic interface is of great industrial interest, for example, it demonstrates that graphene membrane is a potential candidate for the separation of alcohol and water. In this study, we show that the assembly of alcohol molecules at the pore surface tunes the wetting behavior of the surface from hydrophobic to hydrophilic, which is confirmed by the binary-component isotherm and contact angle measurements.

The adsorption of water on microporous carbon with preadsorbed ethanol is shown in Figure 7.14 (green dots). Compared to the water adsorption on the pristine nanoporous carbon (black dots), the preadsorbed ethanol increases the water adsorption capacity at low relative pressures ($0.2 < P/P_0 < 0.45$), indicating that the surface becomes more hydrophilic. The interaction between water and graphite is also increased from 0.73 kJ/mol to 1.2 kJ/mol. The enhanced hydrophilicity of the surface is also proved by simulations showing that the hydrophobic alkyl groups of the preadsorbed ethanol molecules point toward the carbon surface, while the hydrophilic OH groups act as additional adsorption sites for water to nucleate on the surface.(*146, 149, 150*)

Moreover, the demixing of alcohol and water at the hydrophobic interface results in different surface wettability. The macroscopic contact angles of water, ethanol and ethanol-water

mixtures on a hydrophobic surface have been measured. Here, the hydrophobic surface is a glass surface coated with chloro(dodecyl)dimethylsilane. The exposed alkyl tails of the silane make the glass surface more hydrophobic, exhibiting similar hydrophobicity as with graphite.(*171, 172*) Shown in Figure 7.15, the contact angle of the water droplet for this system is $96 \pm 2^{\circ}$, whereas for ethanol it is $13 \pm 2^{\circ}$. The contact angle decreases especially quickly when the ethanol concentration increases from 0% to 20%. This drastic reduction of the contact angle refers to the molecular separation of ethanol and water at the hydrophobic surface; that is, ethanol molecules diffuse to the solid-liquid interface, tuning the wetting behavior of the surface from hydrophobic to hydrophilic in nature. (*140*)

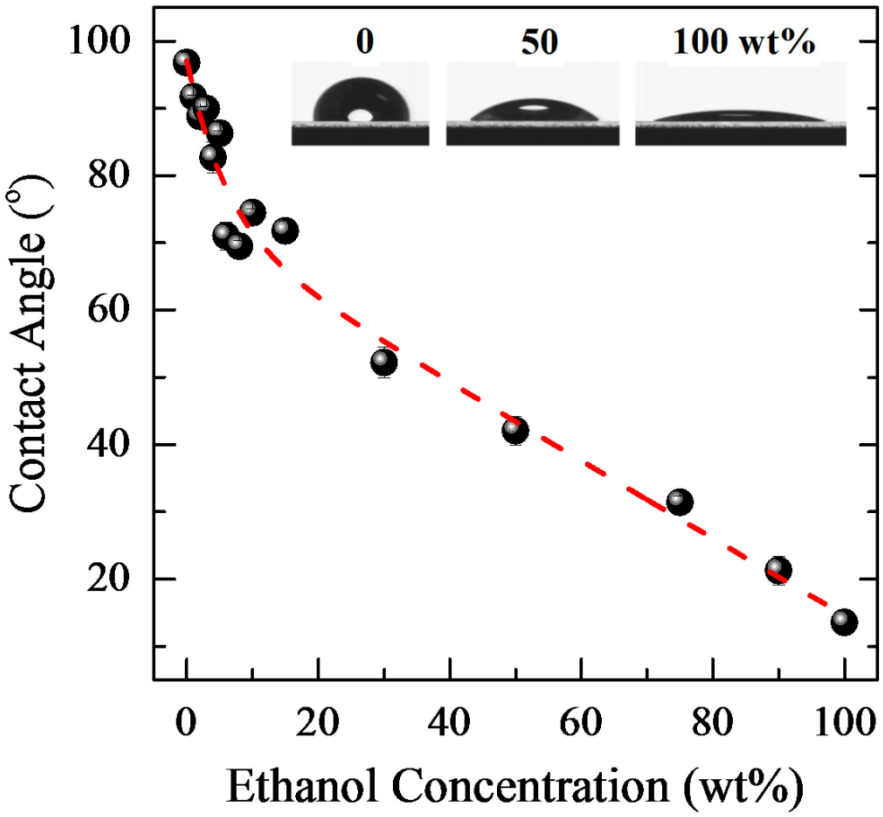

Figure 7.15 Contact angle data on chloro(dodecyl)dimethylsilane coated glass wafers. Inset: images of aqueous ethanol drops on glass wafers. From left to right, the concentrations of ethanol are 0, 50 and 100%. The dashed line simply serves as a guide for the eye.

7.4 Summary and Outlook

In this work, we provide a feasible method to study the nanoconfined fluids based on a distance-dependent magnetic resonance effect. We find that aqueous alcohol solutions undergo phase separation inside the hydrophobic graphitic nanopores. The segregated state remains stable up to 90 ℃, suggesting an unexpectedly high T_c. Detailed phase diagram of nanoconfined mixtures could be mapped either by using better high-temperature NMR equipment or by simulations. Since this technique is independent of crystal structure, it thus can be applied to various carbonaceous materials such as metal-organic frameworks (MOFs) and graphene membranes.(*126, 173*) Also, we show that the interaction between fluid and confining wall can

be tuned, e.g., by altering the hydrophobicity of molecules and by coating the pore surface with certain surfactants. Besides controlling the surface wetting property demonstrated in this paper, the phase behavior of nanoconfined fluids dramatically influences the properties of nanoscopic devices. For example, Simon Gravelle *et at*. reports that carbon membranes exhibit a counter-intuitive "self-semi-permeability" to water in the presence of water-ethanol mixtures while they are permeable to both pure liquids.(*147*)

CHAPTER 8 HYDROPHILIC AND HYDROPHOBIC CHARACTERISTICS OF RESERVOIR ROCKS QUANTIFIED BY NMR-DETECTED WATER ISOTHERMS

8.1 Context and Scope

Reservoir wettability, specifically the wettability of the porous structure within rocks, is one of the parameters that determine the fluid flow through those rocks.(*174, 175*) It is therefore a critical input variable for geophysical models that predict multiphase flow through rocks, assess reservoir quality, and predict well producibility.(*176*) Wettability is often used as a distinguishing characteristic of materials, designating them as either hydrophobic (water fearing), or hydrophilic (water loving). However, wettability is not just a material parameter characteristic of a given type of rock, e.g. sandstone or carbonate, but depends on detailed characteristics, such as mineral types, surface roughness, pore sizes, *etc*.(*177*) Consequently, it is not sufficient to determine the wettability of a reservoir rock by using a water drop and measuring the contact angle, which only identifies the wetting behavior of a specific surface, i.e., the behavior of the fluid in the entire pore space is not assessed. Rock wettability as a useful input parameter for formation models needs to be determined by phenomena spanning the complete pore network and under conditions that resemble and mimic rock environments.

Natural rocks have complex structures, often comprising a variety of mineral types and a wide range of pore sizes, which has been confirmed by SEM imaging. (See Figure 8.1) Because the wettability needs to be determined within the rock pore structure, macroscopic characterization techniques, i.e., contact angle determination, are of limited value. Other common wettability measurement methods for porous media, such as Amott-Harvey test and

United States Bureau of Mines (USBM) method are indirect methods, which are prone to a considerable margin of errors from the unavoidable multiple experimental procedures.(*178, 179*) In addition, these methods have no validity as an absolute measurement, but are the industry standard method for comparing the wettability of various core plugs.

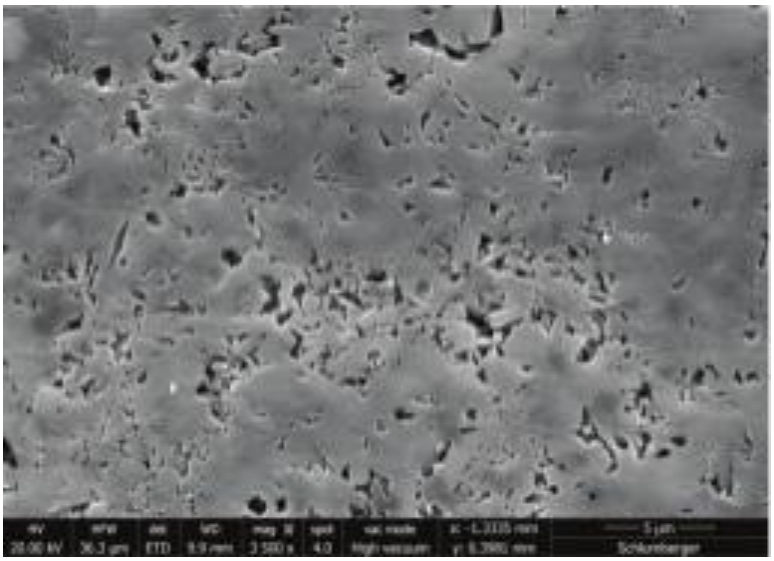

Figure 8.1 Argon-ion milled sample of a fossiliferous, calcareous mudstone from an unconventional formation. The image focuses on an organic matter pellet within the mudstone that is rich in calcareous fossils. The skeletal structures of these fossils provide a framework that preserves high porosities within the rock. (Source: Image courtesy of Schlumberger)

8.1.1 NMR's Unique Capabilities to Elucidate Wettability within Porous Material

NMR adsorption isotherm technique has proven to be a good technique to evaluate the wettability within porous structures.(*180*) More importantly, NMR is a nondestructive method that can investigate porous materials in their pristine state with minimal interference, and in many cases, experiments can be performed in situ. For example, in Figure 8.2, based on NMR adsorption isotherm, Wang *et al.* shows that the shape of water adsorption isotherms in micropore environments strongly depends on the surface hydrophobicity; hydrophobic surfaces produce a concave shape, while hydrophilic surfaces lead to a convex isotherm, corresponding to

Type III and Type I and II, respectively, of the IUPAC classification of isotherms.(*86*) In addition to the isotherms, NMR can also provide insight into the molecular dynamics at the interface by probing the relaxation processes (T_1, T_2).(*88, 90, 181, 182*)

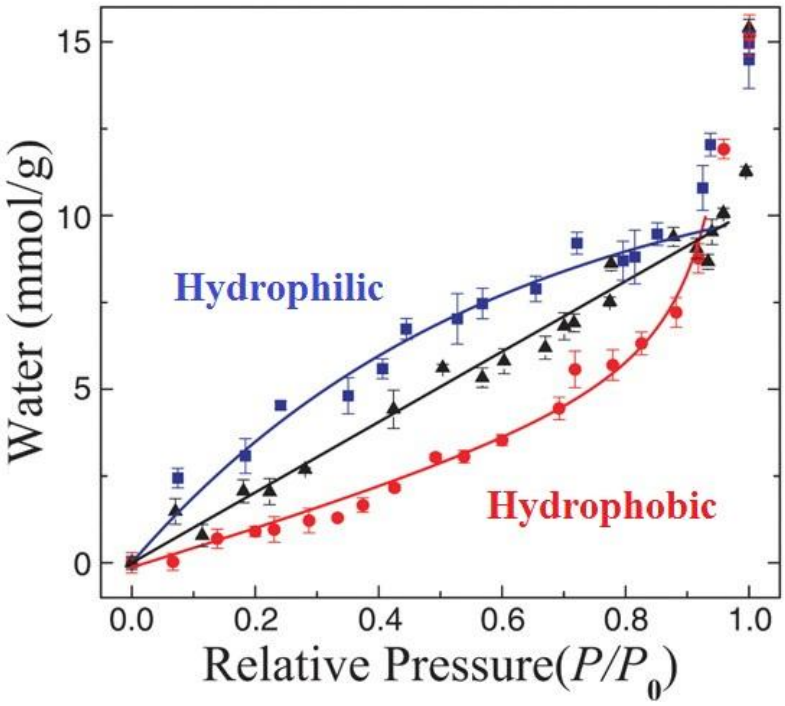

Figure 8.2 Water adsorption isotherms. Three isotherms at 8.0 ℃ (squares), 18.4 ℃ (triangles), and 22.1 ℃ (circles) are shown (The uncertainty of T is ± 0.3 ℃). The lines are guides to the eye. The vertical error bars are shown when they are larger than the size of the symbols and the pressure uncertainty is less than 1% of P_0.(*86*)

8.1.2 Experimental Setup of NMR Isotherm Technique

The gas adsorption isotherms are measured using a vapor delivery system that allows accurate control of vapor pressure and temperature (Figure 8.3). The in situ NMR isotherm system enables us to selectively detect the adsorbent on the surface with high sensitivity subjected to a controlled vapor pressure. As illustrated in Figure 8.3a, the basic components are a vacuum chamber connected to a mechanical pump, a pressure gauge, the NMR sample tube, and the source of water vapor. In each measurement, the dry sample is first packed into the sample

tube (Figure 8.3b). The ^{1}H free-induction-decay (FID) signal of the dry sample is then measured by a single-pulse excitation with a pulse duration of 8 μs. The waiting interval between each repetition of the pulse sequence is set long enough to ensure that the signal is fully recovered after each scan. A broad peak of 500 ppm (full width at half-maximum, FWHM) is observed in the background spectrum and is subtracted from subsequent spectra. Water vapor is then loaded to the sample at varying vapor pressures, and the NMR spectra of the hydrated sample are acquired as a function of water vapor pressure. The intensity of the ^{1}H NMR signal is calibrated with a test tube of bulk water of known mass.

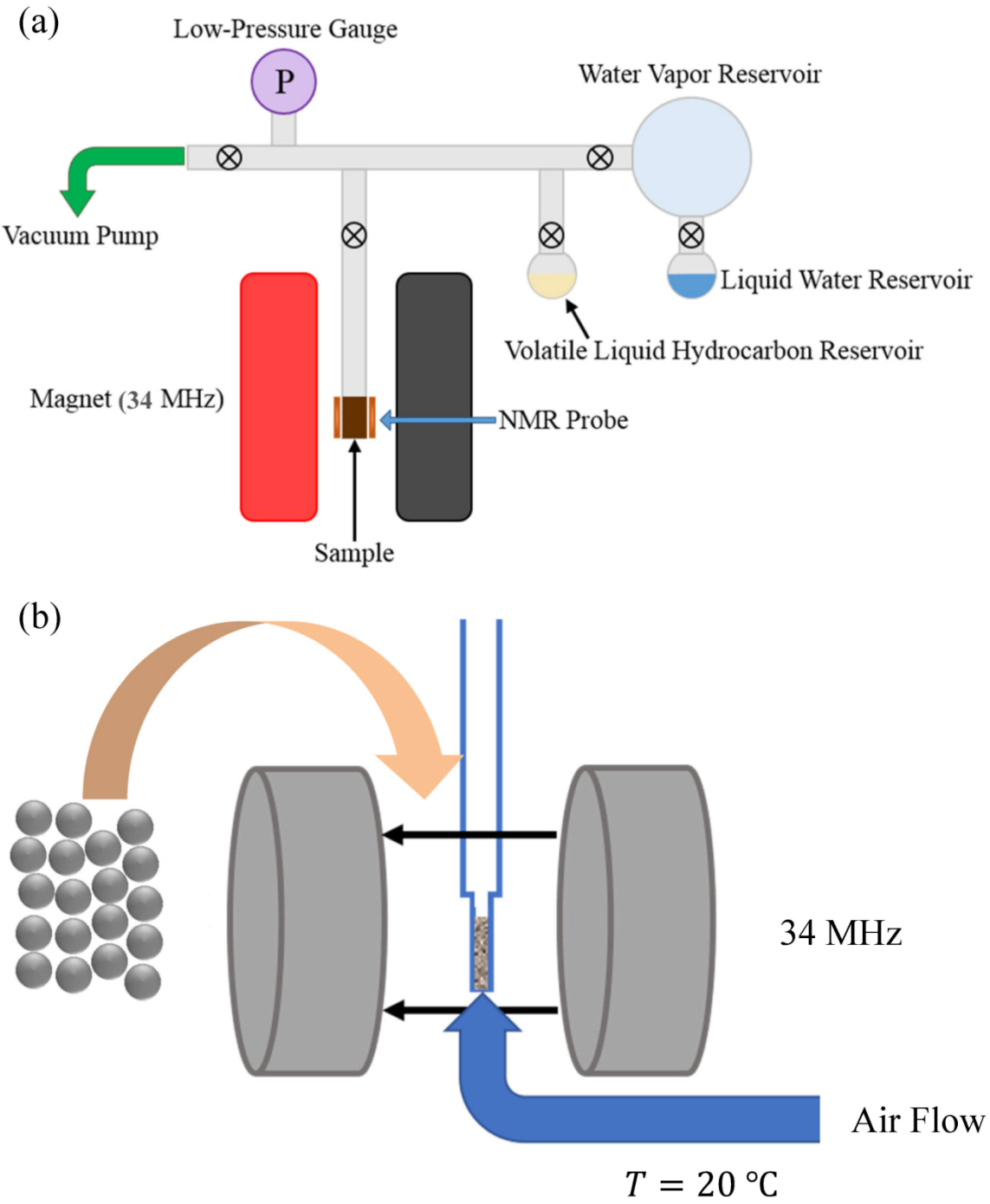

Figure 8.3 (a) The 34 MHz magnet and water vapor delivery system with vapor expansion bulb, distribution chamber, pressure gauge, pump connection, and sample tube. (b) Dry samples (left), treated glass beads or rocks, are first loaded into the sample tube. The sample tube is subsequently attached to the vapor delivery system and maintained at 293 K by airflow.

In this work, we apply in situ NMR isotherm technique to quantify the hydrophilic and hydrophobic characteristics of reservoir rocks. We will first describe the essential concept of our NMR methodology, demonstrating its utility using glass beads phantoms, and then apply it to natural reservoir rocks. The analysis of soda lime glass beads with different wetting properties proves that our approach is indeed capable of distinguishing between hydrophobic and hydrophilic surface states, which are directly related to the wettability. The correlation between the amount of water adsorbed and the properties of surface is also discussed. The new NMR method is further applied to study reservoir core rocks. Both the amount of water adsorption and the shape of isotherm provide valuable information on rock surface wettability and porosity, leading to new insights that are needed in optimizing hydrocarbon production.

8.2 Experimental Details

8.2.1 Materials

The soda lime glass beads are purchased from Mo-Sci Corporation and used as purchased without further purification. The soda lime glass beads are spherical and nonporous. Three different soda lime glass beads are used: 20, 40, and 400 μm in diameter, respectively. Sulfuric acid solution (4N), soda-lime glass slides, and chloro(dodecyl)dimethylsilane (purity > 95%) are purchased from Fisher Scientific.

8.2.2 Surface Wettability Modification

The surface wettability of glass beads and glass slides are modified by different chemical treatments. Hydrophilic surface is obtained through an acid wash treatment in which glass beads or glass slides are immersed in the 2M sulfuric acid solution for 24 h. The acid-treated samples are subsequently rinsed with distilled water and dried in the lab for two days. Hydrophobic

surface is obtained via the silane-coating method. Clean glass beads or glass slides are immersed in chloro(dodecyl)dimethylsilane for 24 h.(*183, 184*) The reaction can be represented as:

$CH_3(CH_2)_{11}Si(CH_3)_2Cl + -Si-OH \rightarrow -Si-O-Si(CH_3)_2(CH_2)_{11}CH_3 + HCl$

Following the silane coating, the treated sample is rinsed with ethanol to wash off any remaining organic materials.

8.2.3 Contact Angle Measurement

Static contact angles are measured using CAM 200 optical contact angle meter (KSV instruments). A water droplet of 2 μL is formed at the end of the syringe and carefully deposited onto the soda lime glass slide. The images of static contact angle are taken within 5s of water deposition by a charge coupled device (CCD) camera. The static contact angle is calculated by the vendor-supplied software.

8.3 Results and Discussion

8.3.1 Model Systems with Controlled Wettability

To establish the link between NMR-detected water isotherms with surface wettability, we first create model systems with controlled wetting properties. For that, two different surface chemical treatments are implemented to make soda lime glass beads surface either hydrophilic or hydrophobic. The morphology and particle size of 40 μm soda lime glass beads before and after surface modifications are determined by scanning electron microscope (SEM). In Figure 8.4a, SEM images show that the three representative samples, assigned as unmodified, hydrophilic, and hydrophobic glass beads, have uniform spherical morphology in large domains. All three samples consist of uniform spheres with a size of approximately 40 μm, which agrees well with the supplier's characterization−particle size ranging from 38 to 45 μm.

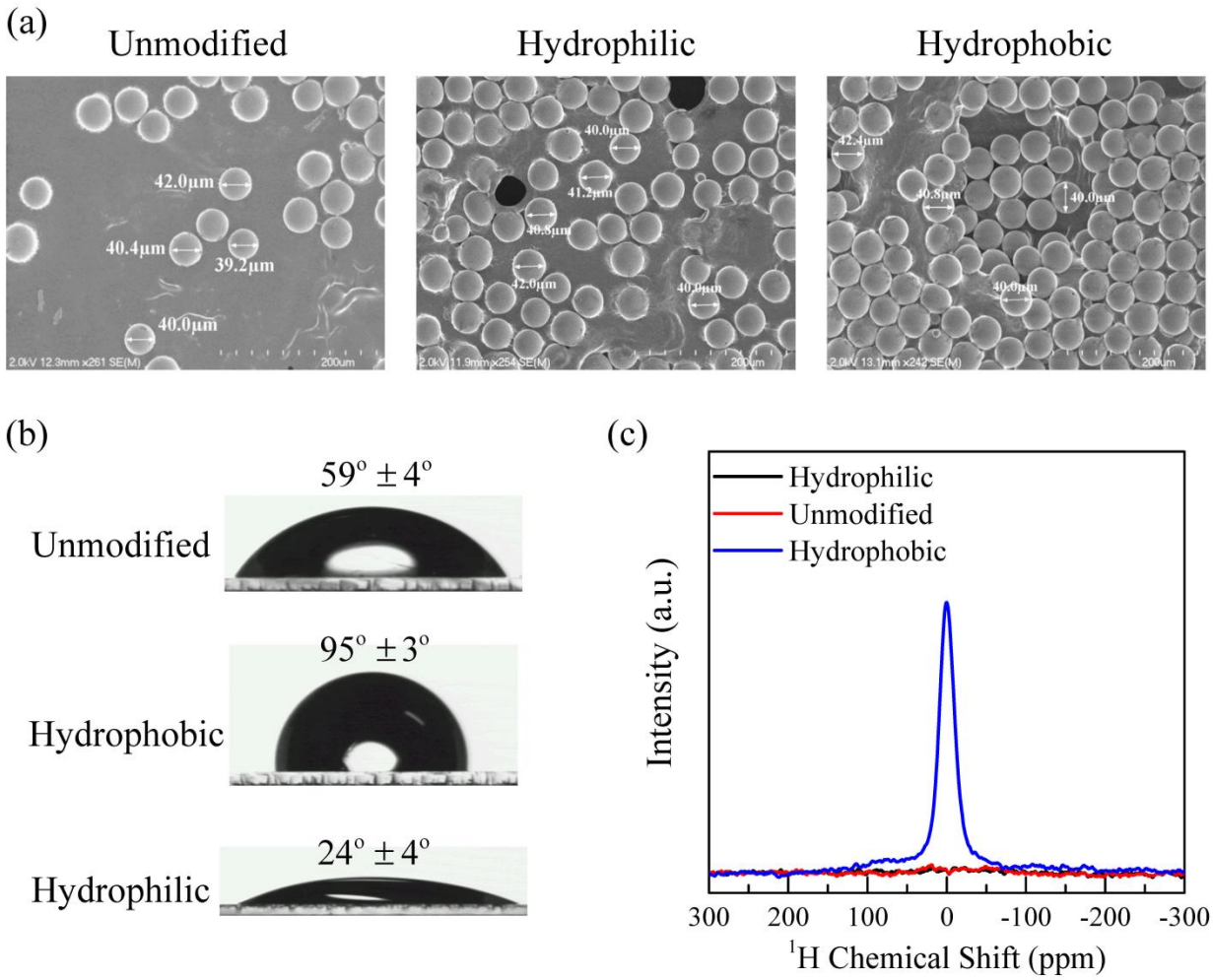

Figure 8.4 (a) SEM images of 40 μm soda lime glass beads with unmodified, hydrophilic, and hydrophobic surface, respectively. (b) Images of water drop on soda lime glass slides and resulting static contact angles with unmodified, hydrophobic, and hydrophilic surface, respectively. (c) ^{1}H NMR spectra of dry glass beads after different chemical modifications. A strong ^{1}H signal is observed in the hydrophobically treated glass beads due to the long chained coating polymer ($-(CH_2)_{11}CH_3$). The ^{1}H peak of hydrophobically coated glass beads is set at 0 ppm. The bulk water proton peak is therefore centered at 4.19 ppm.

The resulting change in surface wettability is characterized by monitoring the change in static contact angle. Soda lime glass slides that have an identical composition with soda lime glass beads are applied in contact angle tests. Figure 8.4b shows the static contact angles of water on unmodified, hydrophilic, and hydrophobic treated glass slides, respectively. The macroscopic

contact angle of the unmodified glass surface is ~59°, indicating that soda lime glass surface is intrinsically mildly hydrophilic. After silane coating, the contact angle increases to ~95°, suggesting a much better degree of hydrophobicity compared to the unmodified surface. The strong hydrophobicity of the silane-coated surface comes from the outermost long alkyl chains ($-(CH_2)_{11}CH_3$), which is verified by the strong ^{1}H NMR signal in the silane-coated sample, see Figure 8.4c. Soda lime glass surface after the acid wash is clearly tuned to hydrophilic with a contact angle ~24°. Hence, through different chemical modification methods, the surface wettability can be controlled from hydrophobic to hydrophilic. In the following isotherm measurements, identical chemical modification methods are applied to soda lime glass beads. Since the chemical composition of glass beads and glass slides are identical, it is assumed that the chemical treatments also work for glass beads, resulting in similar surface wettability.

8.3.2 Surface Wettability Characterized by NMR-Detected Water Isotherms

Figure 8.5a shows the in situ NMR-detected water adsorption isotherms of hydrophilic, hydrophobic, and unmodified 40 μm soda lime glass beads at 293 K. Both the shape of isotherm and the amount of water adsorbed provide important information. For all the granular beads samples, not only in Figure 8.5 but also in Figure 8.6, Figure 8.7, and Figure 8.8, water isotherms are characterized by two distinct relative pressure regions. In the low relative pressure range, e.g., $0 < P/P_{sat} < 0.6$ of the unmodified sample, water uptake increases gradually, indicating that water is mainly filling the beads surface. However, at high relative pressures ($P/P_{sat} > 0.8$), a significant increase in the uptake of water occurs for all samples under investigation. This is typically dominated by the capillary condensation between grains, which agrees with previous findings.(*185-187*)

The amounts of water adsorbed are also in good agreement with the wetting properties determined from the above contact angle measurements. For the hydrophobically treated glass beads, the water isotherm lies nearly flat along the P/P_{sat} axis over the entire range, showing negligible water adsorption. In contrast, compared with the hydrophobically treated glass beads, a significantly larger amount of water adsorption is observed on the hydrophilic-treated glass beads. Specifically, the amount of water adsorbed on the hydrophilic beads at the same relative pressure is greater than both the unmodified and hydrophobic sample, indicating a greater degree of hydrophilicity. As expected, the water adsorption isotherm of unmodified glass beads lies between the hydrophilic and hydrophobic curves.

Furthermore, an analytical correlation of contact angle θ and the amount of water adsorbed has been established. The two variables involved are $\cos\theta$ and normalized water content $W' = W/A$ at P/P_{sat} = 0.2, where water content W equals to water mass divided by the glass beads mass, A is the surface area of glass beads. Here, we choose P/P_{sat} = 0.2 because water adsorption is dominated by the beads surface at low relative pressures. This ensures that the surface wettability plays a critical role in the normalized water adsorption amount W'. W' at P/P_{sat} = 0.2 of hydrophobic, unmodified, and hydrophilic glass beads are 4.3×10^{-8}, 7.2×10^{-7}, and 1.2×10^{-6} g/cm^2, respectively. Moreover, as shown in Figure 8.5b, there is a linear correlation between $\cos\theta$ and W' at P/P_{sat} = 0.2: $W' = 1.2 \times 10^{-6} \times \cos\theta + 1.4 \times 10^{-7}$. This is purely empirical but it reveals key information about surface wettability and the amount of water adsorbed per unit area which could be determined by the combination of isotherm technique and pore surface area measurement, e.g., N_2 Brunauer-Emmett-Teller (BET) method. It demonstrates that water adsorption isotherms can clearly distinguish between hydrophobic and hydrophilic surfaces embedded in a granular or porous structure, which the contact angle measurement

cannot achieve. This is of particular importance in determining the wetting properties of reservoir rocks.

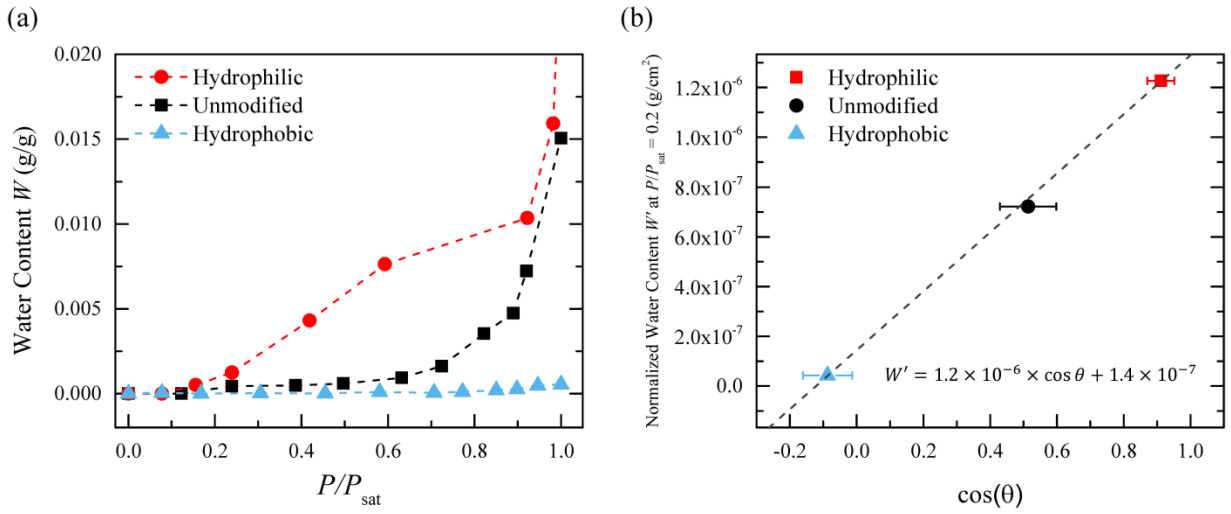

Figure 8.5 (a) NMR-detected water isotherms of hydrophilic, hydrophobic, and unmodified 40 μm soda lime glass beads at 293 K. P is the pressure of water vapor and P_{sat} is the saturation pressure of water at 293 K. Water content W is defined as the water mass divided by the glass beads mass. (b) The correlation of contact angle θ and normalized water content $W' = W/A$ at P/P_{sat} = 0.2. The data obtained from the three glass beads samples gives a straight line.

So far, we have only considered uniform-sized grains, which is an ideal system when compared with the "natural" porous media. In the following, the NMR-based isotherm technique is applied to composite beads samples to demonstrate its general applicability. Some important features of the reservoir rocks, such as wide pore size distribution and heterogeneous surface wettability, hold as well in those composite beads samples. For example, the pore sizes created by the separately packed glass beads (see Figure 8.6) are similar to those of macropores and micropores of Middle East Arab formation carbonates, ~5 μm and ~100 μm, respectively.(*188*)

8.3.3 Effect of Spatial Distribution of Pores on Adsorption Isotherms

Figure 8.6 plots the water adsorption isotherms of beads mixtures with separate and mixed arrangements as shown on the left. In the separate arrangement, 20 μm beads are first

filled into the sample tube; then the sample tube is gently tapped to get a compact packing. Afterward, 400 μm beads are loaded into the tube and form a separate group on the top of the 20 μm beads. In the mixed packing, before transferred to the sample tube, 20 μm and 400 μm beads are thoroughly mixed. Subsequently, the mixture is packed into the tube to achieve a mixed arrangement. In this section, in each sample, 50 wt% 20 μm and 50 wt% 400 μm beads are used.

Figure 8.6b compares the water adsorption isotherms of hydrophilic 20 μm and hydrophilic 400 μm beads mixture in mixed and separate packing, respectively. The key difference between these two samples is the pore space. In the mixed sample, it can be assumed that the pore size is continuously varying according to the local packing. However, the separate packing has two well-defined pore sizes: ~5 μm and ~100 μm. Nonetheless, as seen in Figure 8.6b, the adsorption isotherms fall on top of each other indicating that surface not pore space is the dominant factor in wetting. In order to exclude the effect of surface wettability, water isotherms of the mixtures of hydrophobic 20 μm and hydrophobic 400 μm beads in separate and mixed arrangements are compared in Figure 8.6c. Again, the isotherms of separate and mixed arrangements are indistinguishable. Thus, it can be concluded that water adsorption isotherm does not depend on the spatial distribution of the pores, proving that the isotherm is determined by surface wetting, not by pore filling, and is generally applicable.

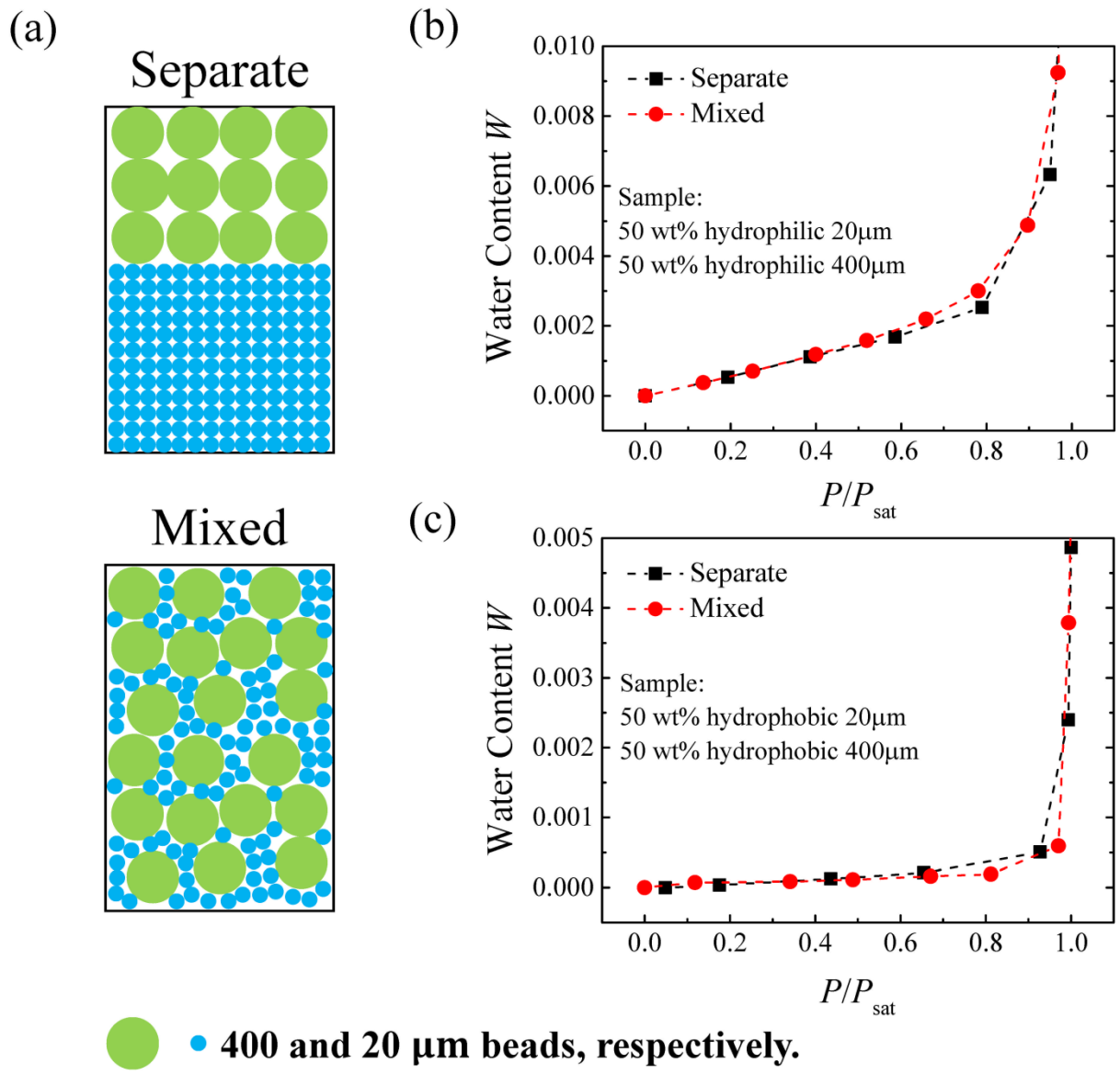

Figure 8.6 (a) Schematic representations of the separate and mixed arrangements of glass beads. (b, c) Water adsorption isotherms of the bead mixtures in separate and mixed arrangements; (b) 50 wt% hydrophilic 20 μm and 50 wt% hydrophilic 400 μm glass beads; (c) 50 wt% hydrophobic 20 μm and 50 wt% hydrophobic 400 μm glass beads.

8.3.4 Water Adsorption Amount and Surface Area

To confirm the conclusion that surface is the dominant factor in adsorption, a quantitative relationship between the amount of water adsorbed and surface area is analyzed. As sketched in Figure 8.7 and listed in Table 8.1, four sets of samples are prepared. In each sample, hydrophilic

20 μm and hydrophilic 400 μm beads are packed in the separate arrangement. If we assume that the beads are perfectly spherical, as appears to be the case for the glass beads used here, then we expect the surface-area-to-mass ratio of the glass beads is given by $6/D\rho$, where D is the sphere diameter, 20 μm or 400 μm, and ρ is the density of glass bead, which is 2.5 g/cm^3. The surface area ratios of the four samples are listed in Table 8.1. Figure 8.7b shows the water adsorption isotherms of the four samples, set 1a-d. The amount of water adsorption increases with the surface area. Moreover, as shown in Figure 8.7c, when normalized by the surface area, the adsorption curves for all four samples collapse into a single curve, again confirming that the water adsorption mainly depends on the surface. In addition, the normalized water content W' of the four samples Set 1a-d at $P/P_{sat} = 0.2$ is 1.2×10^{-6} g/cm^2, in good agreement with the data of hydrophilic 40 μm beads.

Table 8.1 Experiments on various mixtures of hydrophilic beads to elucidate the water adsorption on the geometric surface area.

Set	Separate arrangement	Mass % hydrophilic 20 μm beads	Mass % hydrophilic 400 μm beads	Surface area ratio
1a	yes	10	90	1.0
1b	yes	25	75	19.8
1c	yes	50	50	36.2
1d	yes	75	25	52.6

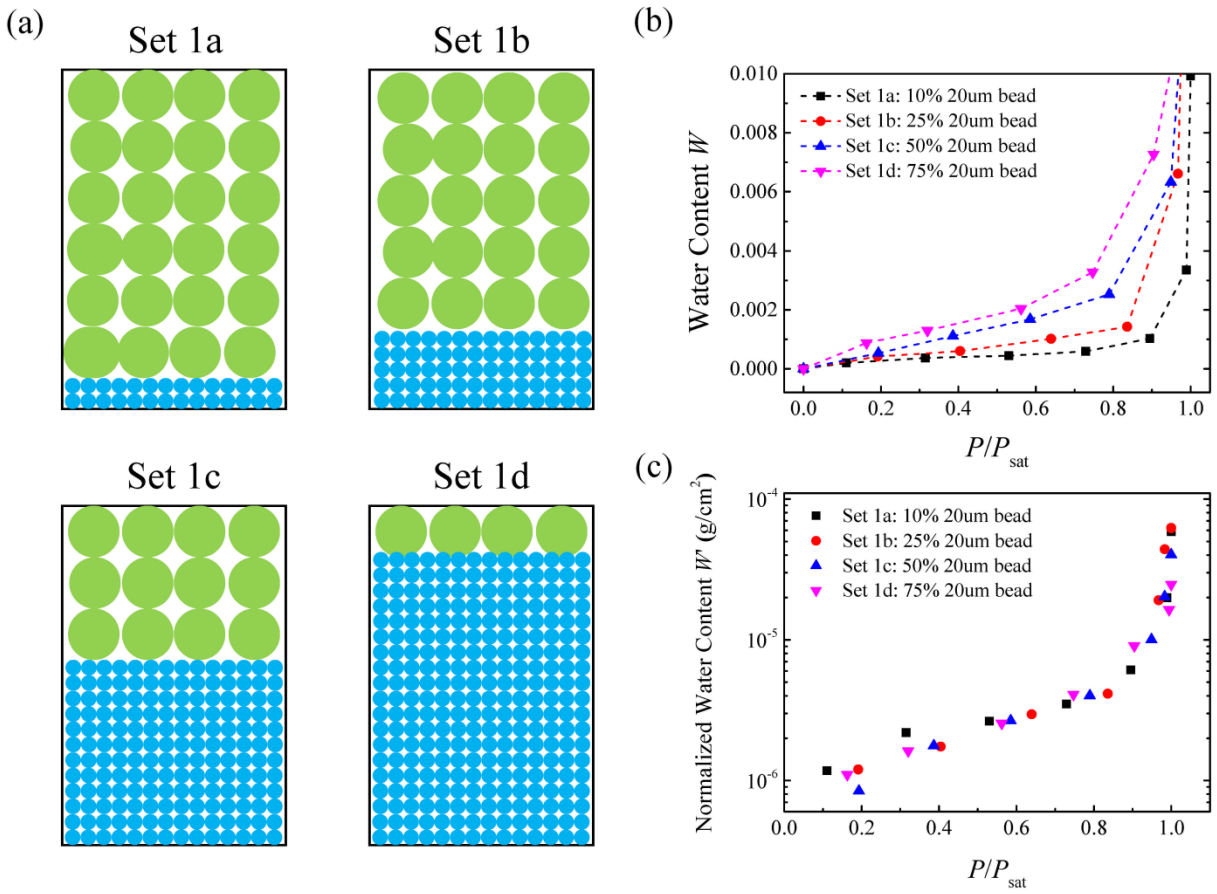

Figure 8.7 (a) Four samples of glass beads arranged in the separate formation. Both 20 μm and 400 μm beads are prepared in the hydrophilic state. The mass percentages of 20 μm beads in Set 1a, 1b, 1c, and 1d are 10%, 25%, 50%, and 75%, respectively. (b) NMR-detected water isotherms of set 1a-d. (c) When normalized by the total surface area the adsorption curves for the four sample sets shown in Figure 8.7b collapse into one master curve.

8.3.5 Water Isotherms of Samples with Heterogeneous Wettability

Research into the wetting-state of reservoir rocks suggests that wettability in a reservoir rock is typically heterogeneous, comprising distinguishable zones that are respectively hydrophilic and hydrophobic.(*189*) To mimic the natural reservoir rock, glass beads samples with mixed wettability are tested. Details about the sample set 2a-e are listed in Table 8.2. In each sample, 20 μm and 400 μm beads are packed in the mixed arrangement. Figure 8.8a shows

the water adsorption isotherms of set 2a-e. The sample set 2a containing the largest hydrophilic surface area adsorbs the greatest amount of water. In contrast, the sample set 2d, consisting of hydrophobic treated 20 μm and hydrophobic treated 400 μm beads, adsorbs the least amount of water. These results suggest that the amount of water adsorbed in porous media with heterogeneous wettability is also determined by the hydrophilic surface. This is born out more clearly when the isotherms are plotted in terms of water adsorption per hydrophilic surface area as is done in Figure 8.8b. All water isotherms collapse onto a single curve, indicating that the water adsorption mainly depends on the total hydrophilic surface area. This conclusion is crucial for core rock surface modification and further analysis.

Table 8.2 Experiments on various beads mixtures with mixed wettability.

Set	**Mass % hydrophilic 20 μm beads**	**Mass % hydrophobic 20 μm beads**	**Mass % hydrophilic 400 μm beads**	**Mass % hydrophobic 400 μm beads**
2a	50	–	50	–
2b	50	–	–	50
2c	–	50	50	–
2d	–	50	–	50
2e	25	25	25	25

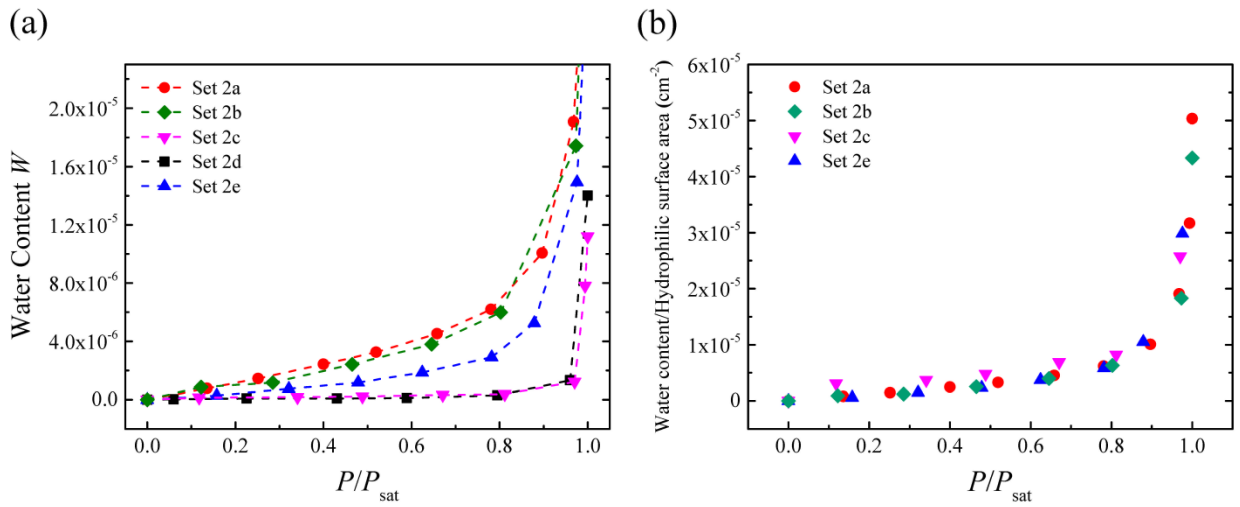

Figure 8.8 (a) Water isotherms of the five samples set 2a-e listed in Table 8.2. (b) When normalized by total hydrophilic surface area all the isotherm curves collapse into one curve indicating that the hydrophilic surface area is the dominant factor in wetting.

8.3.6 Water Adsorption Isotherms on Reservoir Rocks

Furthermore, NMR water adsorption isotherm technique is used to characterize the wettability of reservoir rocks. Two types of reservoir rocks are studied: a carbonate reservoir rock in the Middle East and an Indiana limestone. The sample is prepared as follows. A slice of the rock is cut off, broken into small pieces using a mortar and pestle which are subsequently sieved. Particles with sizes between 355 and 500 μm are selected for the experiments. Water adsorption isotherms are conducted on the pristine rocks and modified rocks which have been exposed to hydrophilic or hydrophobic treatments. A comparison of the water adsorption isotherms between the pristine rocks is shown in Figure 8.9a. In both cases, we observe a low-pressure region ($0 < P/P_{sat} < 0.65$) where the adsorption isotherm is almost flat to the horizontal axis and a high-pressure region ($P/P_{sat} > 0.95$) where the adsorption isotherm increases vertically. Compared to the aforementioned glass beads data, we know that the low-pressure region is dominated by surface adsorption and the high-pressure range is controlled by the capillary

condensation. In the intermediate relative pressure range, $0.65 < P/P_{sat} < 0.95$, water uptake is sharp in the carbonate rock but gradual in Indiana limestone. Our previous study on porous activated carbons with different pore sizes shows that the significant increase in the uptake of water at intermediate relative pressure is associated with the pore condensation.(*88*) That is, the sharp increase above $P/P_{sat} = 0.65$ in carbonate rock indicates that the carbonate rock possesses more hydrophilic surface area and more well-defined pores than the Indiana limestone. The high porosity of the carbonate rock in the Middle East is in agreement with the previous report. Abdulrahman S. Alsharhan *et al.* found that the carbonate reservoirs rocks in the Middle East show exceptionally high porosity up to 30%, which makes the Arabian Gulf one of the most prolific oil fields in the world.(*190*) While the porosity of Indiana limestone typically ranges from 12% ~ 18%.(*191, 192*) Regardless of those research data, the higher porosity in the carbonate reservoir rock can be distinguished easily in the lab. The inset figures in Figure 8.9a are photos of the cross sections of carbonate reservoir rock (left) and Indiana limestone (right), respectively. Clearly, there are many pores and cracks in the carbonate reservoir rock. In contrast, the cross-sectional surface of Indiana limestone is more compact and has fewer pores. Figure 8.9b presents the NMR-detected water isotherms of rocks after surface treatments. The surface treatment is successful: hydrophobic surfaces show negligible adsorption while hydrophilic treatment induces enhanced water adsorption. Moreover, after surface modifications, water isotherms of the modified rocks overlap with each other, showing that both rocks respond similarly to the hydrophilic and hydrophobic modifications. Water isotherms on the reservoir rocks show that surface properties and pore structure differences can be detected by the NMR water adsorption isotherm technique, leading to new insights that are needed in optimizing hydrocarbon production.

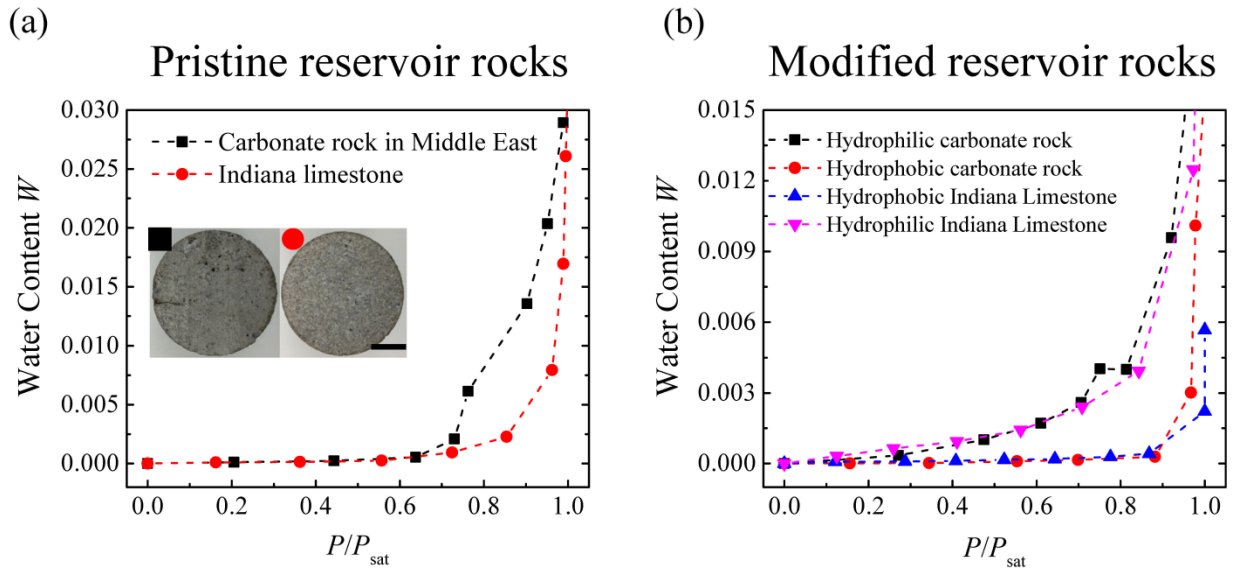

Figure 8.9 (a) Comparison of water adsorption isotherms on the pristine carbonate reservoir rock in the Middle East (black) and Indiana limestone (red). Inset: photos of carbonate reservoir rock (left) and Indiana limestone (right), respectively. The diameter of both rocks is 3.8 cm. The scale bar is 1 cm. (b) Water adsorption isotherms of hydrophilic or hydrophobic treated reservoir rocks.

8.4 Summary and Outlook

We present an in situ NMR-based methodology to measure the wettability of porous media, e.g. reservoir rocks. The water adsorption isotherm is shown to be in good correlation with contact angle measurements, and provide a wettability index to quantify the hydrophilic/hydrophobic characteristics of porous media. The in situ measurements of water isotherms on glass beads phantoms configured with distinct geometric packing, different surface area, and heterogeneous wettability confirm that the isotherm is determined by the surface wettability, not by pore filling. The NMR water isotherm method is further applied to study the reservoir core rocks. The clear difference in water isotherms of the pristine rocks shows that the carbonate reservoir rock in the Middle East possesses more hydrophilic surface area and more well-defined pores than the Indiana limestone. These findings contribute to an improved

understanding of formation wettability and demonstrate that the NMR water isotherm technique is very powerful in the water-interface study.

CHAPTER 9 CONCLUSIONS AND FURTHER WORK

We have shown that NMR spectroscopy is a powerful technique for studying fluids in the nanoscopic space. We have focused our topics on the characterization of the phase behavior, structure, and dynamics of confined fluids, and the changes that occur upon response to external conditions. Specifically, we have studied water clusters within hydrophobic nanopores, CWAs simulants inside microporous MOFs, aqueous solutions confined in carbon nanopores, and water in reservoir rocks. Based on these studies, we have developed a detailed understanding of the factors that influence the form of the NMR spectra for fluids under confinement. Additionally, in-depth characterization at the molecular level of such systems has been proven to be important for the understanding of mechanisms, the elucidation of extrinsic properties, and the refining of preparation methods.

The success of the NMR approach stems from the unique ability to separately observe the in-pore species. For fluids confined inside conjugated systems such as activated carbon and MOFs, the in-pore species experience shielding due to the ring current effect, giving rise to a nucleus-independent chemical shift (NICS). DFT calculations show that the observed chemical shifts (NICS) of in-pore nuclei depend sensitively on the distance between the nuclear spin and the aromatic compounds. In general, nuclear spins residing closer to the surface resonate at lower frequencies. These findings enable NMR to image confined fluids in conjugated systems with sub-nanometer scale spatial resolution.

First, we take advantage of this NMR imaging capability to study water adsorption in micropores of activated carbon. The detailed nucleation and growth processes of water inside activated carbon micropores are directly observed. Furthermore, we combine the spatially resolved information on structure and dynamics obtained by NICS-resolved NMR with the in situ NMR-detected water isotherm. It is shown that water adsorption starts with nucleation at surface sites at low relative pressures. This is followed by two growth processes at higher relative pressures. One is the gradual growth of water clusters, and the other is the cooperative growth by pore-bridging. These two processes both contribute to the water adsorption associated with the sharp increase in the water isotherm. Finally, approaching the saturation pressure, these two distinct water structures coalesce together, leading to the pore filling along the pores in the final stage. This study showcases the unique strength of NMR spectroscopy to probe the intricacies of confined fluid-solid interactions on the nanometer scale.

We then extend the NICS-based NMR technique to study the water adsorption hysteresis in activated carbons. Correlating the macroscopic sorption isotherm with the microscopic cluster configurations qualitatively captures some features of adsorption and desorption curves. The adsorption branch within the hysteresis loop corresponds to a two-phase process: (i) the nucleation of water clusters on the functional groups and (ii) the formation of cooperative water bridges between the pore walls. These two structures then coalesce into a single percolated water cluster, and at this point hysteresis loop closes. While in the hysteresis region, the desorption curve is predominantly associated with a single water cluster shrinking in size via evaporation. Below the point the hysteresis loop starts, the single water cluster disintegrates into a series of smaller clusters.

NMR also enables interesting insights into the phase behavior of confined liquids. There is a growing realization from simulation studies that miscible mixtures could become immiscible in nanoconfined geometries, but verifying this phenomenon experimentally remains challenging. Here, we use solid-state NMR to probe the molecular organization of aqueous alcohols within graphitic nanopores. The state of nanoconfined alcohol-water mixtures is determined to be a heterogeneous arrangement of an alcohol-rich phase in proximity to the pore surface and a water-rich phase at the pore center. Furthermore, this phase separation behavior remains remarkably stable over a broad temperature range from -60 to 90 ℃. Interestingly, it is found that the alcohol-graphite attractions (-0.21 kJ/mol) and the favorable hydration of alcohols at interfaces (-0.22 kJ/mol) cannot compensate the entropy loss (-0.49 kJ/mol) for the observed alcohol-water separation if we assume the aqueous alcohols are ideal solutions. Thus, our data indicate that the confined aqueous alcohols diverge greatly from the ideal solution model. This observation agrees well with the molecular segregation observed in a concentrated alcohol-water solution, that is, when simple alcohol such as methanol or ethanol is mixed with water, the entropy of the system increases far less than expected for an ideal solution of randomly mixed molecules. This microscopic segregation substantially influences macroscopic properties. The preferentially adsorbed alcohol at the pore surface tunes the wetting behavior of the surface from hydrophobic to hydrophilic, which is confirmed by both the contact angle measurements and adsorption isotherm tests.

MOFs also contain aromatic linkers in the framework, giving rise to nucleus-independent chemical shifts. DFT calculations demonstrate that the NICS values for guest molecules in tetrahedral and octahedral pores have opposite signs, which could be exploited to probe molecular binding sites. Our results indicate that CWAs simulant (isopropanol) preferentially

adsorbs in the tetrahedral pores of UiO-66, subsequently adsorb at defective sites at higher pressures and finally occupy octahedral near saturation. More importantly, competitive adsorption experiments show that the preadsorbed water has two effects on the isopropanol adsorption process. First, the preadsorbed water occupies some binding sites and thus reduce the saturation adsorption capacity for isopropanol. Second, the presence of preadsorbed water significantly decelerates the transport of guest molecules. The equilibrium time increases from 50 min on dry UiO-66 to over 300 min on the hydrated UiO-66, which could be a rate-limiting step in decontamination applications.

Last but not least, we develop an in situ NMR-based methodology to measure the wettability of porous media, e.g. reservoir rocks. The water adsorption isotherm is shown to be in good correlation with contact angle measurements, and provide a wettability index to quantify the hydrophilic/hydrophobic characteristics of porous media. The in situ measurements of water isotherms on glass beads phantoms configured with distinct geometric packing, different surface area, and heterogeneous wettability confirm that the isotherm is determined by the surface wettability, not by pore filling. The NMR water isotherm method is further applied to study the reservoir core rocks. The clear difference in water isotherms of the pristine rocks shows that the carbonate reservoir rock in the Middle East possesses more hydrophilic surface area and more well-defined pores than the Indiana limestone. These findings contribute to an improved understanding of formation wettability and demonstrate that the NMR water isotherm technique is very powerful in the water-interface study.

REFERENCES

1. J. C. T. Eijkel, A. v. d. Berg, Nanofluidics: what is it and what can we expect from it? *Microfluidics and Nanofluidics* **1**, 249-267 (2005).

2. S. Zhang, J. Zhang, Y. Zhang, Y. Deng, Nanoconfined Ionic Liquids. *Chemical Reviews* **117**, 6755-6833 (2017).

3. J. Baugh, A. Kleinhammes, D. Han, Q. Wang, Y. Wu, Confinement Effect on Dipole-Dipole Interactions in Nanofluids. *Science* **294**, 1505-1507 (2001).

4. P. Bampoulis *et al.*, Structure and Dynamics of Confined Alcohol–Water Mixtures. *ACS Nano* **10**, 6762-6768 (2016).

5. F. G. Alabarse *et al.*, Freezing of Water Confined at the Nanoscale. *Physical Review Letters* **109**, 035701 (2012).

6. K. V. Agrawal, S. Shimizu, L. W. Drahushuk, D. Kilcoyne, M. S. Strano, Observation of extreme phase transition temperatures of water confined inside isolated carbon nanotubes. *Nature Nanotechnology* **12**, 267 (2016).

7. Y. Zhang *et al.*, Density hysteresis of heavy water confined in a nanoporous silica matrix. *Proceedings of the National Academy of Sciences* **108**, 12206-12211 (2011).

8. D. Liu *et al.*, Observation of the density minimum in deeply supercooled confined water. *Proceedings of the National Academy of Sciences* **104**, 9570-9574 (2007).

9. Y.-Q. Song, Magnetic Resonance of Porous Media (MRPM): A perspective. *Journal of Magnetic Resonance* **229**, 12-24 (2013).

10. Y.-Q. Song, S. Ryu, P. N. Sen, Determining multiple length scales in rocks. *Nature* **406**, 178 (2000).

11. A. Marchetti *et al.*, Understanding Surface and Interfacial Chemistry in Functional Nanomaterials via Solid-State NMR. *Advanced Materials* **29**, 1605895 (2017).

12. R. Bhattacharyya *et al.*, In situ NMR observation of the formation of metallic lithium microstructures in lithium batteries. *Nature Materials* **9**, 504 (2010).

13. L. Bliumkin *et al.*, Development of an in Situ NMR Photoreactor To Study Environmental Photochemistry. *Environmental Science & Technology* **50**, 5506-5516 (2016).

14. C. P. Grey, J. M. Tarascon, Sustainability and in situ monitoring in battery development. *Nature Materials* **16**, 45 (2016).

15. A. G. Palmer, C. D. Kroenke, J. Patrick Loria, in *Methods in Enzymology*, T. L. James, V. Dötsch, U. Schmitz, Eds. (Academic Press, 2001), vol. 339, pp. 204-238.

16. L. E. Kay, D. A. Torchia, A. Bax, Backbone dynamics of proteins as studied by nitrogen-15 inverse detected heteronuclear NMR spectroscopy: application to staphylococcal nuclease. *Biochemistry* **28**, 8972-8979 (1989).

17. A. Mittermaier, L. E. Kay, New Tools Provide New Insights in NMR Studies of Protein Dynamics. *Science* **312**, 224-228 (2006).

18. A. Cavalli, X. Salvatella, C. M. Dobson, M. Vendruscolo, Protein structure determination from NMR chemical shifts. *Proceedings of the National Academy of Sciences* **104**, 9615-9620 (2007).

19. J. H. Chill, J. M. Louis, C. Miller, A. Bax, NMR study of the tetrameric KcsA potassium channel in detergent micelles. *Protein Science* **15**, 684-698 (2006).

20. Z.-X. Luo, Y.-Z. Xing, Y.-C. Ling, A. Kleinhammes, Y. Wu, Electroneutrality breakdown and specific ion effects in nanoconfined aqueous electrolytes observed by NMR. *Nature Communications* **6**, 6358 (2015).

21. X. Liu *et al.*, NMR Study of Preferential Endohedral Adsorption of Methanol in Multiwalled Carbon Nanotubes. *The Journal of Physical Chemistry C* **116**, 7803-7809 (2012).

22. W. Sekhaneh, M. Kotecha, U. Dettlaff-Weglikowska, W. S. Veeman, High resolution NMR of water absorbed in single-wall carbon nanotubes. *Chemical Physics Letters* **428**, 143-147 (2006).

23. A. Kleinhammes *et al.*, Gas adsorption in single-walled carbon nanotubes studied by NMR. *Physical Review B* **68**, 075418 (2003).

24. R. Valiullin *et al.*, Exploration of molecular dynamics during transient sorption of fluids in mesoporous materials. *Nature* **443**, 965 (2006).

25. J. Kärger, R. Valiullin, Mass transfer in mesoporous materials: the benefit of microscopic diffusion measurement. *Chemical Society Reviews* **42**, 4172-4197 (2013).

26. Alexander C. Forse *et al.*, Direct observation of ion dynamics in supercapacitor electrodes using in situ diffusion NMR spectroscopy. *Nature Energy* **2**, 16216 (2017).

27. H. Li, J. Xiao, Q. Fu, X. Bao, Confined catalysis under two-dimensional materials. *Proceedings of the National Academy of Sciences* **114**, 5930-5934 (2017).

28. W. Zhang, S. Xu, X. Han, X. Bao, In situ solid-state NMR for heterogeneous catalysis: a joint experimental and theoretical approach. *Chemical Society Reviews* **41**, 192-210 (2012).

29. S. Xu, W. Zhang, X. Liu, X. Han, X. Bao, Enhanced In situ Continuous-Flow MAS NMR for Reaction Kinetics in the Nanocages. *Journal of the American Chemical Society* **131**, 13722-13727 (2009).

30. G. W. Wagner, Q. Chen, Y. Wu, Reactions of VX, GD, and HD with Nanotubular Titania. *The Journal of Physical Chemistry C* **112**, 11901-11906 (2008).

31. J.-R. Li, J. Sculley, H.-C. Zhou, Metal–Organic Frameworks for Separations. *Chemical Reviews* **112**, 869-932 (2012).

32. S. Li, J. Li, J. Tang, F. Deng, Host-guest interaction of styrene and ethylbenzene in MIL-53 studied by solid-state NMR. *Solid State Nuclear Magnetic Resonance* **90**, 1-6 (2018).

33. J. J. Chen *et al.*, Ex Situ NMR Relaxometry of Metal–Organic Frameworks for Rapid Surface-Area Screening. *Angewandte Chemie International Edition* **52**, 12043-12046 (2013).

34. Y.-Z. Xing, Z.-X. Luo, A. Kleinhammes, Y. Wu, Probing carbon micropore size distribution by nucleus independent chemical shift. *Carbon* **77**, 1132-1139 (2014).

35. I. I. Rabi, J. R. Zacharias, S. Millman, P. Kusch, A New Method of Measuring Nuclear Magnetic Moment. *Physical Review* **53**, 318-318 (1938).

36. I. Rabi, The Discovery of NMR. *http://mriquestions.com/who-discovered-nmr.html*.

37. F. Bloch, W. W. Hansen, M. Packard, The Nuclear Induction Experiment. *Physical Review* **70**, 474-485 (1946).

38. E. M. Purcell, H. C. Torrey, R. V. Pound, Resonance Absorption by Nuclear Magnetic Moments in a Solid. *Physical Review* **69**, 37-38 (1946).

39. N. F. Ramsey, Early History of Magnetic Resonance. *Physics in Perspective* **1**, 123-135 (1999).

40. J. S. Rigden, Quantum states and precession: The two discoveries of NMR. *Reviews of Modern Physics* **58**, 433-448 (1986).

41. M. H. Levitt, Spin dynamics. *Jon Wiley and Sons* **196**, (2001).

42. O. Ioannidou, A. Zabaniotou, Agricultural residues as precursors for activated carbon production—A review. *Renewable and Sustainable Energy Reviews* **11**, 1966-2005 (2007).

43. R. J. White, V. Budarin, R. Luque, J. H. Clark, D. J. Macquarrie, Tuneable porous carbonaceous materials from renewable resources. *Chemical Society Reviews* **38**, 3401-3418 (2009).

44. B. Hu *et al.*, Engineering Carbon Materials from the Hydrothermal Carbonization Process of Biomass. *Advanced Materials* **22**, 813-828 (2010).

45. M.-M. Titirici, M. Antonietti, Chemistry and materials options of sustainable carbon materials made by hydrothermal carbonization. *Chemical Society Reviews* **39**, 103-116 (2010).

46. D. Mohan, C. U. Pittman, Arsenic removal from water/wastewater using adsorbents—A critical review. *Journal of Hazardous Materials* **142**, 1-53 (2007).

47. S. Choi, J. H. Drese, C. W. Jones, Adsorbent Materials for Carbon Dioxide Capture from Large Anthropogenic Point Sources. *ChemSusChem* **2**, 796-854 (2009).

48. A. G. Pandolfo, A. F. Hollenkamp, Carbon properties and their role in supercapacitors. *Journal of Power Sources* **157**, 11-27 (2006).

49. F. Rodríguez-reinoso, The role of carbon materials in heterogeneous catalysis. *Carbon* **36**, 159-175 (1998).

50. E. Auer, A. Freund, J. Pietsch, T. Tacke, Carbons as supports for industrial precious metal catalysts. *Applied Catalysis A: General* **173**, 259-271 (1998).

51. E. C. Dillon, J. H. Wilton, J. C. Barlow, W. A. Watson, Large surface area activated charcoal and the inhibition of aspirin absorption. *Annals of Emergency Medicine* **18**, 547-552 (1989).

52. A. Zahab, L. Spina, P. Poncharal, C. Marlière, Water-vapor effect on the electrical conductivity of a single-walled carbon nanotube mat. *Physical Review B* **62**, 10000-10003 (2000).

53. G. Le Bozec, S. Giraudet, L. Le Polles, P. Le Cloirec, 1H NMR Investigations of Activated Carbon Loaded with Volatile Organic Compounds: Quantification, Mechanisms, and Diffusivity Determination. *Langmuir* **33**, 1605-1613 (2017).

54. K. S. Sing, Reporting physisorption data for gas/solid systems with special reference to the determination of surface area and porosity (Recommendations 1984). *Pure and applied chemistry* **57**, 603-619 (1985).

55. M. D. Donohue, G. L. Aranovich, Classification of Gibbs adsorption isotherms. *Advances in Colloid and Interface Science* **76-77**, 137-152 (1998).

56. M. Thommes *et al.*, in *Pure and applied chemistry*. (2015), vol. 87, pp. 1051.

57. G.-P. Hao *et al.*, Unusual Ultra-Hydrophilic, Porous Carbon Cuboids for Atmospheric-Water Capture. *Angewandte Chemie International Edition* **54**, 1941-1945 (2015).

58. K. Kaneko, Water capture in carbon cuboids. *Nature Chemistry* **7**, 194 (2015).

59. E. de la Llave, V. Molinero, D. A. Scherlis, Role of Confinement and Surface Affinity on Filling Mechanisms and Sorption Hysteresis of Water in Nanopores. *The Journal of Physical Chemistry C* **116**, 1833-1840 (2012).

60. M. H. Factorovich, E. Gonzalez Solveyra, V. Molinero, D. A. Scherlis, Sorption Isotherms of Water in Nanopores: Relationship Between Hydropohobicity, Adsorption Pressure, and Hysteresis. *The Journal of Physical Chemistry C* **118**, 16290-16300 (2014).

61. Y. Men, Q. Yan, G. Jiang, X. Zhang, W. Wang, Nucleation and hysteresis of vapor-liquid phase transitions in confined spaces: Effects of fluid-wall interaction. *Physical Review E* **79**, 051602 (2009).

62. P. Monson, Contact angles, pore condensation, and hysteresis: insights from a simple molecular model. *Langmuir* **24**, 12295-12302 (2008).

63. L. Liu *et al.*, Water adsorption on carbon - A review. *Advances in Colloid and Interface Science* **250**, 64-78 (2017).

64. C. S. Dewey, P. K. Lefforge, G. L. Cabot, Moisture Sorption by Carbon Black. *Industrial & Engineering Chemistry* **24**, 1045-1050 (1932).

65. J. W. McBain, J. Porter, R. Sessions, The nature of the sorption of water by charcoal. *Journal of the American Chemical Society* **55**, 2294-2304 (1933).

66. E. A. Müller, L. F. Rull, L. F. Vega, K. E. Gubbins, Adsorption of Water on Activated Carbons: A Molecular Simulation Study. *The Journal of Physical Chemistry* **100**, 1189-1196 (1996).

67. E. A. Müller, K. E. Gubbins, Molecular simulation study of hydrophilic and hydrophobic behavior of activated carbon surfaces. *Carbon* **36**, 1433-1438 (1998).

68. M. Jorge, C. Schumacher, N. A. Seaton, Simulation Study of the Effect of the Chemical Heterogeneity of Activated Carbon on Water Adsorption. *Langmuir* **18**, 9296-9306 (2002).

69. A. Striolo, A. A. Chialvo, P. T. Cummings, K. E. Gubbins, Simulated water adsorption in chemically heterogeneous carbon nanotubes. *The Journal of Chemical Physics* **124**, 074710 (2006).

70. J. K. Brennan, T. J. Bandosz, K. T. Thomson, K. E. Gubbins, Water in porous carbons. *Colloids and Surfaces A: Physicochemical and Engineering Aspects* **187-188**, 539-568 (2001).

71. T. Ohba, H. Kanoh, K. Kaneko, Water Cluster Growth in Hydrophobic Solid Nanospaces. *Chemistry - A European Journal* **11**, 4890-4894 (2005).

72. T. Ohba, H. Kanoh, K. Kaneko, Cluster-Growth-Induced Water Adsorption in Hydrophobic Carbon Nanopores. *The Journal of Physical Chemistry B* **108**, 14964-14969 (2004).

73. T. Kimura *et al.*, Cluster-Associated Filling of Water in Hydrophobic Carbon Micropores. *The Journal of Physical Chemistry B* **108**, 14043-14048 (2004).

74. T. Ohba, H. Kanoh, K. Kaneko, Affinity Transformation from Hydrophilicity to Hydrophobicity of Water Molecules on the Basis of Adsorption of Water in Graphitic Nanopores. *Journal of the American Chemical Society* **126**, 1560-1562 (2004).

75. T. Ohba, K. Kaneko, Cluster-associated filling of water molecules in slit-shaped graphitic nanopores. *Molecular Physics* **105**, 139-145 (2007).

76. T. Ohba, H. Kanoh, K. Kaneko, Water Cluster Growth in Hydrophobic Solid Nanospaces. *Chemistry – A European Journal* **11**, 4890-4894 (2005).

77. S. Wang, R. Futamura, K. Kaneko, Cluster-associated filling of water molecules in graphene-based mesopores. *Adsorption* **22**, 1035-1042 (2016).

78. J. Bahadur, C. I. Contescu, D. K. Rai, N. C. Gallego, Y. B. Melnichenko, Clustering of water molecules in ultramicroporous carbon: In-situ small-angle neutron scattering. *Carbon* **111**, 681-688 (2017).

79. T. Horikawa, T. Muguruma, D. D. Do, K.-I. Sotowa, J. R. Alcántara-Avila, Scanning curves of water adsorption on graphitized thermal carbon black and ordered mesoporous carbon. *Carbon* **95**, 137-143 (2015).

80. M. Thommes, J. Morell, K. A. Cychosz, M. Fröba, Combining Nitrogen, Argon, and Water Adsorption for Advanced Characterization of Ordered Mesoporous Carbons (CMKs) and Periodic Mesoporous Organosilicas (PMOs). *Langmuir* **29**, 14893-14902 (2013).

81. E. O. Wiig, A. Juhola, The adsorption of water vapor on activated charcoal. *Journal of the American Chemical Society* **71**, 561-568 (1949).

82. M. Nakamura, T. Ohba, P. Branton, H. Kanoh, K. Kaneko, Equilibration-time and pore-width dependent hysteresis of water adsorption isotherm on hydrophobic microporous carbons. *Carbon* **48**, 305-308 (2010).

83. H. Ogasawara *et al.*, Structure and Bonding of Water on Pt(111). *Physical Review Letters* **89**, 276102 (2002).

84. K. Xu, P. Cao, J. R. Heath, Graphene Visualizes the First Water Adlayers on Mica at Ambient Conditions. *Science* **329**, 1188-1191 (2010).

85. T. Mitsui, M. K. Rose, E. Fomin, D. F. Ogletree, M. Salmeron, Water Diffusion and Clustering on Pd(111). *Science* **297**, 1850-1852 (2002).

86. H.-J. Wang, X.-K. Xi, A. Kleinhammes, Y. Wu, Temperature-Induced Hydrophobic-Hydrophilic Transition Observed by Water Adsorption. *Science* **322**, 80-83 (2008).

87. Z.-X. Luo *et al.*, Dehydration of Ions in Voltage-Gated Carbon Nanopores Observed by in Situ NMR. *The Journal of Physical Chemistry Letters* **6**, 5022-5026 (2015).

88. Y. Song *et al.*, Nucleation and Growth Process of Water Adsorption in Micropores of Activated Carbon Revealed by NMR. *The Journal of Physical Chemistry C* **121**, 8504-8509 (2017).

89. T. P. McNicholas *et al.*, H2 Storage in Microporous Carbons from PEEK Precursors. *The Journal of Physical Chemistry C* **114**, 13902-13908 (2010).

90. Y. Chong, A. Kleinhammes, P. Tang, Y. Xu, Y. Wu, Dominant Alcohol–Protein Interaction via Hydration-Enabled Enthalpy-Driven Binding Mechanism. *The Journal of Physical Chemistry B* **119**, 5367-5375 (2015).

91. R. J. Anderson *et al.*, NMR Methods for Characterizing the Pore Structures and Hydrogen Storage Properties of Microporous Carbons. *Journal of the American Chemical Society* **132**, 8618-8626 (2010).

92. J. K. Brennan, T. J. Bandosz, K. T. Thomson, K. E. Gubbins, Water in porous carbons. *Colloids and Surfaces A: Physicochemical and Engineering Aspects* **187–188**, 539-568 (2001).

93. H.-J. Wang, A. Kleinhammes, T. P. McNicholas, J. Liu, Y. Wu, Water Adsorption in Nanoporous Carbon Characterized by in Situ NMR: Measurements of Pore Size and Pore Size Distribution. *The Journal of Physical Chemistry C* **118**, 8474-8480 (2014).

94. C. L. McCallum, T. J. Bandosz, S. C. McGrother, E. A. Müller, K. E. Gubbins, A Molecular Model for Adsorption of Water on Activated Carbon: Comparison of Simulation and Experiment. *Langmuir* **15**, 533-544 (1999).

95. A. Abragam, *The principles of nuclear magnetism*. (Oxford university press, 1961).

96. M. H. Levitt, *Spin dynamics: basics of nuclear magnetic resonance*. (John Wiley & Sons, 2001).

97. G. S. Gogelashvili, R. S. Vartapetyan, D. V. Ladychuk, Y. B. Grunin, E. V. Khozina, Specific Features of the Adsorption and Nuclear Magnetic Relaxation of the Water Molecules in Active Carbons: 2. The State of Water in Active Carbon with Relatively Large Pores According to the NMR Relaxation Data. *Colloid Journal* **66**, 271-276 (2004).

98. T. Ma *et al.*, Single-crystal x-ray diffraction structures of covalent organic frameworks. *Science* **361**, 48-52 (2018).

99. H. Kim *et al.*, Water harvesting from air with metal-organic frameworks powered by natural sunlight. *Science*, (2017).

100. C. S. Diercks, Y. Liu, K. E. Cordova, O. M. Yaghi, The role of reticular chemistry in the design of CO2 reduction catalysts. *Nature Materials* **17**, 301-307 (2018).

101. K. A. Cychosz, R. Guillet-Nicolas, J. García-Martínez, M. Thommes, Recent advances in the textural characterization of hierarchically structured nanoporous materials. *Chemical Society Reviews* **46**, 389-414 (2017).

102. W. Li, J. Liu, D. Zhao, Mesoporous materials for energy conversion and storage devices. *Nature Reviews Materials* **1**, 16023 (2016).

103. M. Salanne *et al.*, Efficient storage mechanisms for building better supercapacitors. *Nature Energy* **1**, 16070 (2016).

104. F. Fathieh *et al.*, Practical water production from desert air. *Science Advances* **4**, (2018).

105. M.-X. Wu, Y.-W. Yang, Metal–Organic Framework (MOF)-Based Drug/Cargo Delivery and Cancer Therapy. *Advanced Materials* **29**, 1606134 (2017).

106. M. Thommes, R. Köhn, M. Fröba, Sorption and pore condensation behavior of pure fluids in mesoporous MCM-48 silica, MCM-41 silica, SBA-15 silica and controlled-pore glass at temperatures above and below the bulk triple point. *Applied Surface Science* **196**, 239-249 (2002).

107. K. Morishige, M. Tateishi, F. Hirose, K. Aramaki, Change in Desorption Mechanism from Pore Blocking to Cavitation with Temperature for Nitrogen in Ordered Silica with Cagelike Pores. *Langmuir* **22**, 9220-9224 (2006).

108. J. Garcia-Martinez *et al.*, Evidence of Intracrystalline Mesostructured Porosity in Zeolites by Advanced Gas Sorption, Electron Tomography and Rotation Electron Diffraction. *ChemCatChem* **6**, 3110-3115 (2014).

109. Q. Yao *et al.*, 3D assembly based on 2D structure of Cellulose Nanofibril/Graphene Oxide Hybrid Aerogel for Adsorptive Removal of Antibiotics in Water. *Scientific Reports* **7**, 45914 (2017).

110. A. V. Neimark, P. I. Ravikovitch, A. Vishnyakov, Adsorption hysteresis in nanopores. *Physical Review E* **62**, R1493-R1496 (2000).

111. Y. Zeng, C. Fan, D. D. Do, D. Nicholson, Evaporation from an Ink-Bottle Pore: Mechanisms of Adsorption and Desorption. *Industrial & Engineering Chemistry Research* **53**, 15467-15474 (2014).

112. L. Sarkisov, P. A. Monson, Modeling of Adsorption and Desorption in Pores of Simple Geometry Using Molecular Dynamics. *Langmuir* **17**, 7600-7604 (2001).

113. E. O. Wiig, A. J. Juhola, The Adsorption of Water Vapor on Activated Charcoal. *Journal of the American Chemical Society* **71**, 561-568 (1949).

114. L. Sarkisov, A. Centineo, S. Brandani, Molecular simulation and experiments of water adsorption in a high surface area activated carbon: Hysteresis, scanning curves and spatial organization of water clusters. *Carbon* **118**, 127-138 (2017).

115. A. C. Forse, C. Merlet, J. M. Griffin, C. P. Grey, New Perspectives on the Charging Mechanisms of Supercapacitors. *Journal of the American Chemical Society* **138**, 5731-5744 (2016).

116. H.-C. Zhou, J. R. Long, O. M. Yaghi, Introduction to Metal–Organic Frameworks. *Chemical Reviews* **112**, 673-674 (2012).

117. M. S. Denny Jr, J. C. Moreton, L. Benz, S. M. Cohen, Metal–organic frameworks for membrane-based separations. *Nature Reviews Materials* **1**, 16078 (2016).

118. A. J. Howarth *et al.*, Chemical, thermal and mechanical stabilities of metal–organic frameworks. *Nature Reviews Materials* **1**, 15018 (2016).

119. A. G. Slater, A. I. Cooper, Function-led design of new porous materials. *Science* **348**, aaa8075 (2015).

120. N. S. Bobbitt *et al.*, Metal–organic frameworks for the removal of toxic industrial chemicals and chemical warfare agents. *Chemical Society Reviews* **46**, 3357-3385 (2017).

121. J. E. Mondloch *et al.*, Destruction of chemical warfare agents using metal–organic frameworks. *Nature Materials* **14**, 512 (2015).

122. N. C. Burtch, H. Jasuja, K. S. Walton, Water Stability and Adsorption in Metal–Organic Frameworks. *Chemical Reviews* **114**, 10575-10612 (2014).

123. A. Ö. Yazaydın *et al.*, Enhanced CO2 Adsorption in Metal-Organic Frameworks via Occupation of Open-Metal Sites by Coordinated Water Molecules. *Chemistry of Materials* **21**, 1425-1430 (2009).

124. H. Li, M. Eddaoudi, M. O'Keeffe, O. M. Yaghi, Design and synthesis of an exceptionally stable and highly porous metal-organic framework. *Nature* **402**, 276 (1999).

125. A. Dhakshinamoorthy, A. Santiago-Portillo, A. M. Asiri, H. Garcia, Engineering UiO-66 Metal Organic Framework for Heterogeneous Catalysis. *ChemCatChem* **0**.

126. A. Nandy, A. C. Forse, V. J. Witherspoon, J. A. Reimer, NMR Spectroscopy Reveals Adsorbate Binding Sites in the Metal–Organic Framework UiO-66(Zr). *The Journal of Physical Chemistry C* **122**, 8295-8305 (2018).

127. J. Chmiola *et al.*, Anomalous Increase in Carbon Capacitance at Pore Sizes Less Than 1 Nanometer. *Science* **313**, 1760-1763 (2006).

128. H. G. Yang *et al.*, Anatase TiO2 single crystals with a large percentage of reactive facets. *Nature* **453**, 638-641 (2008).

129. F. Zaera, Probing Liquid/Solid Interfaces at the Molecular Level. *Chemical Reviews* **112**, 2920-2986 (2012).

130. R. Shimizu, H. Tanaka, Impact of complex topology of porous media on phase separation of binary mixtures. *Science Advances* **3**, (2017).

131. K. Binder, S. Puri, S. K. Das, J. Horbach, Phase Separation in Confined Geometries. *Journal of Statistical Physics* **138**, 51-84 (2010).

132. D. G. Lev, K. E. Gubbins, R. Radhakrishnan, M. Sliwinska-Bartkowiak, Phase separation in confined systems. *Reports on Progress in Physics* **62**, 1573 (1999).

133. K. Binder, in *Encyclopedia of Microfluidics and Nanofluidics*, D. Li, Ed. (Springer US, Boston, MA, 2008), pp. 335-348.

134. K.-i. Murata, H. Tanaka, Impact of surface roughness on liquid-liquid transition. *Science Advances* **3**, (2017).

135. H. Patrick, Soft matter in hard confinement: phase transition thermodynamics, structure, texture, diffusion and flow in nanoporous media. *Journal of Physics: Condensed Matter* **27**, 103102 (2015).

136. S. Iglauer, S. Favretto, G. Spinelli, G. Schena, M. J. Blunt, X-ray tomography measurements of power-law cluster size distributions for the nonwetting phase in sandstones. *Physical Review E* **82**, 056315 (2010).

137. T. Pak, I. B. Butler, S. Geiger, M. I. J. van Dijke, K. S. Sorbie, Droplet fragmentation: 3D imaging of a previously unidentified pore-scale process during multiphase flow in porous media. *Proceedings of the National Academy of Sciences* **112**, 1947-1952 (2015).

138. G. Krausch, Surface induced self assembly in thin polymer films. *Materials Science and Engineering: R: Reports* **14**, v-94 (1995).

139. M. Geoghegan, G. Krausch, Wetting at polymer surfaces and interfaces. *Progress in Polymer Science* **28**, 261-302 (2003).

140. A. K. Metya, S. Khan, J. K. Singh, Wetting Transition of the Ethanol–Water Droplet on Smooth and Textured Surfaces. *The Journal of Physical Chemistry C* **118**, 4113-4121 (2014).

141. M. Lundgren, N. L. Allan, T. Cosgrove, N. George, Wetting of Water and Water/Ethanol Droplets on a Non-Polar Surface: A Molecular Dynamics Study. *Langmuir* **18**, 10462-10466 (2002).

142. N. Severin *et al.*, Nanophase Separation in Monomolecularly Thin Water–Ethanol Films Controlled by Graphene. *Nano Letters* **15**, 1171-1176 (2015).

143. N. Severin, I. M. Sokolov, J. P. Rabe, Dynamics of Ethanol and Water Mixtures Observed in a Self-Adjusting Molecularly Thin Slit Pore. *Langmuir* **30**, 3455-3459 (2014).

144. X. Tian, Z. Yang, B. Zhou, P. Xiu, Y. Tu, Alcohol-induced drying of carbon nanotubes and its implications for alcohol/water separation: A molecular dynamics study. *The Journal of Chemical Physics* **138**, 204711 (2013).

145. Y. Hou, Z. Xu, X. Yang, Interface-Induced Affinity Sieving in Nanoporous Graphenes for Liquid-Phase Mixtures. *The Journal of Physical Chemistry C* **120**, 4053-4060 (2016).

146. M. Zhao, X. Yang, Segregation Structures and Miscellaneous Diffusions for Ethanol/Water Mixtures in Graphene-Based Nanoscale Pores. *The Journal of Physical Chemistry C* **119**, 21664-21673 (2015).

147. S. Gravelle, H. Yoshida, L. Joly, C. Ybert, L. Bocquet, Carbon membranes for efficient water-ethanol separation. *The Journal of Chemical Physics* **145**, 124708 (2016).

148. A. Kommu, J. K. Singh, Separation of Ethanol and Water Using Graphene and Hexagonal Boron Nitride Slit Pores: A Molecular Dynamics Study. *The Journal of Physical Chemistry C* **121**, 7867-7880 (2017).

149. F. Liu, J. Yang, Z. Xu, X. Yang, Selective surface adsorption and pore trapping for ethanol-water mixtures near single-layer polyporous graphynes. *Applied Surface Science* **387**, 1080-1087 (2016).

150. S. D. Janssens *et al.*, Evidence for phase separation of ethanol-water mixtures at the hydrogen terminated nanocrystalline diamond surface. *The Journal of Chemical Physics* **137**, 044702 (2012).

151. D. Damasceno Borges, C. F. Woellner, P. A. S. Autreto, D. S. Galvao, Insights on the mechanism of water-alcohol separation in multilayer graphene oxide membranes: Entropic versus enthalpic factors. *Carbon* **127**, 280-286 (2018).

152. K. Voïtchovsky, D. Giofrè, J. José Segura, F. Stellacci, M. Ceriotti, Thermally-nucleated self-assembly of water and alcohol into stable structures at hydrophobic interfaces. *Nature Communications* **7**, 13064 (2016).

153. X.-Y. Guo, T. Watermann, D. Sebastiani, Local Microphase Separation of a Binary Liquid under Nanoscale Confinement. *The Journal of Physical Chemistry B* **118**, 10207-10213 (2014).

154. D. Chandler, Interfaces and the driving force of hydrophobic assembly. *Nature* **437**, 640-647 (2005).

155. P. T. Callaghan, *Principles of nuclear magnetic resonance microscopy*. (Oxford University Press on Demand, 1993).

156. A. C. Forse, J. M. Griffin, V. Presser, Y. Gogotsi, C. P. Grey, Ring Current Effects: Factors Affecting the NMR Chemical Shift of Molecules Adsorbed on Porous Carbons. *The Journal of Physical Chemistry C* **118**, 7508-7514 (2014).

157. J. M. Griffin, A. C. Forse, C. P. Grey, Solid-state NMR studies of supercapacitors. *Solid State Nuclear Magnetic Resonance* **74–75**, 16-35 (2016).

158. Y. Song *et al.*, Nucleation and Growth Process of Water Adsorption in Micropores of Activated Carbon Revealed by NMR. *The Journal of Physical Chemistry C*, (2017).

159. A. C. Forse *et al.*, NMR Study of Ion Dynamics and Charge Storage in Ionic Liquid Supercapacitors. *Journal of the American Chemical Society* **137**, 7231-7242 (2015).

160. O. Pecher, J. Carretero-González, K. J. Griffith, C. P. Grey, Materials' Methods: NMR in Battery Research. *Chemistry of Materials* **29**, 213-242 (2017).

161. R. C. Haddon, Magnetism of the carbon allotropes. *Nature* **378**, 249-255 (1995).

162. J. H. Guo *et al.*, Molecular Structure of Alcohol-Water Mixtures. *Physical Review Letters* **91**, 157401 (2003).

163. S. Dixit, J. Crain, W. C. K. Poon, J. L. Finney, A. K. Soper, Molecular segregation observed in a concentrated alcohol–water solution. *Nature* **416**, 829 (2002).

164. C. Merlet *et al.*, On the molecular origin of supercapacitance in nanoporous carbon electrodes. *Nat Mater* **11**, 306-310 (2012).

165. P. Lazar *et al.*, Adsorption of Small Organic Molecules on Graphene. *Journal of the American Chemical Society* **135**, 6372-6377 (2013).

166. J. Gienger, N. Severin, J. P. Rabe, I. M. Sokolov, Reconstructing interaction potentials in thin films from real-space images. *Physical Review E* **93**, 043306 (2016).

167. S. K. Allison, J. P. Fox, R. Hargreaves, S. P. Bates, Clustering and microimmiscibility in alcohol-water mixtures: Evidence from molecular-dynamics simulations. *Physical Review B* **71**, 024201 (2005).

168. R. F. Lama, B. C. Y. Lu, Excess Thermodynamic Properties of Aqueous Alcohol Solutions. *Journal of Chemical & Engineering Data* **10**, 216-219 (1965).

169. D. D. Do, *Adsorption analysis: equilibria and kinetics*. (Imperial college press London, 1998), vol. 2.

170. A. J. Patel *et al.*, Extended surfaces modulate hydrophobic interactions of neighboring solutes. *Proceedings of the National Academy of Sciences* **108**, 17678-17683 (2011).

171. Y. Qiu, L. Lupi, V. Molinero, Is Water at the Graphite Interface Vapor-like or Ice-like? *The Journal of Physical Chemistry B*, (2018).

172. H. Li, X. C. Zeng, Wetting and Interfacial Properties of Water Nanodroplets in Contact with Graphene and Monolayer Boron–Nitride Sheets. *ACS Nano* **6**, 2401-2409 (2012).

173. W. Cai *et al.*, Synthesis and Solid-State NMR Structural Characterization of ¹³C-Labeled Graphite Oxide. *Science* **321**, 1815-1817 (2008).

174. M. J. Blunt, *Multiphase flow in permeable media: A pore-scale perspective*. (Cambridge University Press, 2017).

175. J. H. Schön, *Physical properties of rocks: Fundamentals and principles of petrophysics*. (Elsevier, 2015), vol. 65.

176. T. Lee, L. Bocquet, B. Coasne, Activated desorption at heterogeneous interfaces and long-time kinetics of hydrocarbon recovery from nanoporous media. *Nature Communications* **7**, 11890 (2016).

177. K. S. Lee, N. Ivanova, V. M. Starov, N. Hilal, V. Dutschk, Kinetics of wetting and spreading by aqueous surfactant solutions. *Advances in Colloid and Interface Science* **144**, 54-65 (2008).

178. E. Amott. (Society of Petroleum Engineers, 1959), pp. 7.

179. E. C. Donaldson, R. D. Thomas, P. B. Lorenz, Wettability Determination and Its Effect on Recovery Efficiency. *SPE-2338-PA* **9**, 13-20 (1969).

180. Y. Song, H. T. Kwak, A. Kleinhammes, Y. Wu, Hydrophilic and Hydrophobic Characteristics of Reservoir Rocks Quantified by Nuclear Magnetic Resonance-Detected Water Isotherms. *The Journal of Physical Chemistry C* **123**, 6107-6113 (2019).

181. N. Bloembergen, E. M. Purcell, R. V. Pound, Relaxation Effects in Nuclear Magnetic Resonance Absorption. *Physical Review* **73**, 679-712 (1948).

182. H. Y. Carr, E. M. Purcell, Effects of Diffusion on Free Precession in Nuclear Magnetic Resonance Experiments. *Physical Review* **94**, 630-638 (1954).

183. M. Fuji, H. Iwata, T. Takei, T. Watanabe, M. Chikazawa, The change in wettability and structure of silica powder surfaces modified with hexamethyldisilazane. *Advanced Powder Technology* **10**, 187-198 (1999).

184. T. Takei, A. Yamazaki, T. Watanabe, M. Chikazawa, Water Adsorption Properties on Porous Silica Glass Surface Modified by Trimethylsilyl Groups. *Journal of Colloid and Interface Science* **188**, 409-414 (1997).

185. M. Scheel *et al.*, Morphological clues to wet granular pile stability. *Nature Materials* **7**, 189 (2008).

186. T. G. Mason, A. J. Levine, D. Ertaş, T. C. Halsey, Critical angle of wet sandpiles. *Physical Review E* **60**, R5044-R5047 (1999).

187. M. M. Kohonen, D. Geromichalos, M. Scheel, C. Schier, S. Herminghaus, On capillary bridges in wet granular materials. *Physica A: Statistical Mechanics and its Applications* **339**, 7-15 (2004).

188. D. L. Cantrell, R. M. Hagerty, Microporosity in arab formation carbonates, Saudi Arabia. *GeoArabia* **4**, 129-154 (1999).

189. R. J. S. Brown, I. Fatt, paper presented at the Fall Meeting of the Petroleum Branch of AIME, Los Angeles, California, 1956/1/1/ 1956.

190. A. S. Alsharhan, K. Magara, Nature and distribution of porosity and permeability in jurassic carbonate reservoirs of the Arabian Gulf basin. *Facies* **32**, 237-253 (1995).

191. M. Freire-Gormaly, J. S. Ellis, H. L. MacLean, A. Bazylak, Pore Structure Characterization of Indiana Limestone and Pink Dolomite from Pore Network Reconstructions. *Oil Gas Sci. Technol. – Rev. IFP Energies nouvelles* **71**, 33 (2016).

192. Y. Ji, P. Baud, V. Vajdova, T.-f. Wong, Characterization of pore geometry of Indiana limestone in relation to mechanical compaction. *Oil & Gas Science and Technology–Revue d'IFP Energies nouvelles* **67**, 753-775 (2012).